Mechanistic force model calibration for milling in multiple materials

A Thesis Presented for the

Master of Science

Degree

The University of Tennessee, Knoxville

Dylan Michael Pollard

August 2025

ACKNOWLEDGEMENTS

I would like to thank Dr. Tony Schmitz for the opportunity to further my education and for his guidance through most of my time here at UTK. I would also like to express gratitude to my advisors Dr. Chad Duty, Dr. Bradley Jared, and Dr. Tony Shi for their support in helping me finish this master's thesis.

To everyone here at the machine tool research center, I am forever grateful for their guidance and support during my time here. Especially Jose Nazario, David Roberson, Aaron Cornelius for their help in furthering my knowledge of machining, manufacturing, and the dynamics behind it. As well as all of the other students and interns that have assisted me in machining and research; including Imelia Markus-Brock, Madison Solano, Joshua Hoekstra, Mack Patrick, Hutch Peter, John Greene, and Jun Son.

Finally, I want to thank my mom, Debbie, my dad, Paul, and my two sisters, Sarah and Jordan, for all of their love and support.

ABSTRACT

Being able to measure and simulate cutting forces of milling is crucial to understanding the machining process at a higher level. The research objective of this thesis is to develop and validate a milling mechanistic cutting force model for a variety of materials that can be used to predict machining performance, which includes cutting force and the associated acceleration, velocity, and displacement of the tool and/or workpiece during milling. The cutting forces for development of the simulated model will be measured using a previously studied constrained motion dynamometer (CMD) compared to values from a commercially-available cutting force dynamometer. The CMD measures the displacement of the stage while milling and that displacement is deconvolved into a force using the frequency response function (FRF) of the system. Calculating the cutting force coefficients (CFCs) for a variety of material and tool combinations will be done utilizing a linear regression method with the mean cutting force from a range of feed per tooth values. The CFCs and system parameters are then input into a simulated milling mechanistic force model that can be utilized to predict the milling signals, including force and displacement, for cutting tests completed using the CMD.

Secondary tasks include making improvements to the data collection and calibration processes of the CMD. As well as determining if any changes in the CMDs dynamics, particularly a natural frequency shift, due to a change in workpiece mass can be modeled and compensated as a function of material removed from the workpiece. This will all be done for the purpose of validating and streamlining the process of constructing a simulated milling force mechanistic model utilizing the CMD that can be utilized to simulate cutting conditions beyond the ones used to calibrate the model.

TABLE OF CONTENTS

LIST OF TABLES

LIST OF FIGURES

CHAPTER ONE

INTRODUCTION

Currently, the cost and expertise needed to measure the forces while milling requires a high budget and level of expertise. For that reason, there are not many people outside of academia that are taking advantage of cutting force measurements to help drive their productivity. Even within academia, the tens of thousands of dollars that a commercial system can cost is cost prohibitive for smaller labs that just need force measurements for validations of models and systems. This thesis seeks to present further validation for a previously developed monolithic constrained motion dynamometer (CMD) to obtain force measurements. Current methods utilize costly piezoelectric commercial dynamometers, which do not give perfect results from the dynamometer due to the dynamometer having natural frequencies that amplifies frequency content of measured forces. The cutting force coefficients (CFCs),which specify the amount of force needed to cut an area of material, of the tool-workpiece combination are solved for after filtering the force data. These CFC calculations will be used to characterize a specific tool-workpiece combination to be able to construct a simulated mechanistic force model simulation. The model can be used to simulate any number of speeds, feeds, and depths of cut to obtain the corresponding forces and motion parameters. With a better understanding of the predicted forces and displacements during machining, a programmer can select ideal cutting parameters without having to guess and check through multiple physical cutting tests.

Constrained Motion Dynamometer

The constrained motion dynamometer is a single degree of freedom (SDoF) system that can only displace in one direction, stated as the flexible direction, when a force is imparted upon it. A SDoF system is used because of the simplicity of the structural deconvolution that can be used to obtain a force measurement from a displacement measurement. This filtering is similar to the filtering that has to be completed with the commercial dynamometer, so there is no cost in time gained for having to filter the signal to get a force. Original work with the CMD focused on calibration and validation using limited material and tool sets. There is a need to further validate the system with a variety of tool-workpiece combinations to ensure that more complex tool geometry and harder materials can be measured accurately and modeled for further analysis.

CHAPTER TWO

BACKGROUND AND LITERATURE REVIEW

Milling Description

Cutting Forces

In milling a rotating cutting tool with defined edges feeds along a stationary workpiece to remove material from the workpiece [1], [2]. As the tool translates across the workpiece, a force is imparted from the tool to the workpiece to create a chip. The force acts in the normal and tangential direction of each cutting tooth. These forces can be expressed as shown in Equations 2.1 and 2.2 with two key components; the chip area, which is a function of the axial depth of cut (b) and time dependent chip thickness (h) shown in **Figure 2.1**, and the specific cutting coefficient for the normal and tangential directions (k_n and k_t).

$$F_n = k_n bh + k_{ne} b \tag{2.1}$$

$$F_t = k_t bh + k_{te} b \tag{2.2}$$

The first term in each equation is associated with the force needed for shearing the chip, where the force increases proportionally to the increase in chip area, $b*h$. However, the second term is associated with rubbing of the tool on the workpiece which acts as a frictional force. The rubbing "edge" term is independent of the chip thickness but dependent on the depth of cut and edge specific terms, k_{ne} and k_{te}, for the normal and tangential directions respectively. The force measurements described in this thesis will use a workpiece centered coordinate system, that is the x and y direction forces. **Figure 2.2** shows the previously mentioned forces and their projections in the x and y coordinates for down milling. These are dependent on the cutting angle (φ) of the tooth and the instantaneous chip thickness (h) which is rewritten as $f_t*sin(\varphi)$. A model of the forces in the x and y (feed and cross-feed) directions can then be written using these projections of the normal and tangential cutting forces in equations 2.3 and 2.4.

$$\begin{gathered} F_x = \mathrm{F_n}\sin(\phi) + F_t\cos(\phi) \\ = k_t b f_t \sin(\varphi)\cos(\varphi) + k_{te} b\cos(\varphi) + k_n b f_t \sin^2(\varphi) + k_{ne} b \sin(\varphi) \end{gathered} \tag{2.3}$$

$$\begin{gathered} F_y = F_t si\,n(\phi) - F_n cos(\phi) \\ = k_t b f_t \sin^2(\varphi) + k_{te} b\sin(\varphi) - k_n b f_t\ \sin(\varphi)\cos(\varphi) - k_{ne} b\cos(\varphi) \end{gathered} \tag{2.4}$$

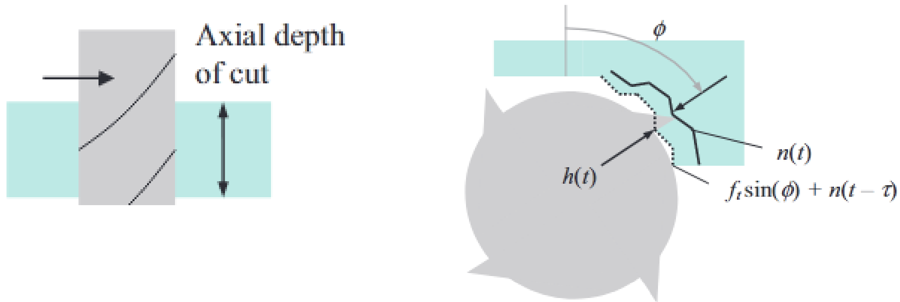

Figure 2.1: Representation of axial depth of cut (b) and chip thickness (h).

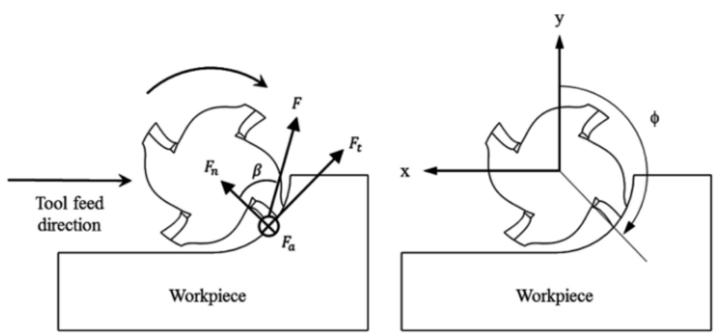

Figure 2.2: Projections of tangential and normal cutting forces with cutting angle for down milling

These will be the driving equations of the mechanistic force model described in this paper. However, the equations are only valid when a tooth is engaged in the workpiece, where φ is between the start and exit cutting angles, φ_s and φ_e. Using the radius of the tool (r) and the axial engagement (a), these values can be calculated. Two directions of milling are possible, up milling and down milling, shown in **Figure 2.3**. For up milling, φ_s equals 0 degrees, and the exit angle is calculated using Equation 2.5.

$$\varphi_e = \cos^{-1}\left(\frac{r-a}{r}\right) \tag{2.5}$$

For down milling, φ_e equals 180 degrees and the start angle is calculated using Equation 2.6.

$$\varphi_s = 180 - \cos^{-1}\left(\frac{r-a}{r}\right) \tag{2.6}$$

Most of the work in this thesis will be utilizing down milling unless otherwise noted, therefore Equation 2.6 will be used for the start angle and a value of 180 degrees will be used for the exit angle.

Cutting Force Coefficients

Cutting force coefficients (CFCs) are material and tool dependent. While similar tools and material group combinations will have similar values, there is no way to know exactly what the values are without experimental testing. Due to slight variations in materials and tools that contribute to the CFC values, as well as the stochastic nature of milling that leads to slight variation in cutting forces. CFC values vary based mainly on the material selection, but also on tooling choice and cutting parameters. To calculate the CFCs, k_n, k_t, k_{ne}, and k_{te}, an average force, a linear regression method is performed [1], [3], [4], [5]. The method takes average force values from a steady state region of milling, over several feed per tooth (f_t) values, to approximate the CFC values for the specific material and tool combination used in the measurements. The mean forces in the feed (x) and cross-feed (y) directions increase in a linear fashion as a function of f_t. This can be seen in **Figure 2.4** where the mean force values for a low carbon steel case is plotted over five feed per tooth values. A linear fit is applied to both force directions to visualize the slope and intercept of the mean forces. An R^2 value of greater than 0.99 is calculated for both directions, which proves the assumption of a linear increase as a function of feed per tooth to be true. Therefore, the equation for the linear regression method takes the form of:

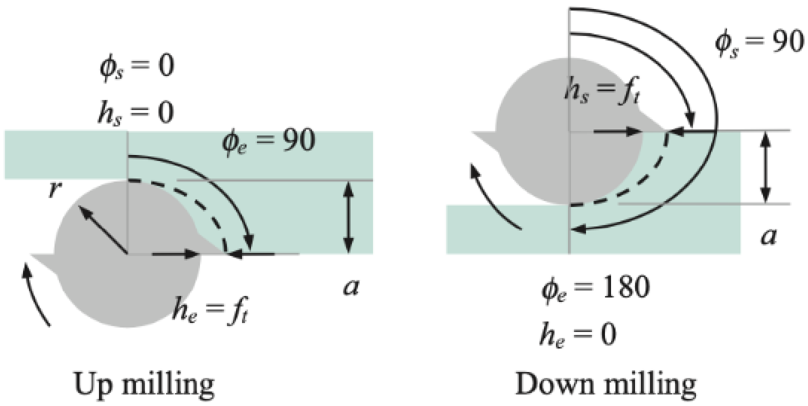

Figure 2.3: Examples for up milling and down milling.

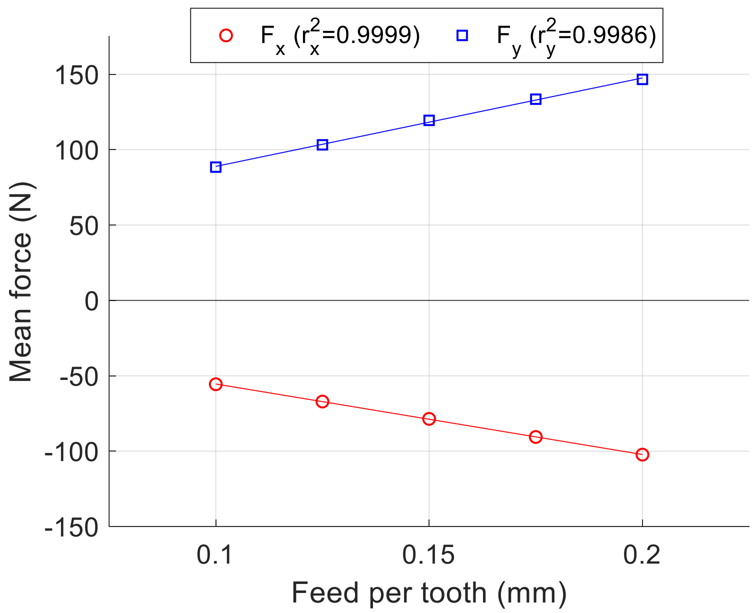

Figure 2.4: Mean force values of milling over five feed per tooth values to be used for the linear regression method.

$$\bar{F}_{j,i} = a_{0j} + a_{1j} f_{t,i} + E_i \tag{2.7}$$

Where the intercept, a_0, and slope, a_1, are calculated using the following summations:

$$a_{1j} = \frac{n \sum_{i=1}^{n} f_{t,i} \bar{F}_{j,i} - \sum_{i=1}^{n} f_{t,i} \sum_{i=1}^{n} \bar{F}_{j,i}}{n \sum_{i=1}^{n} f_{t,i}^2 - \left(n \sum_{i=1}^{n} f_{t,i}\right)^2} \tag{2.8}$$

$$a_{0j} = \frac{1}{n} \sum_{i=1}^{n} \bar{F}_{j,i} - a_{1j} \frac{1}{n} \sum_{i=1}^{n} f_{t,i} \tag{2.9}$$

In these equations *j* indicates the direction (*x*, *y*, and *z*), and *n* represents the total number of test cuts performed for the linear regression, typically *n* equals five. While performing this method, all cutting parameters are kept the same and only the feed per tooth is changed. The slope and intercept are calculated for the *x* and *y* directions utilizing the f_t values and corresponding mean forces for each direction. There will be separate slopes and intercept values for both coordinate directions. The following Equations 2.10 and 2.11 are utilized with these values to solve for the cutting and edge coefficients in the tangential and normal directions.

$$\bar{F}_x = \left\{ \frac{N_t b f_t}{8\pi} \left[-k_t \cos(2\varphi) + k_n (2\varphi - \sin(2\varphi)) \right] + \frac{N_t b}{2\pi} \left[k_{te} \sin(\varphi) - k_{ne} \cos(\varphi) \right] \right\}_{\varphi_s}^{\varphi_e} \tag{2.10}$$

$$\bar{F}_y = \left\{ \frac{N_t b f_t}{8\pi} \left[k_t (2\varphi - \sin(2\varphi)) + k_n \cos(2\varphi) \right] - \frac{N_t b}{2\pi} \left[k_{te} \cos(\varphi) + k_{ne} \sin(\varphi) \right] \right\}_{\varphi_s}^{\varphi_e} \tag{2.11}$$

These equations, derived in part from Equations 2.3 and 2.4 [1], solve for the average force value over the cutting region between φ_s and φ_e. Where N_t is added to account for the number of teeth on the cutting tool. Utilizing the above equations with the slope and intercept values, the cutting force coefficient values can then be calculated utilizing linear algebra methods. The integration limits only affect the sine and cosine values, so those can be solved for independent of the other terms. First the intercept values can be used to solve for the non-feed-dependent edge coefficients, and then the slope values are used for the feed-dependent cutting coefficients in the two following equations.

$$\begin{bmatrix} a_{0x} \\ a_{0y} \end{bmatrix} = \frac{N_t b}{2\pi} \begin{bmatrix} \sin(\varphi) & -\cos(\varphi) \\ -\cos(\varphi) & -\sin(\varphi) \end{bmatrix}_{\varphi_s}^{\varphi_e} \begin{bmatrix} k_{te} \\ k_{ne} \end{bmatrix} \tag{2.12}$$

$$\begin{bmatrix} a_{1x} \\ a_{1y} \end{bmatrix} = \frac{N_t b}{8\pi} \begin{bmatrix} -\cos(2\varphi) & (2\varphi - \sin(2\varphi)) \\ (2\varphi - \sin(2\varphi)) & \cos(2\varphi) \end{bmatrix}_{\varphi_s}^{\varphi_e} \begin{bmatrix} k_t \\ k_n \end{bmatrix} \tag{2.13}$$

The start and exit angles are calculated utilizing the rules depicted in Equations 2.5 or 2.6 depending on if up or down milling is being performed. Since the only unknown values are the CFC values, simple linear algebra inverse matrix methods can be used to solve for the values. The tangential and normal CFCs can also be expressed as a specific CFC (K_s) and angle (β), and their relations are shown in equations 2.14 and 2.15.

$$K_s = \sqrt{{k_t}^2 + {k_n}^2} \tag{2.14}$$

$$\beta = \tan^{-1}\left(\frac{k_t}{k_n}\right) \tag{2.15}$$

The K_s and β is used for simplicity of reporting the CFCs as just a magnitude and angle. This helps for simplicity in comparison of values, opposed to the tangential and normal components.

Frequency Response Functions

Frequency response functions (FRFs) are needed to determine the dynamics of a system. An FRF is a representation of how a system responds to an external stimulus over a range of frequencies. The receptance FRF gives a transfer function of the output displacement over the input force in the frequency domain. An FRF is measured utilizing a modal hammer and piezoelectric accelerometer shown in **Figure 2.5**. The accelerometer is attached to the system using modal beeswax or super glue. Using the modal hammer, an impulse is imparted on the system and resulting acceleration is measured. The force and acceleration signals are transformed from the time domain into the frequency domain utilizing a fast Fourier transform, which is converted into a displacement over force FRF. Equation 2.16 shows how acceleration is converted to displacement in the frequency domain.

$$\frac{X}{F} = -\frac{1}{\omega^2} \cdot \frac{A}{F} \tag{2.16}$$

Repeating this process multiple times and averaging the result provides a good representation of the receptance of the system being measured. The FRF can then be used to calculate the natural frequency (ω_n), stiffness (k), and damping ratio (ζ) values of the system, also known as the modal parameters. These values are used to construct approximations of the system's FRF and as inputs for time domain simulations. **Figure 2.6** shows an example of a two degree of freedom system FRF with a real and imaginary part.

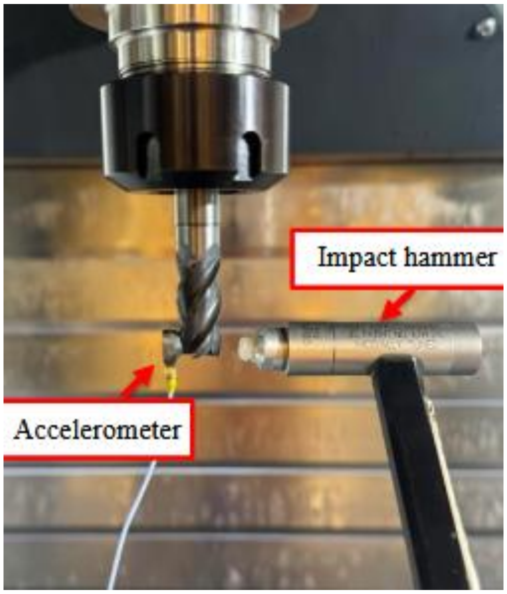

Figure 2.5: Image of tap testing to find a tool tip frequency response function

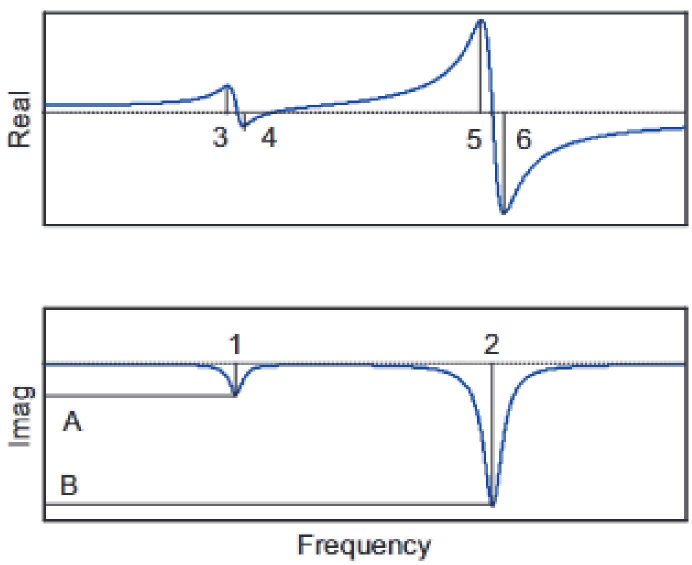

Figure 2.6: Example of a two degree of freedom FRF used for peak picking explanation [1].

To solve for the modal parameters mentioned, a peak picking method is used. The peak amplitudes are used in the real and imaginary parts of the FRF alongside their corresponding frequencies. The natural frequency (ω_n) is first found by looking at the frequency of the negative peak in the imaginary part as shown in Equation 2.17.

$$\omega_{n1} = \omega_1 \tag{2.17}$$

Where the frequency is in radians/second and ω_1 is the frequency at point 1. Next the damping ratio (ζ) is found by taking the difference in the positive and negative peaks in the real part as shown in Equation 2.18.

$$\zeta_1 = \frac{\omega_4 - \omega_3}{2\omega_{n1}} \tag{2.18}$$

With the damping ratio being unitless decimal equivalent of a percentage. Finally, the stiffness value is calculated using the previous calculated values with the amplitude (A) of the negative peak of the imaginary part of the FRF as shown in Equation 2.19.

$$k_1 = \frac{-1}{2\zeta_1 A} \tag{2.19}$$

Peak picking can be repeated for as many modes needed for an FRF given that the modes are relatively spaced apart to be able to decern where and what the peak values are for the system. As will be shown later, the CMD is a single degree of freedom system, so usually there will only be one mode to calculate these values for.

Stability Mapping

Stability maps are used to select milling process parameters that ensure stable cutting. In unstable cutting, chatter is classified as a self-excited vibration caused by surface regeneration effects as each tooth passes the previously cut surface [1], [6]. **Figure 2.7** shows the instantaneous chip thickness, $h(t)$, depends on both the vibration of the previously machined surface and the vibration of the current tooth. In stable milling, these vibrations are in phase, which results in a nearly constant chip thickness between cuts. In unstable milling however, these vibrations are out of phase, which results in a widely varying chip thickness throughout the cut. Large changes in cutting forces occur due to this change in chip thickness and lead to a state of self-excited vibrations which ensures further instability in subsequent cuts.

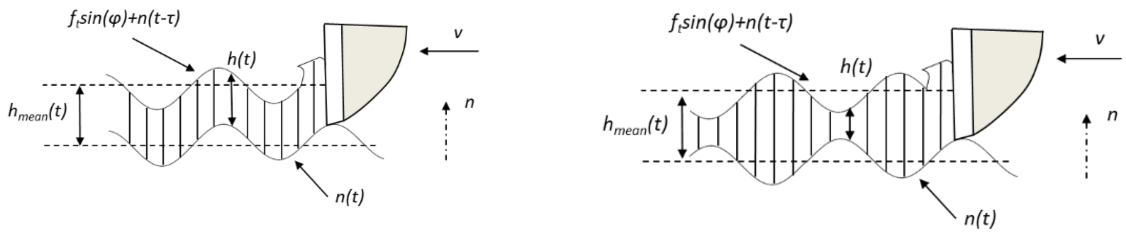

Figure 2.7: Vibration effects on instantaneous chip thickness in milling for stable (left) and unstable (right) cutting.

These vibrations are able to occur due to flexibility in both the tool and workpiece. In order to avoid cutting parameters that would induce these self-excited vibrations, stability lobe diagrams (SLDs) are constructed. SLDs are able to qualify areas of stable and unstable cutting conditions as a function of varying spindle speed and axial cutting depth. The primary method used is an analytical Fourier Series approach presented by Altintas and Budak [7]. In this approach, the tool diameter, number of teeth, radial depth of cut, specification of up or down milling, cutting force coefficients, and tool/workpiece frequency response functions (FRFs) are required to solve for the stability boundaries. The first 4 inputs can be specified for the process by the user and usually remain constant for differing materials or setups, but the CFCs and FRFs need to be determined for each tool-workpiece combination and vary as the workpiece and setup changes. As previously stated, a linear regression method is used to determine the CFC values for a certain tool-workpiece combination. While it is possible to reasonably predict these values for different workpiece materials based on previous experiments, there is no guarantee that these values will be correct for the specific system. Especially if the tool is of an abnormal geometry or if the workpiece material properties vary from one sample to another. Therein lies a need for an inexpensive and reliable way to gather these CFC values, which is a focus of this research. For the FRFs, modal tap testing is utilized to find these values for both the tool and workpiece in the machining x and y coordinates. Once these values are acquired, the SLD can be constructed, and a spindle speed and axial depth can be selected that ensures stable cutting conditions. **Figure 2.8** shows an example of a SLD constructed using a single degree of freedom (SDOF) system, the region below the blue line represents stable cutting conditions and above is unstable conditions.

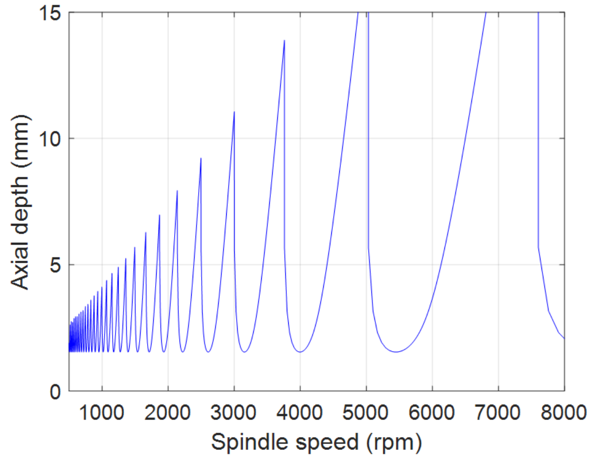

Figure 2.8: Stability lobe diagram utilizing the Fourier serries approach for a single degree of freedom system

Mechanistic Force Model

The basis of this thesis is to construct and calibrate a simulated mechanistic force model for use in predicting milling forces for a variety of tools and materials. The force model that is used is based on the "regenerative force, dynamic deflection model" described by Smith and Tlusty [8], and is expanded upon by Schmitz and Smith [1]. Milling can be described by a periodic forcing function which contains frequency content at the tooth passing frequency and its harmonics. The model utilizes second order numerical integration to output the motion parameters used to solve for changing instantaneous chip thickness as the tool and workpiece vibrate independent of each other. Once the model is run, the simulation outputs the force between the tool and workpiece over time, as well as the displacement, velocity, and acceleration for both the tool and workpiece over time, all in the x (feed) and y (cross-feed) directions.

Simulation

To set up the mechanistic force model there are a number of parameters needed to ensure an accurate simulation. First, all user defined inputs are selected for the model. Including the axial (b) and radial (rd) depth of cut, specification of up vs. down milling, spindle speed (Ω), and feed per tooth (f_t). Next is the tool parameters such as the number of teeth (N_t), diameter of tool (d), tooth spacing, helix angle (γ), and the tooth-to-tooth runout of the end mill. All of these parameters can be directly selected or measured using traditional means for use in the system. The two parameters that cannot be selected this way are the modal parameters and cutting force coefficients.

Modal parameters can be measured directly using modal impact testing as described above, indirectly through dynamic finite element analysis simulations [9], [10] or through receptance coupling [11]. These values are used in the simulation for the numerical integration of the equations of motion. The acceleration, velocity, and displacement are solved for each mode in the tool and workpiece x and y directions at each step. Since the tool and workpiece have different structural dynamics, they will respond to the force input differently. Therefore, their motion parameters are solved for separately.

CFCs are one of the important parameters of the system, affecting the magnitude of the forces and resulting displacements of the system, as well as the overall stability limit. As described above, these values can be obtained through a series of physical test cuts using an average force linear regression method, or alternatively an instantaneous force, nonlinear optimization method [3]. With the parameters set, the simulation proceeds in the following manner [1]:

1. The instantaneous chip thickness, *h(t)*, is calculated utilizing the current feed and previous step's displacement between the tool and workpiece
2. If a section of tooth is engaged in the material, the force in the tangential, F_t, and radial, F_n, directions are calculated utilizing the CFCs, *h(t)*, and *b* values.
3. The forces are converted to *x* and *y* directions and summed up for each section of tooth engaged in cutting.
4. The differential equations of motion (acceleration, velocity, and displacement) of the tool and workpiece in the *x* and *y*-directions are then solved using the current force and corresponding modal mass, *m*, damping, *c*, and stiffness, *k*. The general equations of motion are as follows:

$$F_x = m_x\ddot{x} + c_x\dot{x} + k_x x \tag{2.20}$$

$$F_y = m_y\ddot{y} + c_y\dot{y} + k_y y \tag{2.21}$$

5. Once the motion parameters are solved, the total values are stored, and the current cutter angle is incremented.
6. The process is repeated for a specified number of steps

When setting up for the simulation, the discretization of the tool and cutting angles is used to properly apply numerical integration techniques. The cutting tool is discretized axially to account for the helix angle, γ. A time step, *dt*, is determined to ensure that all frequencies in the system are present in the simulation. A resulting step per revolution, SR, and step per tooth, ST, is calculated and rounded to ensure that there are an integer number of steps. The angle in degrees between each step, $d\varphi$, can then be solved using the following equations:

$$SR = \frac{60}{dt \cdot \Omega} \tag{2.22}$$

$$d\varphi = \frac{360}{SR} \tag{2.23}$$

The instantaneous chip thickness in step 1 is calculated using the tooth angle, φ, dependent chip thickness, the vibration normal to the surface for the current tooth, *n(t)*, and the previous tooth,

$n(t\text{-}\tau)$, at the same angular position, and the runout of the current tooth. The equation takes the form of:

$$h(t) = f_t \sin(\phi) + n(t-\tau) - n(t) + RO \tag{2.24}$$

Force Measurements

Commercial Cutting Force Measurement Systems

Being able to measure cutting forces during a machining process is crucial to understanding the physics of how the material is being cut. Commercial cutting force measurement systems can vary in cost and complexity. The most common dynamometers utilize piezoelectric crystals that produce a voltage when stress is applied to the crystal. A sensitivity coefficient is used to convert this measured voltage back into a force measurement. The dynamometer used in this research is the Kistler 9257B, a three-component dynamometer that utilizes four piezoelectric crystals that are sensitive to stresses in the x, y, and z directions. Piezoelectric dynamometers are robust and calibrated to a high precision but are costly in the range of tens of thousands of dollars just for the dynamometer, amplifier and cables. **Figure 2.9** shows the dynamometer and arrangement of the piezoelectric crystal force sensing element.

Constrained Motion Dynamometer

The measurement system used in this research is a constrained motion dynamometer (CMD). The design is the same used and validated in previous works by Gomez and Mason [4], [12]. The design consists of a moving platform attached to the base through four leaf-type flexure elements that are arranged in a parallel configuration, see **Figure 2.10** for image and **Table 2.1** for the dimensions of the geometry. The leaves behave as parallel rectilinear springs with linear behavior over a small displacement range that is half the flexure thickness, t. The way in which they are constrained to the platform and frame constricts movement to a single direction perpendicular to the leaves. The constraints make it so the CMD a single degree of freedom system, in which it ideally is only allowed to displace in a single direction. When the moving platform is displaced, there is an elastic deformation or strain in the leaves, that introduces stress in the material. Maximum allowable displacements of the leaves are calculated to ensure that this stress does not exceed the yield strength of the material, therefore plastically deforming the leaves and changing the system response.

Figure 2.9: Kistler 9257B (left) and the diagram of the piezoelectric crystals arrangement (right) [13].

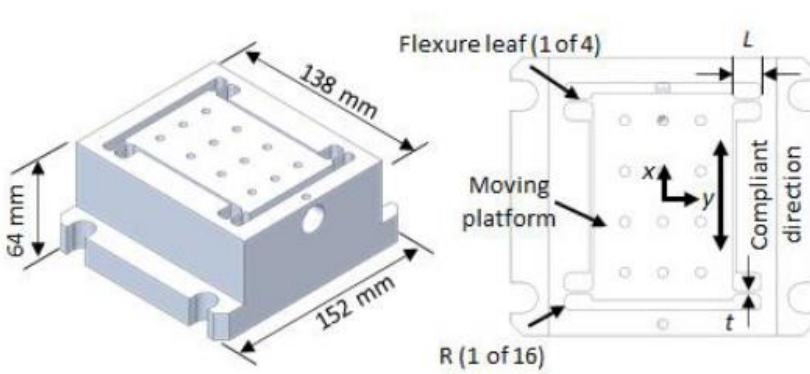

Figure 2.10: Constrained motion dynamometer design.

Table 2.1: Geometry of the flexure leaves

Length, L (mm)	Width, b (mm)	Thickness, t (mm)	Radius, R (mm)
10	44.5	1.27	3.2

The material chosen to construct the dynamometer was 6061-T6 aluminum alloy. The nominal elastic modulus, E, and yield strength, σ_y, of the material are 69 GPa and 276 MPa respectively. To maintain the elastic behavior of the leaves, a maximum allowable stress is set to 60% of the yield strength, or 160 MPa. The maximum allowable displacement, $x_{allowable}$ of the stage is then calculated using the following equation:

$$x_{allowable} = \frac{\sigma_{allowable} L^2}{3Et} \cong \pm\, 50\ \mu m \tag{2.25}$$

To solve for the equivalent spring constant of the system the following equations are used:

$$I = \frac{bt^3}{12} \tag{2.26}$$

$$K_{eq} = \frac{n12EI}{L^3} = \frac{4Et^3}{L^3} \tag{2.27}$$

Term n represents the number of flexure elements, which is four. The maximum force range can then be found using Hooke's law with the allowable displacement and equivalent spring stiffness of the system. The spring constant force can be determined as, $K_{eq} = 1.5 * 10^7$ N/m, and the maximum allowable force is ± 1500 N.

CHAPTER THREE

MODIFICATIONS AND METHODS

Optical Interrupter Calibration

The optical interrupter knife edge sensor (KES) is responsible for measuring displacement of the dynamometer stage in the flexible direction. To conform with the low-cost requirements of the system, a RHOM RPI-0352E optical interrupter was chosen which ranges in price from 50-85 cents per sensor. Photo-sensors such as this have been used in the past for a force measuring unit which works in a similar manner to derive a force measurement from the change in voltage of the interrupter [14]. Previous work has been conducted to calibrate and prove the effectiveness of the KES for use in measuring displacements of the constrained motion dynamometer [12], [15], [16]. The working principal involves a knife edge (X-ACTO™ #17) that displaces to partially block the light beam between the infrared light emitting diode (ILED) and phototransistor. As the blade moves laterally through the sensor, the intensity of light is increased or decreased as the blade moves out or into the beam, respectively. This change in intensity due to displacement results in a change in output voltage in the phototransistor that can then be measured using an analog to digital converter (ADC). **Figure 3.1** shows the KES and knife interaction, where the knife blade is rigidly attached to the stage. A calibration is preformed to be able to get a displacement over voltage ratio. The ratio is applied to the voltage to be able to read a related displacement of the stage from a measured change in voltage.

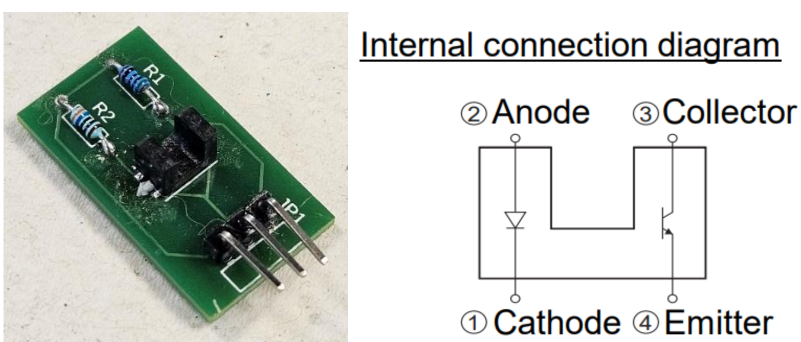

Figure 3.1: Image of ROHM RPI-0352E sensor (left) and corresponding circuit diagram (right)

Reworking of Circuit

All previous works that utilized the optical interrupter KES used a 15-volt variable power supply to provide power to the ILED and phototransistor within the optical interrupter [4], [12], [16]. After consulting the manufacturer of the sensor and accompanying data sheet [17], the input was reduced to a 5-volt constant power supply to reduce the chance of overloading the ILED which has a 5-volt reverse voltage (the maximum voltage an LED can withstand without damage in reverse polarity). The ability to use a fixed 5-volt power supply is beneficial to ensuring proper calibration of the sensor. Since the output voltage of the phototransistor is related to the input voltage, any variation in the input voltage leads to variation in the output response which increases or decreases the calibration coefficient. Along with the change in input voltage, the load resistors, R2 and R1, had to be decreased as well to 330 ohms for the ILED and 500 ohms for the phototransistor, see Figure 3.1 for circuit diagram. A 3D printed fixture was designed to assist in repeatable placement of the KES within the bottom of the CMD as shown in **Figure 3.2**. This allows the sensor to be taken out of the dynamometer for calibration and placed back in with the sensor square to the compliant direction of the dynamometer without any complex alignment.

Calibration of Sensor

The calibration coefficient needed is a µm/V value, and is used to convert the voltage out from the KES to a corresponding displacement of the knife and, by extension, the movement platform of the CMD. For initial calibration of the knife edge sensor, a linear air-bearing positioning stage (Aerotech ABL 10100-LT) was used. The KES was placed on a stationary position while the knife was fixtured to the air-bearing stage and moved, at a prescribed displacement per time, into the range of the sensor as shown in **Figure 3.3**. In the current configuration, the optical interrupter has an output voltage range of 0-0.34 V, and a resolution less than 1 µm. **Figure 3.4** shows the change in voltage over time as the knife is moved into the beam of the sensor and, highlights the linear range over which the sensor will be operated. The sensitivity coefficient was determined to be 790 µm/V, with a linear range of approximately 120 µm that is centered around 0.17 V.

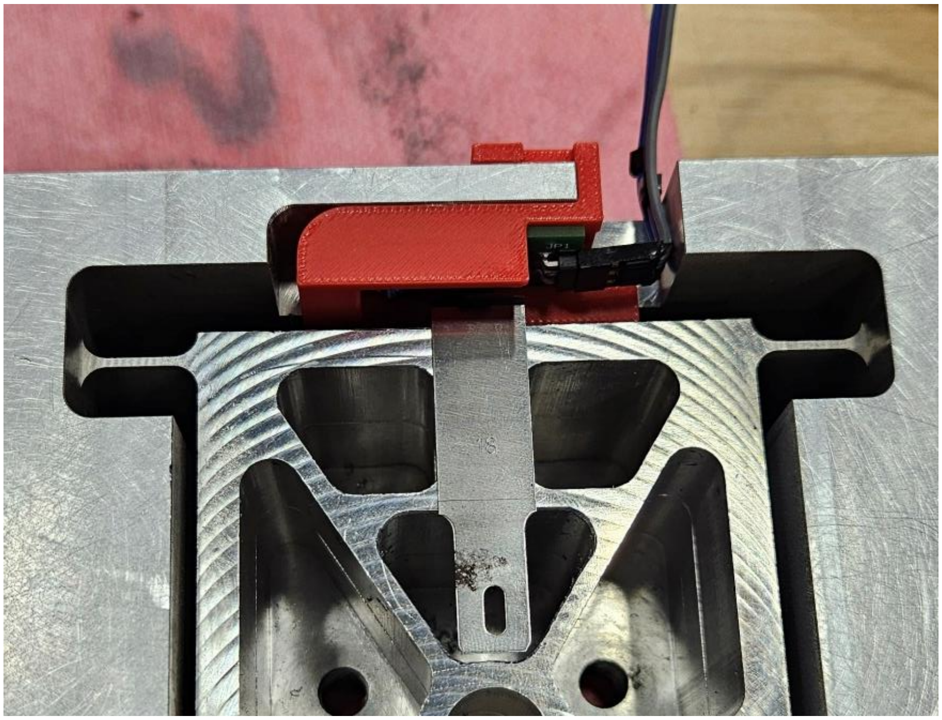

Figure 3.2: 3D printed KES holder placed in the base of the CMD

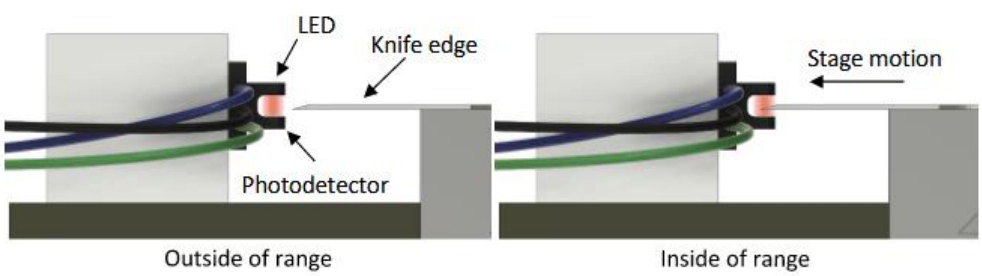

Figure 3.3: Optical interrupter and knife edge interaction.

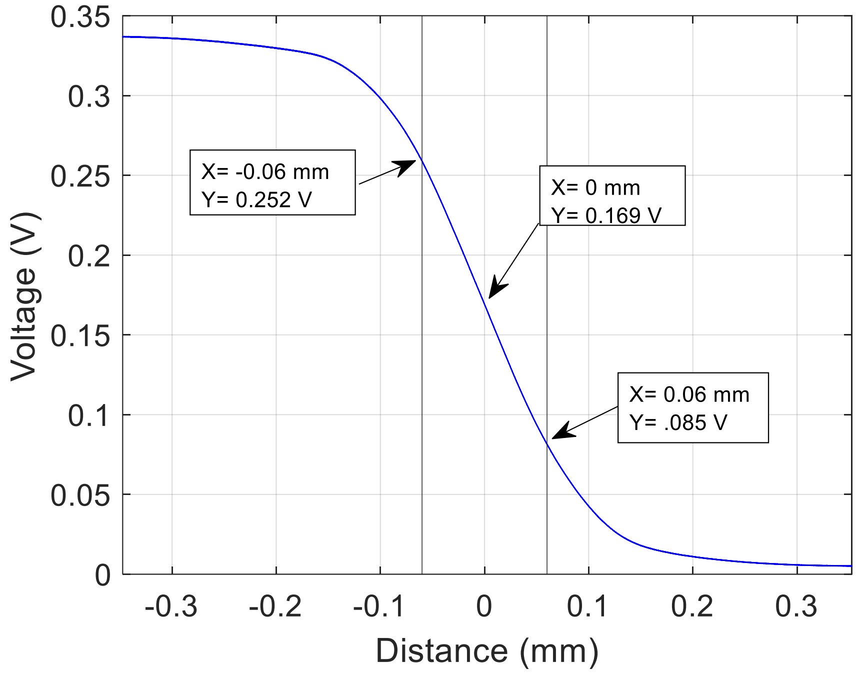

Figure 3.4: Plot used for initial calibration of KES. Displacement is zeroed at the middle of the voltage and linear range of the sensor.

Due to slight variations in the KES setup between the linear air bearing stage and CMD, an on-system calibration was performed to update the initial sensitivity coefficient. This was performed through a hanging mass test with the KES mounted in the CMD. The CMD was mounted so that the compliant direction is parallel to the direction of gravitational acceleration (rotated 90 degrees about its *y*-axis), see **Figure 3.5**. A string was attached to a bolt that was fixed on top of the CMD flexible stage, and a set of weights was attached to the bottom of the string. This method was used to minimize any moment effects about the *y*-axis that would result from a center of mass that is not located at the interface of the flexible stage. The ganging mass test utilizes a known mass to displace the flexible stage a prescribed amount, and by measuring the change in voltage for the prescribed change a calibration can be calculated. The mass (m) of the weights used were measured as 4.559 kg. Utilizing Newton's second law, the static force that the weights imparted on the stage due to gravity (g) was found to be 44.64 N. Tap testing was performed on the CMD to find the estimated static stiffness for the single degree of freedom system. The resulting modal parameters were as follows, f_n = 930 Hz, k = $2.0*10^7$ N/m, and ζ= 1.50 %. In a SDOF system the modal stiffness calculated at the natural frequency of the system is equal to the static stiffness. Hooke's law can be used to predict the static displacement due to the force of the weights as 2.236 μm. Equation 3.1 shows how the static force from gravity can be related to the spring force acting on the flexure system.

$$F = mg = k\Delta x \tag{3.1}$$

After utilizing this equation to obtain the expected displacement (Δx), the calibration coefficient can then be found. The voltage of the KES was measured as the mass was added and taken off of the system as shown in **Figure 3.6**. Due to the significant signal noise, the average value was taken in each section for the weighted and un-weighted system to get the mean voltage. The change in voltage (ΔV) was calculated multiple times to get a mean value for the change as well. This difference in voltage was found to be 2.746 mV, which can be used with Equation 3.2 to obtain the calibration value.

$$calibration = \frac{\Delta x}{\Delta V} \tag{3.2}$$

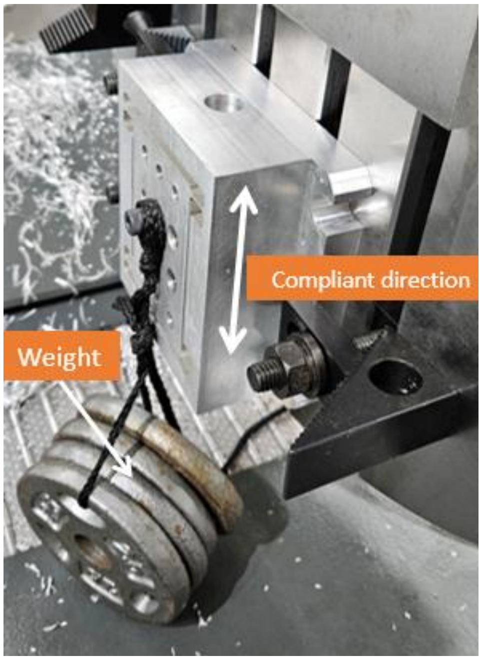

Figure 3.5: CMD mounted aligned to gravity with weights attached.

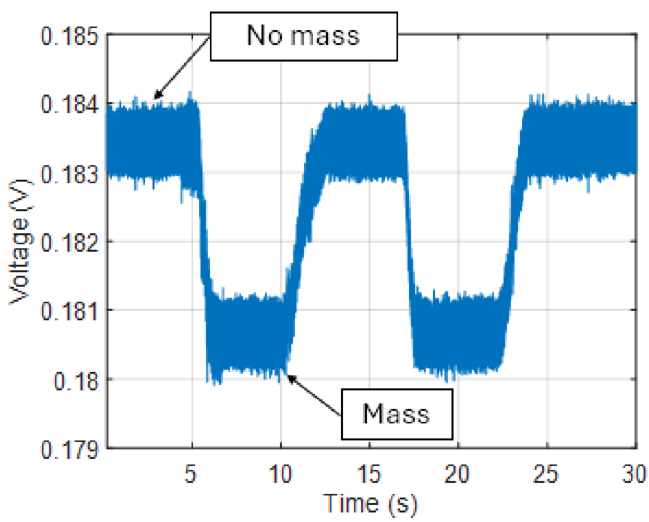

Figure 3.6: Voltage reading as the mass is added and taken off of system.

Solving for the calibration coefficient, a value of 814 μm/V was observed for the current setup of the system. This updated value is close to, but not exactly what was found using the air stage, potentially due to slight differences in set-up conditions. Since it better represents the actual conditions of the sensor, 814 μm/V is used for the sensitivity in all measurements. This method is also more cost effective since any weights can be attached to the system, as long as the actual mass of it can be obtained for the calculations.

Structural Effects Compensation

Even with an updated sensitivity coefficient, in initial measurements there was a discrepancy in the displacement measurements of the KES at the bottom of the stage to measurements taken on the workpiece itself where the forces are applied. **Figure 3.7** shows a comparison from the KES measuring at the bottom of the stage compared to a measurement from a laser doppler vibrometer measuring at the top of a one inch tall workpiece. To quantify this error in measurements, the following steps had to be taken. First a static finite element analysis (FEA) study was conducted to see if there was a difference in the flexible direction displacement from the top of the workpiece to the KES at the bottom of the moving stage. Then tap testing was conducted at different vertical points on the CMD-workpiece combination to be able to determine the difference in the physical system, as well as to create a compensation factor for this phenomenon.

Finite Element Analysis

Finite element analysis is helpful in predicting how a physical system might behave in different circumstances. With a monolithic structure design, there exists the need to be able to discretize the structure into smaller elements that can be solved for in a simulation, which is taken care of in FEA. SolidWorks was used as the FEA software for simulations. The goal of this simulation is to see how the displacement magnitude changes vertically through the CMD-workpiece combination as a force is applied on the workpiece.

To represent the physical system, the workpiece was modeled as a 3x2x1 inch block with the counterbore holes for the M8 bolts used to fix the workpiece to the CMD. Shown in **Figure 3.8** is the model for the CMD-workpiece combination that will be used for FEA simulations. The workpiece is constrained to the moving platform using a bolted constraint to best reflect the

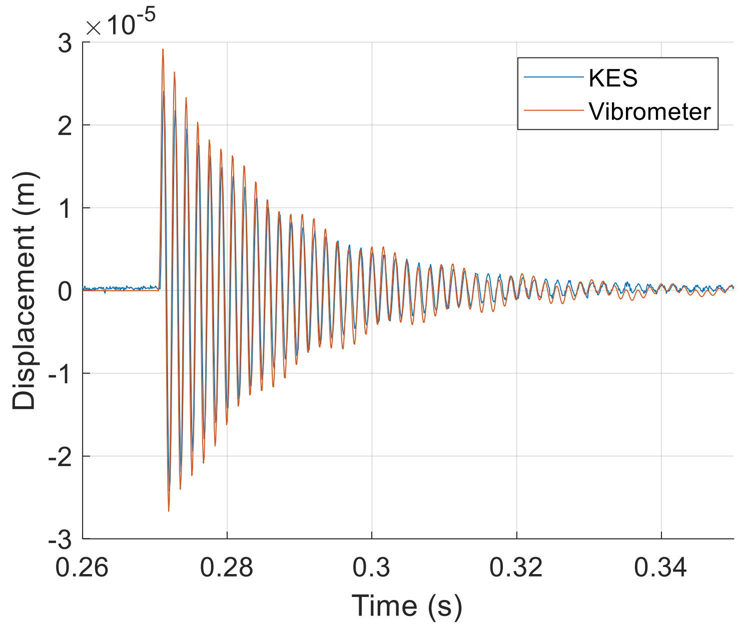

Figure 3.7: Comparison of displacement of workpiece measured by laser Doppler vibrometer and the displacement of the moving platform measured by the KES.

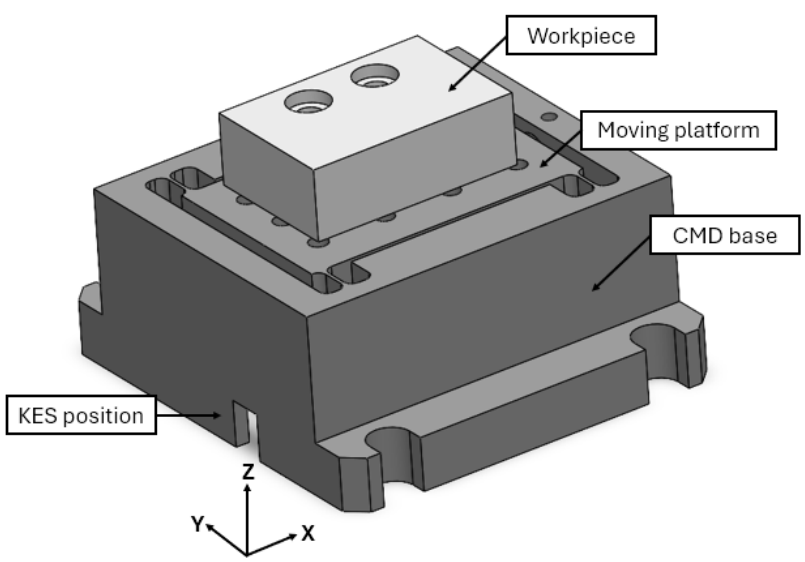

Figure 3.8: CMD model used for FEA.

actual loading of the system. The CMD and workpiece are both made of 6061-T6 aluminum, **Table 3.1** gives the material properties used in the simulation. The CMD itself is fixed on its bottom face similar to what it would be on the machine table, and the mesh with the constraints is shown in **Figure 3.9**. With the materials and boundary conditions set, the position of the applied force and measured displacement are decided. **Figure 3.10** shows that the input force is applied at the top corner of the workpiece (mimicking the start of a cut) and the displacement is measured at nodes along the center line at positions from the top of the workpiece to the bottom of the moving stage.

For the initial set of simulations, the input force location and displacement measurement locations were kept constant while the magnitude of the force increased from 1 Newton to 1000 N. This was to verify if there was a linearity in response for differing force values. For the 1 N input there was a resulting flexible-direction displacement of 0.040 μm at the top of the workpiece, 0.0375 μm at the top of the moving platform, and 0.0343 μm at the bottom of the moving platform where the knife edge is located. For this setup, there is a 15 % error between the value of the displacement at the top of the workpiece (node 15) is and the displacement at the bottom of the stage (node 9558). **Table 3.2** shows the rest of the measurements, which has a linear relationship of input force to output displacement for 1-1000 N.

In the next simulation set, the position of the force and top displacement measurements were incrementally changed from the top of the workpiece (25.4 mm) to the bottom of the workpiece (3 mm) in six steps. The bottom, moving platform, measurement was taken at the where the KES would be positioned for each simulation. **Table 3.3** shows the displacements in the flexible direction of the CMD, in mm, at the same height as the force input and at the bottom where the KES is attached. When the force was applied at the top of the block (24.5 mm), the bottom (KES) displacement error was 12.7 %, and when the force was moved down the block (3 mm), the bottom displacement error was 5.66 % compared to the actual displacement at the force location. The effect can be attributed to a bending mode in the system that acts about the about the *y*-axis of the moving platform and workpiece. Along the vertical z-axis of the dynamometer, the bending mode leads to a difference in the magnitude of displacement in the flexible direction.

.

Table 3.1: Material properties for 6061-T6 aluminum

Property	**Value**	**Units**
Elastic Modulus	6.90×10^{10}	N/m^2
Poisson's Ratio	0.33	-
Shear Modulus	2.60×10^{10}	N/m^2
Mass Density	2.7×10^3	kg/m^3
Tensile Strength	1.24×10^8	N/m^2
Yield Strength	5.51×10^7	N/m^2

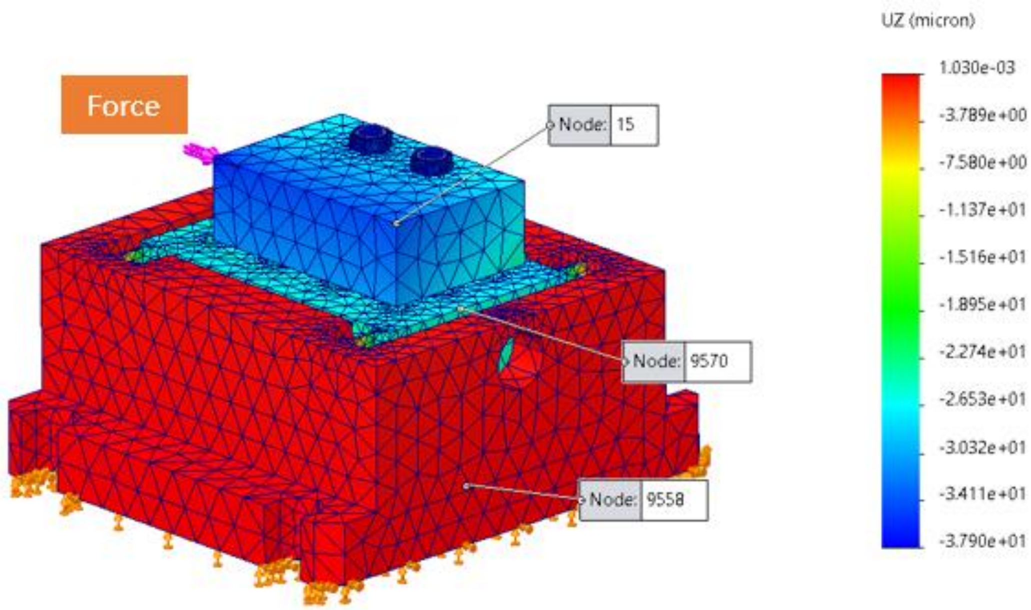

Figure 3.9: Mesh used for the FEA simulation.

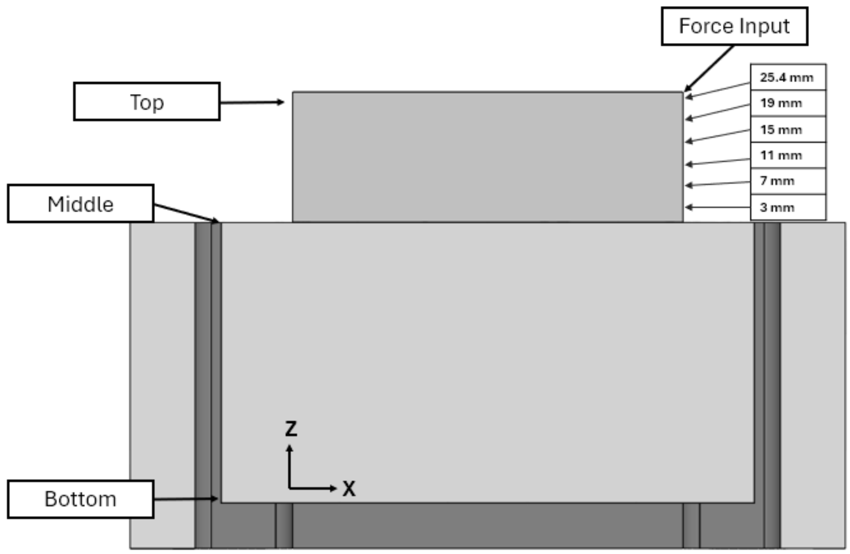

Figure 3.10: FEA force input and measurement locations for displacements

Table 3.2: Displacement values in microns for FEA simulation at the top of the workpiece, middle boundary between workpiece and moving stage, and bottom of moving stage.

Position	Node #	1 N	10 N	50 N	100 N	250 N	500 N	750 N	1000 N
Top	15	0.040	0.403	2.02	4.03	10.10	20.20	30.30	40.30
Middle	9570	0.038	0.375	1.88	3.75	9.38	18.80	28.10	37.50
Bottom	9558	0.034	0.343	1.72	3.43	8.58	17.20	25.70	34.30

Table 3.3: Comparison of displacements at different 100 N force input locations to displacement at the bottom of the CMD moving stage

Force position (mm)	25.4	19	15	11	7	3
Displacement (µm)	3.92	3.85	3.81	3.76	3.71	3.69
Bottom disp. (µm)	3.42	3.43	3.45	3.46	3.47	3.48
% Error	12.74%	10.94%	9.58%	8.03%	6.49%	5.66%

It can then be concluded that as the force input moves further away from the KES in the *z*-axis, a larger discrepancy will be seen between the actual displacement of the workpiece and the displacement that is measured from the KES. Since it is impossible to input the force at the same vertical position of the KES, there will always be a discrepancy, and therefore a way to compensate for this difference is needed.

Impulse Testing for Compensation Coefficient

Similar testing was conducted on the physical system to characterize the bending mode resultant error on actual measurements from the CMD [18]. A series of tests was conducted using three workpieces; aluminum 6061-T6, AISI 4140 steel, and titanium 6-Al-4V. A series of five FRFs, one direct and four cross, were taken using a method similar to the first FEA test. The hammer hit remained at the top cutting depth, and the accelerometer was moved along the vertical center line of the workpiece and moving platform at five different locations to determine a correlation. **Figure 3.11** shows the top placement of the accelerometer on the physical system. The 5th location utilized the displacement directly from the KES for the FRF instead of the accelerometer because to properly compensate for the measured and actual displacement the measured FRF from the KES is needed. Three tests were performed for each material, with a different hammer strike location for each set of FRFs. The placements are shown in **Figure 3.12** for the hammer and accelerometer positions, where L1-L5 are the accelerometer placements and C1-C3 is where the hammer strike is performed. The modal parameters were found for all FRFs at the CMDs SDOF natural frequency. Since the modal stiffness, *k*, relates to the displacement of the system, that was the parameter used in evaluation. **Figure 3.13-15** shows the modal stiffness values versus the vertical distance from the KES for the three trials for each material, and their corresponding lines of best fit. Notice the piecewise nature of the fit that lies at L4 or the boundary between the moving platform and workpiece (52.5 mm). Each material and strike location results in a different stiffness value at the natural frequency of the system, therefore all stiffness values were normalized to position L5, at the KES, as shown in **Figure 3.16**. Since the KES will never move position the normalization was done from the bottom to be able to account for different heigh workpieces that could be used in future testing. This also helps to visualize the displacement at the KES vs. actual displacement for differing heights of cut as a percentage.

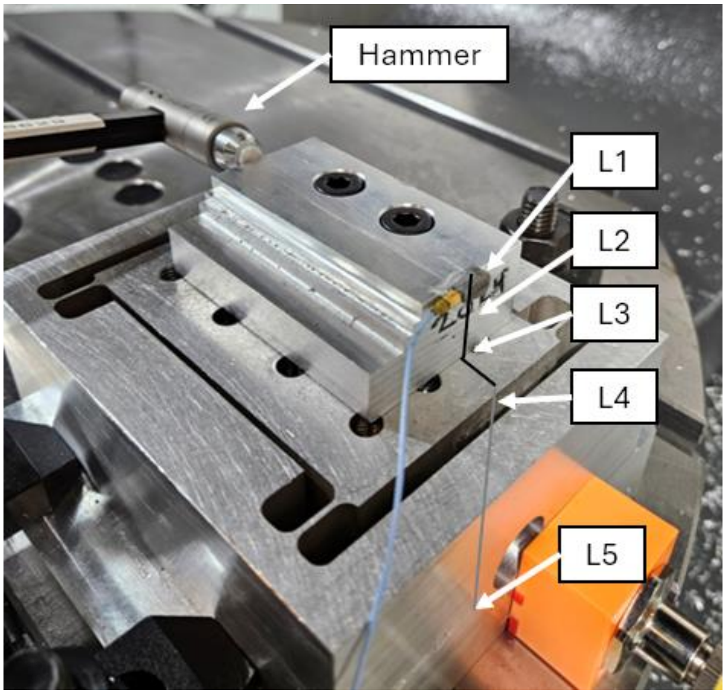

Figure 3.11: Positions of accelerometer placements on the physical CMD.

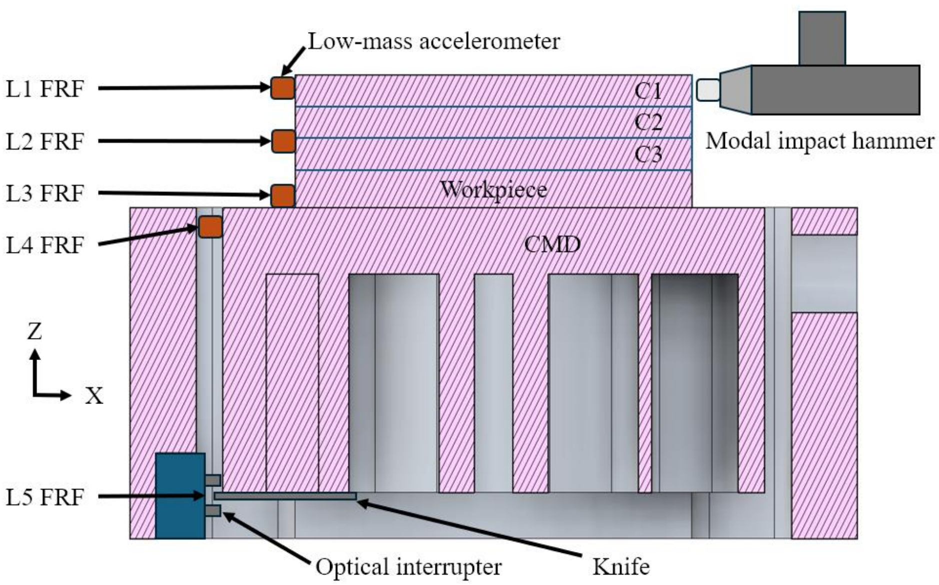

Figure 3.12: Section view for accelerometer and hammer strike locations used in the tap testing [18].

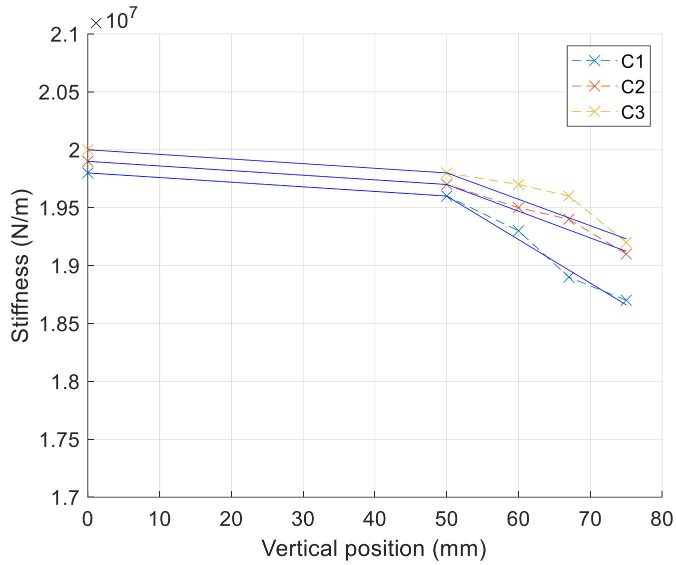

Figure 3.13: Modal stiffness values and best fit lines at the CMD natural frequency for aluminum 6061-T6 [18].

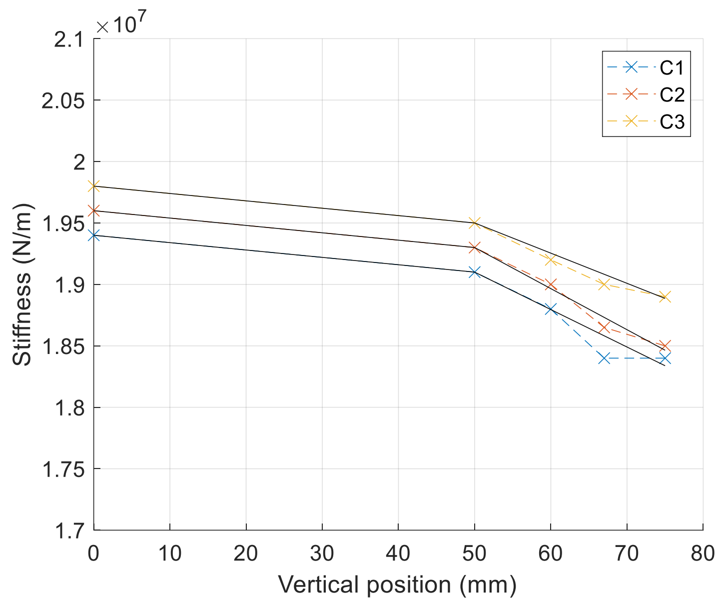

Figure 3.14: Modal stiffness values and best fit lines at the CMD natural frequency for AISI 4140 steel [18].

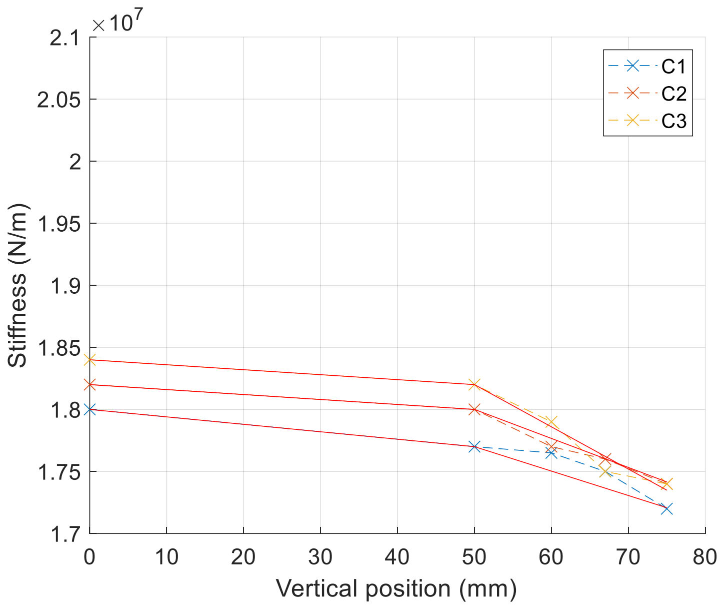

Figure 3.15: Modal stiffness values and best fit lines at the CMD natural frequency for titanium 6Al-4V [18].

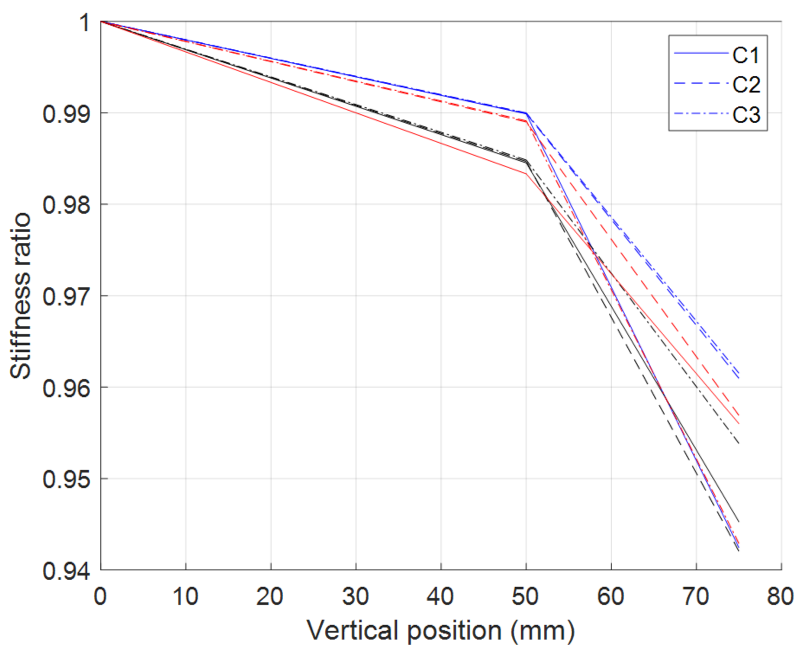

Figure 3.16: Normalized modal stiffness values for all three trials and materials; (black) AISI 4140 steel, (blue) 6061-T6 aluminum, and (red) titanium 6Al-4V [18].

A total piecewise fit can then be applied using the average values of each individual fit, which will result in a compensation coefficient, α, based on the vertical height from the KES. Equation 3.3 is used to obtain the alpha value from a best fit of the average of the lines shown in **Figure 3.16**.

$$\alpha = 0.987 - 0.0018(x - 52.5) \tag{3.3}$$

Where the values 0.987 and 52.5 correlate to a 98.7% displacement at 52.5mm above the KES, at the boundary between workpiece and moving platform. Above that boundary is a decrease of 0.18% of displacement per millimeter up the test workpiece. To obtain the actual displacement (x_{actual}) at the force input, the perceived measured displacement ($x_{measured}$) from the KES is divided by this α value as shown in equation 3.4.

$$x_{actual}(t) = \frac{x_{measured}(t)}{\alpha} \tag{3.4}$$

The compensation allows for an accurate displacement signal to analyze before any force analysis is done, which can lead to better modeling of the motion and force parameters. Compared to previous methods that only use the cross FRF at the KES which only accounts for the force compensation and not the displacement measurement compensation [15]. Which is useful when only the resultant forces are needed, but when trying to model displacement this method is not able to produce an accurate displacement for analysis. Therefore, all displacement signals in this research will utilize the newly developed method for displacement compensation prior to any analysis.

Structural Deconvolution

Structural deconvolution can be used to obtain force from a measured voltage or displacement of a dynamic system [15], [19]. The CMD acts as a mechanical filter that converts an applied force into a displacement which is amplified at the natural frequency of the system. The system's FRF expresses the amplitude of displacement for a certain force input over a range of frequencies. To obtain the original force input, the inverse of the FRF must be applied to the displacement signal, which is converted to the frequency domain via fast Fourier transform (FFT), to be able to obtain the force signal in the frequency domain as shown in Equation 3.5.

$$F(\omega) = \left(\frac{X}{F}\right)^{-1} \cdot \; X(\omega) \; \cdot \text{Butterworth} \tag{3.5}$$

However, the amplitude of the system's FRF approaches zero as frequency approaches infinity, and as a result when inverted, the amplitude of the inverse FRF will approach infinity as frequency approaches infinity. Any high frequency noise in the measurement would be amplified. Therefore, a 3rd order lowpass Butterworth filter is applied to the inverted FRF to attenuate the high frequency content. The cutoff frequency is usually at or slightly above the system's natural frequency to ensure that no relevant frequency content below the natural frequency is lost. **Figure 3.17** shows an example of the amplitude of the original FRF, the inverted FRF with no filter, and the inverted FRF with the Butterworth filter applied. The modal parameters used in the example are similar to those of an aluminum workpiece on the CMD and can be seen with the cutoff frequency in **Table 3.4**. Once applied, the signal is converted back into the time domain via inverse FFT.

Inverse Force Filtering

Similar to the CMD, the Kistler 9257B dynamometer also acts to amplify any force content near its natural frequencies. The resultant measured force signal does not accurately represent the original force input to the system. To compensate for this effect, a filtering approach similar to the previously discussed structural deconvolution filtering is conducted using force as an input and output of the measured FRF. The modal impact hammer is used as the input force, same as any other FRF, but for the response, the dynamometer's force output is utilized. This results in a force-to-force FRF as opposed to the typical force-to-displacement (receptance) FRF. **Figure 3.18** shows an example of the resultant FRF with a 3x2x1 in aluminum 6061 workpiece mounted for the *x* and *y*-direction of the Kistler 9257B dynamometer. Similar to the structural deconvolution, the force-to-force FRF is inverted and a lowpass Butterworth filter is applied above the natural frequency of the system, with f_{cutoff} at 2500 Hz. The dynamometer force signal is converted into the frequency domain through an FFT. **Figure 3.19** shows the inverted force-to-force filter that is applied to the dynamometer force in the frequency domain. The resulting signal will not be affected near the lower frequencies, but the forces at frequencies near the natural frequency of the system will be attenuated to obtain a closer approximation to the actual force input into the system. The resulting filtered force signal can then be used in comparison to the CMD deconvolved forces.

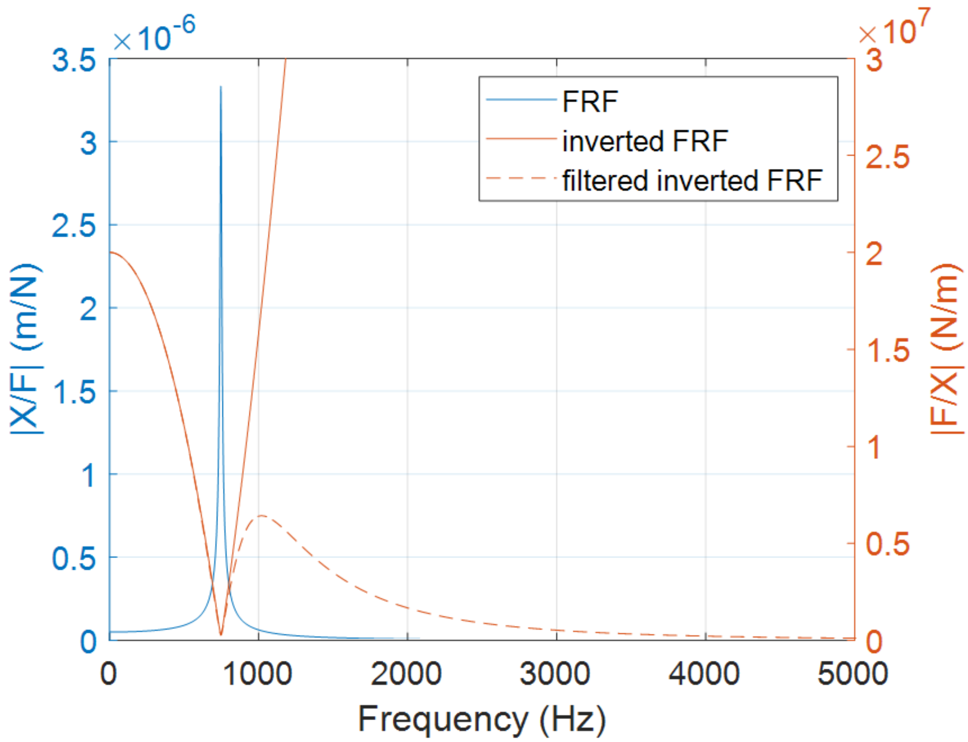

Figure 3.17: Structural deconvolution filter example for SDOF FRF.

Table 3.4: Parameters of structural deconvolution example shown in figure 3.9.

f_n (Hz)	k (N/m)	ζ (%)	cutoff (Hz)
750	2.00E+07	0.75	850

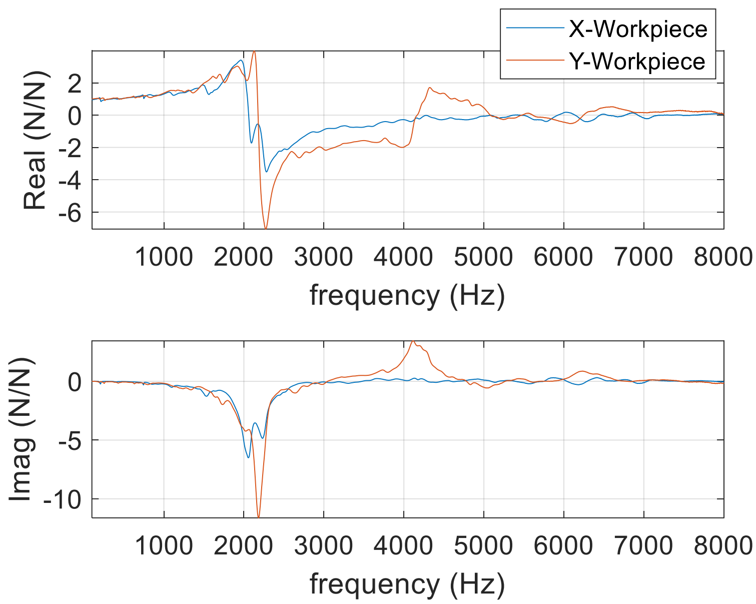

Figure 3.18: Force-to-force FRF for the Kistler 9257B with an aluminum 6061 workpiece

Figure 3.19: Amplitude of inverted force-to-force FRF for *x* and *y*-directions

Tooth Passing Frequency Consideration

The selected spindle speed of cutting directly effects the frequency content in the force and displacement measurements taken during milling. The tooth passing frequency (f_{tooth}) and its harmonics (N), is a function of the spindle speed (ω) and number of teeth (N_t) on the tool as shown in Equation 3.6.

$$f_{tooth,N} = \frac{\omega * N_t}{60}\ \mathrm{N} \tag{3.6}$$

Where N=1 is the first fundamental tooth passing frequency (TPF), and N increases as an integer for the second, third, etc. harmonics of the fundamental TPF. The higher the spindle speed or larger number of teeth, the higher the first tooth passing frequency will be. This is important to consider when using the CMD to measure signals during milling because the bandwidth (the maximum frequency that can be captured without a loss in signal magnitude) is low compared to a commercial dynamometer. The CMDs bandwidth is only around 600-800 Hz for different density workpieces. The reason for the range is the mass dependence on the natural frequency of the system. For a denser material there will be more mass for the same volume and results in a lower f_n. Therefore, when selecting a spindle speed for a test it is important to know the number of teeth of the tool and the SDOF natural frequency of the system for the particular material. For example, aluminum will be on the higher end of f_n, approximately 750 Hz, and tools for aluminum will have fewer teeth, usually two or three. On the other end, more dense steel workpieces will have lower natural frequencies around 630 Hz and the cutting tools for steel will usually have four or more teeth.

The first of two major consideration when selecting spindle speed is to ensure that at least the first three harmonics (including the fundamental harmonic) are below the natural frequency of the system. Previous work for a turning based dynamometer mentions that the tooth passing frequency should be four times less than the natural frequency of the system [20], but due to the higher spindle frequencies present in milling a value of three times should suffice to able to keep the tool rotation at reasonable cutting speeds. Three TPFs would ensure that enough harmonics are below the bandwidth of the sensor to accurately deconvolve the force signal. For a two-fluted tool spinning at 5000 rpm the tooth passing frequency content is shown alongside the FRF of the

CMD in **Figure 3.20**. For this case there are four tooth passing frequencies below the natural frequency, which follows the first consideration. The second consideration is that the tooth passing harmonics, should not be equal to or within 5% of the natural frequency of the system. While setting a harmonic equal to the natural frequency of a system usually leads to the highest stability boundary, it also typically results in the region of highest surface location error (SLE) which is the error in geometry cause by forced vibrations [1], [21]. When cutting in these regions, the harmonic that is equal to f_n would be amplified by the maximum amount due to the previously mentioned mechanical filtering effect. The structural deconvolution would be able to attenuate this effect, but the real issue is that the displacement signal would be too high for the physical system. With cuts in these regions being predicted at far higher displacements than the recommended maximum CMD displacement of 50 μm. **Figure 3.21** shows the amplification effect when using all of the same cutting conditions for the two fluted tool but now spinning at 5600 rpm, where the fourth TPF is now equal to the natural frequency of the system at 747 Hz. The TPF is amplified to ten times the maximum of the previous figure. While this 5600 rpm example is still a stable cutting condition, the amplification leads to a displacement of up to 40 μm, where the 5000 rpm case was only reaching maximum displacements of 10 μm. Therefore, to be able to properly deconvolve the force for a stable cut, the TPF will need to be considered after obtaining an initial value from the stability maps.

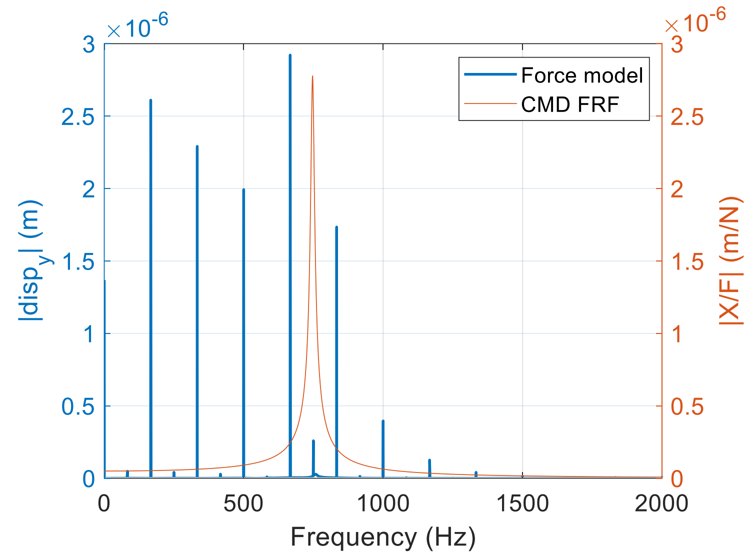

Figure 3.20: Tooth passing frequency for a two-fluted tool spinning at 5000 rpm.

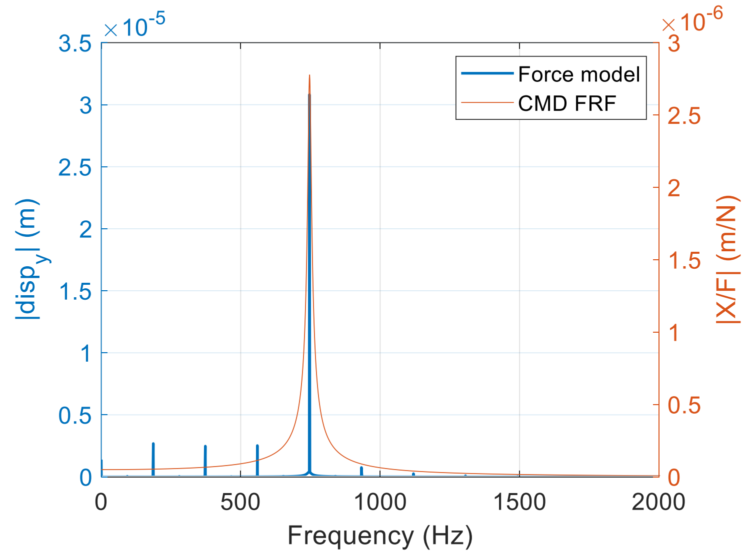

Figure 3.21: Tooth passing frequency for a two-fluted tool spinning at 5600 rpm.

CHAPTER FOUR

EXPERIMENTAL METHODS

The work of this research is to be able to model and predict cutting forces for a range of different tools and materials. The main component that needs to be captured is the cutting force coefficients (CFCs). The following testing procedure will explain how a low-cost constrained motion dynamometer (CMD) can be used in place of a commercial-grade piezoelectric dynamometer to be able to measure forces needed for the model construction.

Experimental Setup

A wide range of materials and appropriate cutting tools were selected for this work. Materials will be separated into their ISO classifications; non-ferrous (N), steel (P), hardened steel (H), stainless steel (M), and superalloy (S). Tooling is selected based on common tools used for certain material groups**. Table 4.1** shows the list of materials and **Table 4.2** shows the tooling and the material types for which they are rated. Each material will have two different tools to be able to test the ability to construct models for different tool types and geometries. For the non-ferrous materials, a Kennametal uncoated two flute carbide endmill was chosen to compare against an Accupro three fluted zirconium nitride (ZrN) coated tool to see how the number of flutes and coating of the tool affects the CFC values, if at all. For the ferrous materials and titanium, both of the tools have a similar AlTiN coating, but the Kennametal tool has a unique tooth spacing that is meant to break up the harmonics of the tool to reduce chatter. Instead of a 90-90-90-90 degree spacing between the four teeth in the Accupro tool, the Kennametal tool has roughly a 90-95-90-85 degree spacing. This tool was chosen to see if the abnormal tooth spacing affected the mean force values while milling. All aluminum tests have been conducted on a HAAS UMC-1000 5-axis milling center, but due to an increase of electrical noise, subsequent testing was conducted on a HAAS VF-4 SS vertical milling center.

Testing Workflow

A consistent testing workflow was performed for all tools and materials. There are process checks to ensure that the cutting conditions remain stable and that filtering is taking place properly. The procedure for data collection and mechanistic force model evaluation is as follows:

Table 4.1: Materials used throughout testing and their ISO material types.

Material name	**ISO group**
2024 aluminum	N
6061 aluminum	N
7075 aluminum	N
110 copper	N
1018 steel	P
4140 steel	P
A36 steel	P
H13 steel	H
303 stainless steel	M
304 stainless steel	M
316 stainless steel	M
440 stainless steel	M
6Al-4V titanium	S

Table 4.2: Tools used throughout testing and their specifications.

Manufacturer	**Coating**	**Diameter (in)**	**Teeth**	**Helix (deg)**	**Material types**
Kennametal	uncoated	0.5	2	45	N
Accupro	ZrN	0.5	3	37	N
Accupro	AlTiN	0.5	4	40	P,M,S,H
Kennametal	AlTiN	0.5	4	38	P,M,S,H

1. The tool and workpiece of interest are selected. The workpiece was prepared into a 3x2x1 inch sample to perform the test cuts on. The tool specifications were measured and stored. This includes diameter, helix angle, tooth-to-tooth runout, and tooth spacing.
2. The radial depth of cut and specification of up or down milling are determined. An initial guess of the cutting force coefficients is taken. These are approximate for different material types based on initial measurements with generic tools.
3. Frequency response functions (FRFs) are taken for the tool, workpiece on the CMD, and workpiece on the Kistler. For the tool and CMD, the FRF is a force-to-displacement measurement in the machine *x* and *y* coordinates (see **Figure 4.1**). For the Kistler, the FRF is a force-to-force measurement in both the *x* and *y* coordinates (see **Figure 4.2**).
4. Stability maps are constructed using the CMD FRF, approximate CFCs, and selected cutting parameters. Due to the asymmetric nature of the system, stability maps are constructed for *x* and *y* milling directions of the CMD.
    a. An initial guess of stable cutting conditions is gathered from both of the stability maps, and the corresponding axial depth of cut and spindle speed are noted.
5. An initial mechanistic force model is constructed to simulate cutting on the CMD in the *x* and *y* directions based on all of the parameters set and the initial CFC guess. This is used to check for time domain stability, and also to ensure that predicted maximum force and displacement signals are within the dynamometers previously defined limits.
    a. If the cut is stable and within limits in both cutting directions, then continue to test
    b. If the cut is not stable or within limits in either cutting direction, then select new cutting parameters based on stability maps.
6. Perform the tests cuts at varying feeds needed for the average force, linear regression method. Ten total cuts, five in the *y* and then five in the *x*-direction, are taken on the CMD. The initial cuts in each direction are checked for stable cutting. Five total cuts are performed on the Kistler dynamometer to obtain both *x* and *y*-direction forces.
    a. An initial FRF is used to deconvolve the y-direction force, and a second FRF is measured after the *y*-direction cuts are performed to be used for deconvolution of the *x*-direction force.

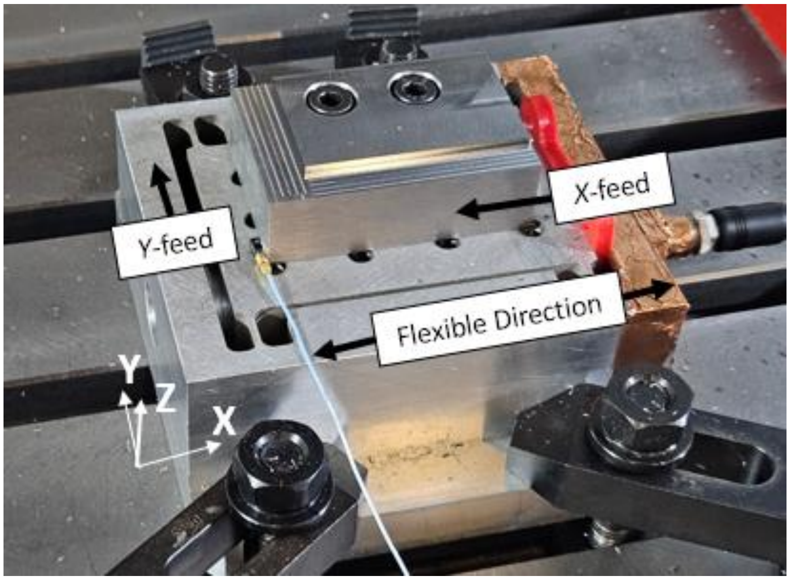

Figure 4.1: CMD setup on table with corresponding coordinate system.

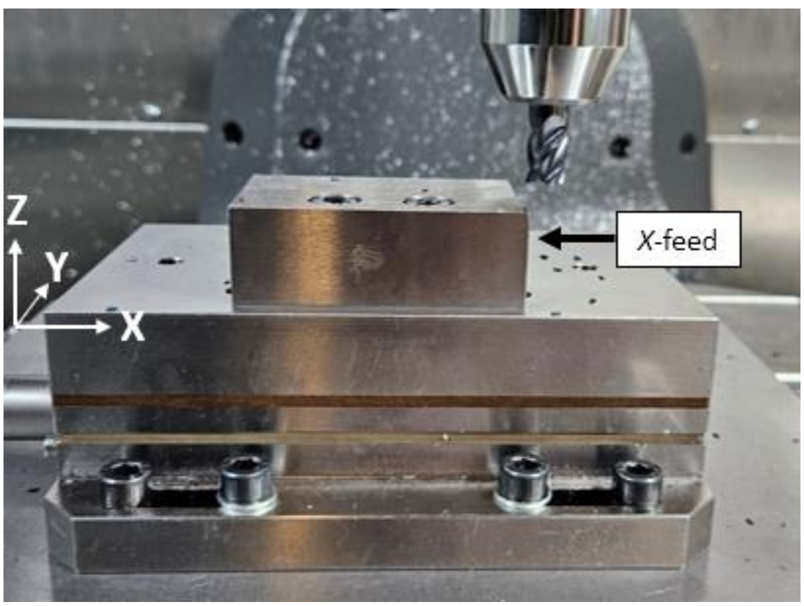

Figure 4.2: Kistler 9257B setup on table with corresponding coordinate system.

7. The inverse force filtering technique is performed on the cuts from the CMD and Kistler. The CMD uses receptance FRF measurement while the Kistler is using the force-to-force FRF for the inverse filter.
    a. The mean and max forces from the CMD and Kistler cuts are compared for the feed and cross feed directions to ensure that the value obtained from the CMD can be trusted to be correct
    b. CFC values are then obtained from the CMD measurements to update the model
8. The initial force model is then updated with the measured CFC values
    a. The forces are then compared to the CMD forces to validate the ability of the model to approximate cutting forces seen while milling

This workflow is shown in **Figure 4.3** as a process diagram to be able to visualize where parameters are set to and where any checks are done throughout collection. FRFs were taken as described above on the appropriate workpiece while the CMD is clamped to the table with the compliant direction parallel to the *x*-axis of the machine. The FRF of each tool was taken only when initially set up, since the tool's dynamics do not change from test to test. The stability maps mentioned in step 4 were constructed using the analytical Fourier Series approach previously mentioned. Due to the limitations of the current CMD to be able to measure in only a single direction, two cuts were performed for each feed value to be able to measure the displacement in the feed direction (*x*), where the tool is traveling parallel to the compliant direction, and in the cross-feed direction (*y*), where the tool is traveling perpendicular to the compliant direction. The stability maps can only predict stability for one direction of cutting, so separate stability maps were constructed to be able to predict the stability boundary where the flexible direction is in line with the feed direction (*x*) and a second where it is in line with the cross-feed direction (*y*).

An initial force model was constructed as described in Chapter 2 using the specific parameters of each test. The Fourier series approach used for stability mapping is a time invariant method which does well at approximating the stability of a system but is not able to consider the tool parameters or time variant regenerative effects. For this reason, the time-domain force model is used to verify that the cut parameters found using stability maps are going to be stable. At this

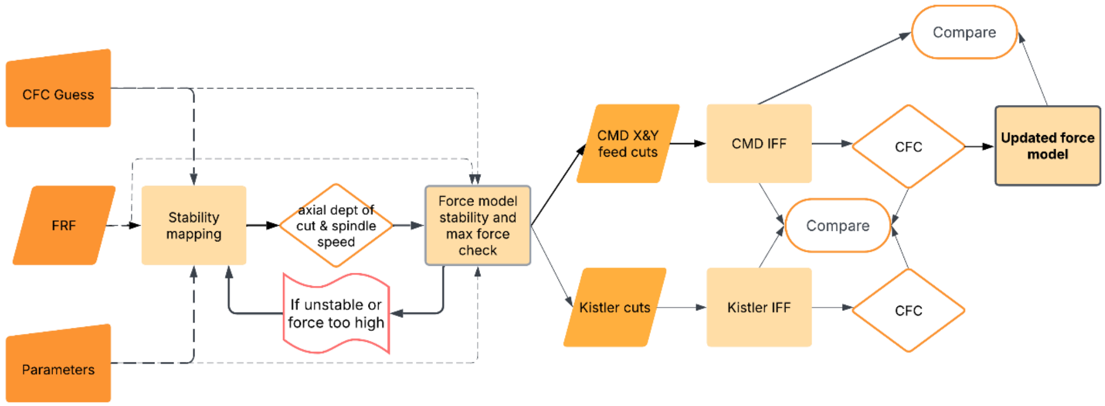

Figure 4.3: Process flow diagram of testing procedure to construct the force model.

point there will still be some uncertainty since the CFCs are not the exact values for the tool-workpiece combination. The force model is also used to verify that the maximum force and workpiece displacement is within the allowable 1500 N or ±50 μm so as to not destroy the flexure by exceeding the yield strength.

Displacement data was taken for the cuts on the CMD utilizing the KES as described in Chapter 3. The sensor is set up such that the displacement data is taken only in the linear range of the KES output. The sensitivity coefficient ($\Delta x/\Delta V$) was applied to the measured voltage (V) from the KES to convert to a displacement measurement ($x_{measured}$). After that the compensation value (α) is applied to the measured displacement to get the real displacement (x_{actual}) at the workpiece from the measured displacement at the KES. This process is shown in Equation 4.1, where all of the signals are still in the time domain.

$$x_{measured}(t) = \frac{\Delta x}{\Delta V} V(t) \;\Rightarrow\; x_{actual}(t) = \frac{x_{measured}(t)}{\alpha} \tag{4.1}$$

As stated before, the sensitivity used for all tests will be 0.814 mm/V, and the typical measured range of alpha values will be between 0.85-0.95 for all tests. The DC offset and transience of the signal have to be removed to be able to properly apply the inverted CMD FRF to the signal. A fast Fourier transform is then performed on the steady state region of the displacement data to convert the time-domain displacement into the frequency domain.

Aluminum 6061-T6 trial

Initial Setup

For this experiment, the CMD and commercial dynamometer (Kistler 9257B) were set up on a Haas UMC-1000 vertical 5-axis milling center. As shown in **Figure 4.4**, both dynamometers were set up parallel to the *x*-direction of the machine by utilizing a dial indicator attached to the spindle to minimize cosine error. Cosine error results from taking a measurement of a signal at an angle relative to the direction of the signal, which results in the measured value being smaller than the actual value. The CMD was mounted to the machine table using toe clamps which were torqued to 65 N-m, and the commercial dynamometer was mounted to a ground steel plate, which was mounted to the table, and was also torqued to 65 N-m to ensure the system was rigidly mounted to the table. The sample workpieces were trammed and mounted to both dynamometers utilizing two M8 x 1.25 bolts torqued to 35 N-m. The workpieces were taken from the same bar stock to ensure consistency. All tools were mounted in a Schunk hydraulic holder to minimize runout. Runout was measured with a dial indicator when the tool in in the machine, the relative distances of each tool from the center of the tool are stored. The tool used in this example was the Kennametal, two fluted, uncoated, square endmill (mfg. # 3658904). The tool is kept the same for the *y* and *x*-direction cuts on the CMD and commercial dynamometer. Once the workpiece and tool were set up the initial cutting parameters were determined. Down (climb) milling will be used for all tests. The radial depth of cut in all tests will be 2 mm or 15.75% of the tool diameter to ensure that ensure enough percentage of the tool is engaged without producing cutting forces too high for the CMD. For the same reasoning a feed per tooth range was selected to be 0.1 – 0.2 mm/tooth with a 0.025 mm/tooth step to give a total of five feed per tooth values. Tool parameters are taken from **Table 4.2** for the two fluted Kennametal tool. Finally, the previously acquired cutting force coefficients was set for 6000 series aluminum to have a K_s value of 750 N/mm^2 and β angle of 60 degrees.

The frequency response measurements were taken for the tool in the machine for the *x* and *y* orientations of the tool relative to the machine's axis and can be seen plotted in **Figure 4.5**. **Figure 4.6** shows the receptance FRF for the CMD that was also taken in the machine *x* and *y* directions. To ensure that the modal parameters are accurate, the impulse location and

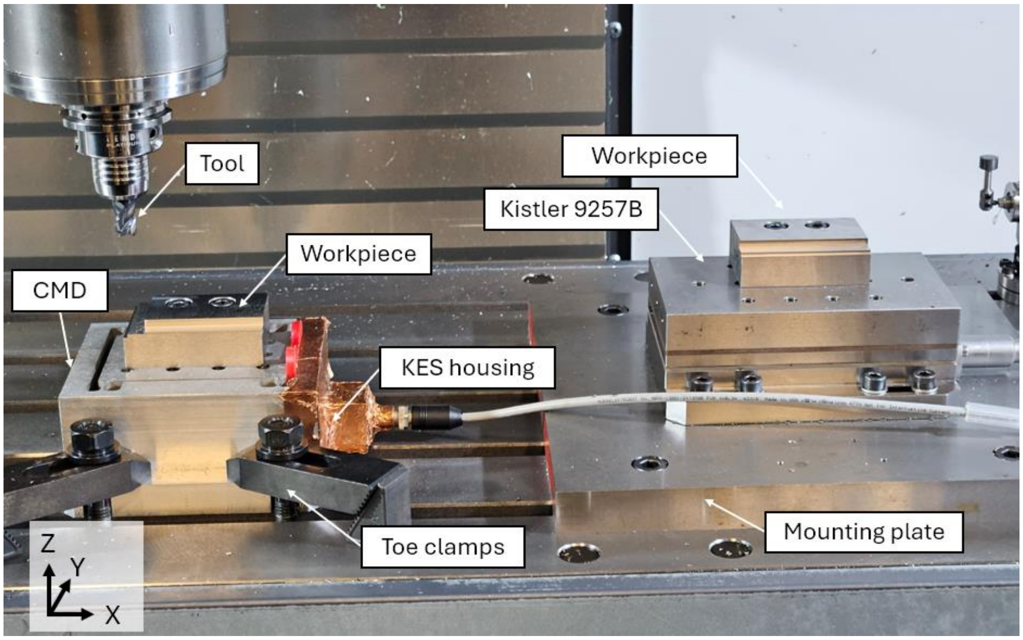

Figure 4.4: Annotated setup of CMD, commercial dynamometer, and tool in the machining center.

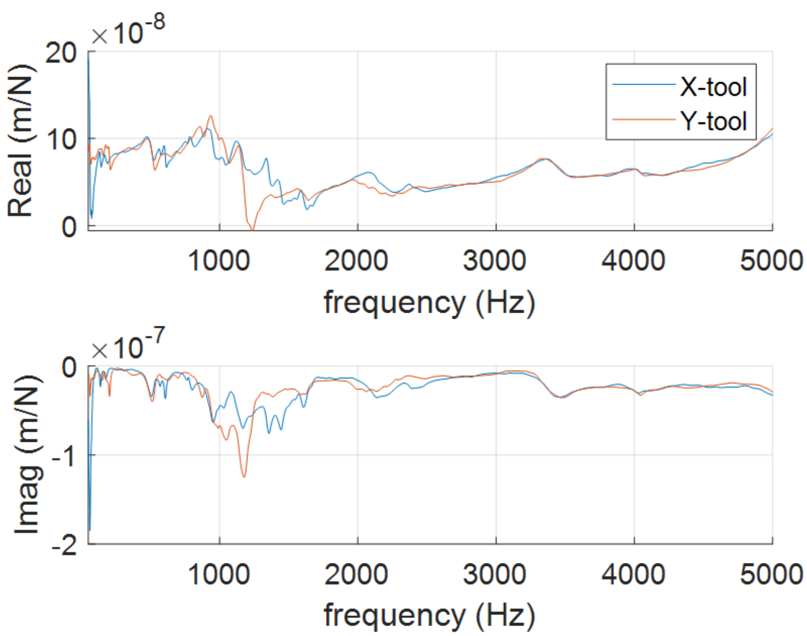

Figure 4.5: Receptance FRF for Kennametal 0.5 in. diameter tool in hydraulic holder.

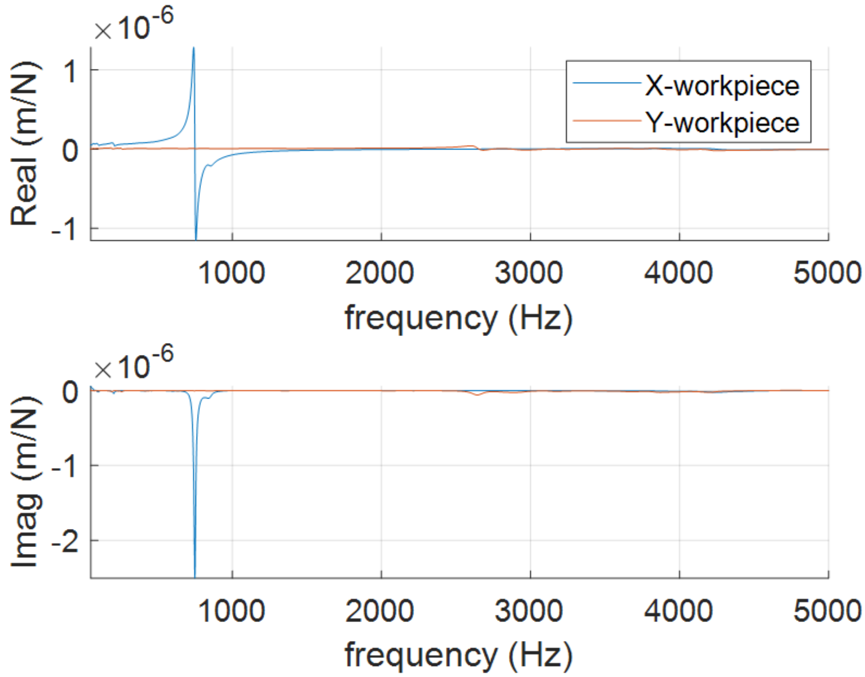

Figure 4.6: Receptance FRF for CMD with aluminum 6061-T6 workpiece.

accelerometer are positioned at the top corner of the workpiece. The initial SDOF modal parameters derived from the FRF of the CMD are as follows; f_n = 747 Hz, k = $1.95*10^7$ N/m, and ζ= 0.96 %.

Due to changes in the setup and materials, the specific calibration coefficient (α) mentioned in Chapter 3 had to be determined. Since all cutting will be conducted at one vertical level, only a single value is needed for the current tests. Therefore, only the FRF measurement utilizing the KES as the response is needed in addition to the already conducted FRF from the top of the workpiece. Using this method and comparing the modal stiffness values of both FRFs results in an α value of 85.9%. This value was applied to all measurements obtained from the KES for the 6061 aluminum cuts. The final tap test conducted was a force-to-force FRF conducted on the commercial dynamometer utilizing the impact hammer as the input force while measuring the output of the dynamometer for the response in the appropriate *x* and *y* machine directions. This was performed to compensate for the amplification effect of force around the natural frequency of the dynamometer [13]. The resulting FRF can be seen in **Figure 4.7**.

Stability lobe diagrams were then constructed utilizing the Fourier series approach previously described. Two different SLDs can be seen in **Figure 4.8** with one representing the flexible direction of the CMD aligned with the feed direction of milling, and the second where the flexible direction is perpendicular (cross-feed) to the direction of milling. The limiting axial depth of the direct feed and cross-feed stability maps is 5 mm and 3 mm respectively. This means that anything below 3 mm should result in stable cutting conditions for both orientations. An axial depth of 2 mm was selected to stay below the stability limit, but to select a proper spindle speed the tooth passing frequency consideration needs to be done.

Spindle Speed Considerations

To simulate typical cutting speeds for aluminum, a spindle speed range of 4k-6k rpm was established, but to determine what speed is best for the system the frequency content needs to be analyzed. For an initial guess, 5000 rpm was chosen since it lied in the middle of the previously defined range. It is found that the first four harmonics lie below the natural frequency with the fourth being at 667 Hz, which satisfies the first condition of at least three harmonics being below 747 Hz. The second condition is also satisfied, because even though the runout harmonic above

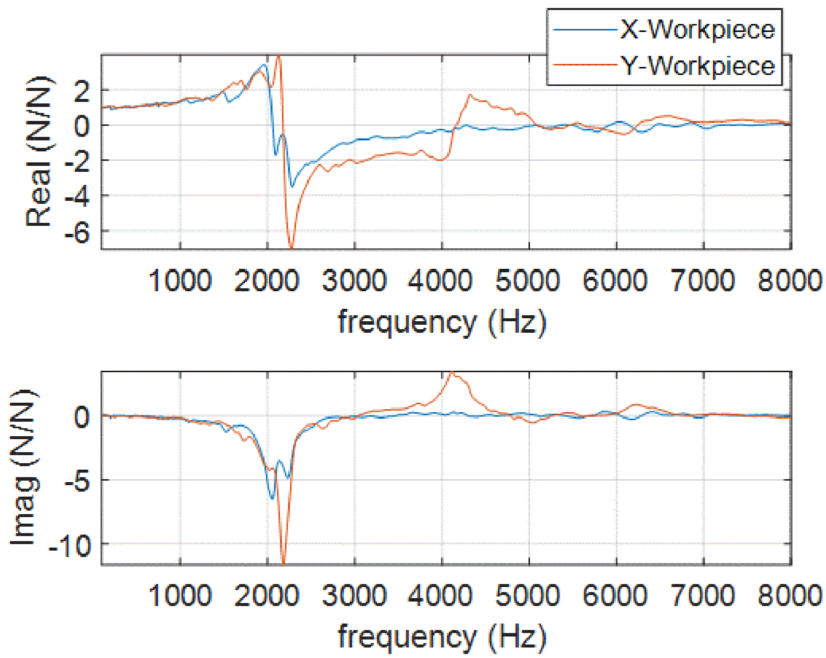

Figure 4.7: Force-to-force FRF for Kistler 9257B dynamometer with aluminum 6061-T6 workpiece.

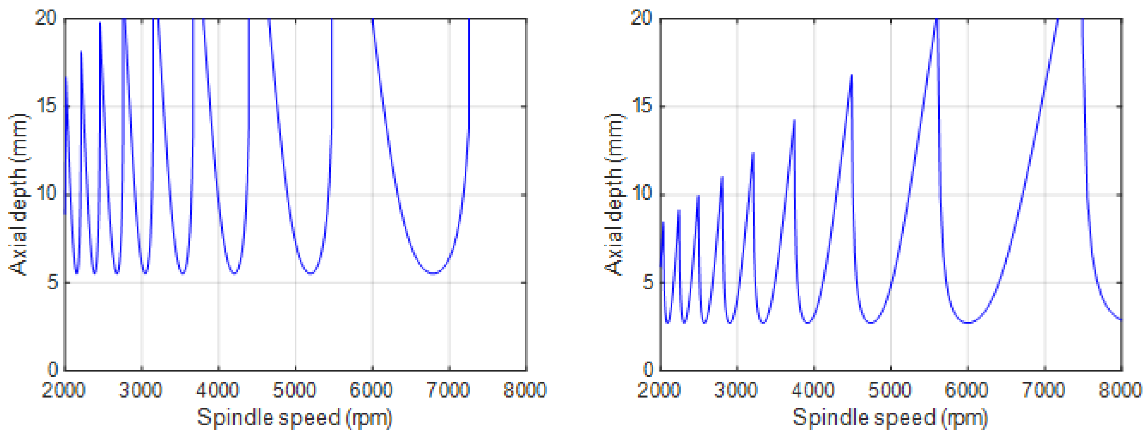

Figure 4.8: SLD for direct (left) and cross (right) feed directions.

the fourth tooth passing harmonic is 750 Hz, which is close to but not equal to 747 Hz natural frequency, there is very little content at the runout frequency. This is due to the minimal runout in the tool (only 2 μm), which results in lower frequency content compared to the tooth passing harmonics. Therefore, 5000 rpm will satisfy conditions needed for testing.

Initial Force Model

An initial mechanistic force model was constructed before cutting was performed firstly to ensure that the current cutting conditions will result in stable milling. Secondly, to ensure that the theoretical max displacement or force of the CMD would not be exceeded. The simulation is constructed with all of the previously defined parameters as well as the modal parameters derived from the FRFs performed on the tool and workpiece on the CMD. Two simulations were performed in a similar matter to the SLDs with one orienting the flexible direction of the CMD to the feed directions and one oriented to the cross-feed direction. The highest feed value of 0.2 mm/tooth was also chosen to simulate the maximum forces and displacement that will be seen during the trials. The four measurements taken from these simulations are the force and workpiece displacements in the x and y-directions and can be seen plotted in **Figure 4.9**. The maximum force is predicted below the 1500 N limit, and the displacement is within the 50 μm limit as well.

Data Collection and Filtering

The next step was to perform the test cuts on the commercial dynamometer and CMD. Five cuts were performed in sequence on the commercial dynamometer, then on the CMD in the y-direction, and finally in the CMD x-direction. There was a cleanup pass performed before each of the individual cuts to ensure that the surface left behind was not rough and that the tool would not rub on the floor of the part, which would introduce errors and inconsistencies. Measurements of the direct-feed (x) and cross-feed (y) forces were taken on the commercial dynamometer for each of the five feed per tooth values. The force signals directly from the Kistler 9257B are shown for the x and y-directions in **Figure 4.10**. As stated before, the natural frequencies of the system cause unwanted amplifications of the tooth passing frequency harmonics that need to be filtered out. To accomplish this, the measured force signals are converted into the frequency domain via fast Fourier transform (FFT).

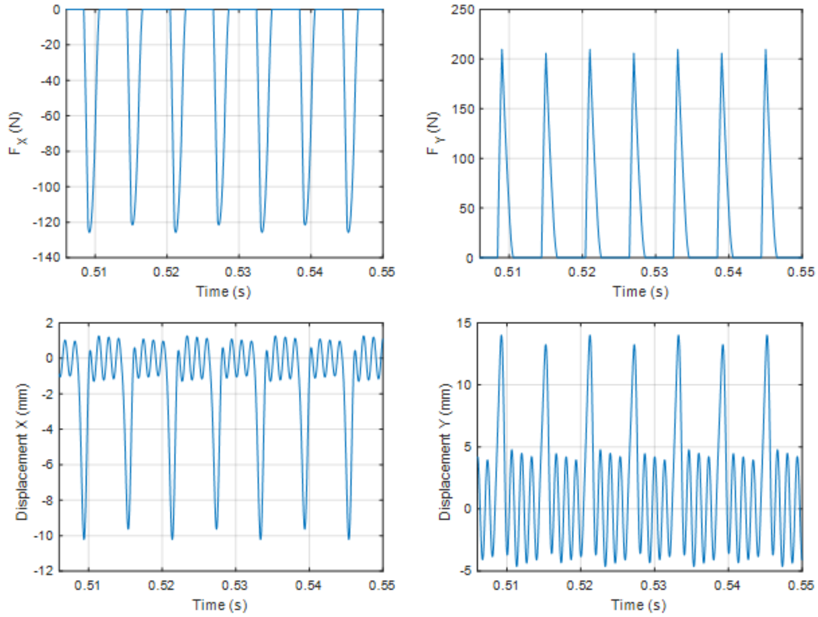

Figure 4.9: Mechanistic for model plots for force in *x* (top-left) and *y* (top-right), and workpiece displacements in the *x* (bottom-left) and *y* (bottom-right) directions at spindle speed of 5000 rpm and feed of 0.2 mm/tooth.

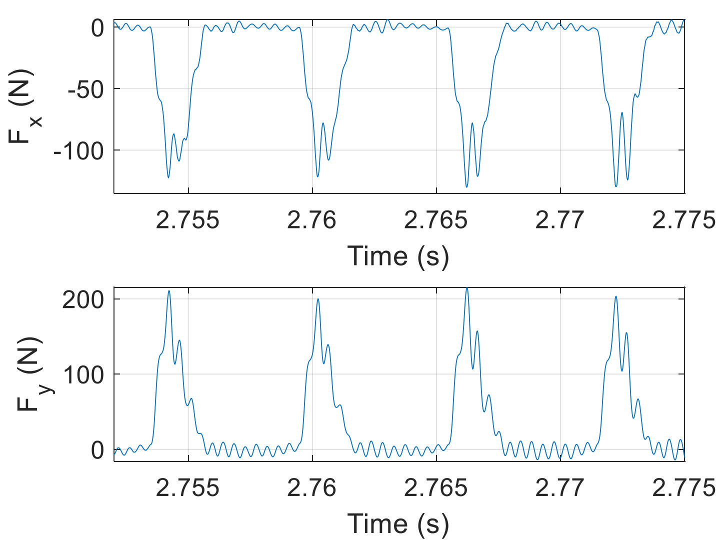

Figure 4.10: Unfiltered force signals from Kistler 9257B for Al 6061 at 0.150 mm/tooth and 5000rpm

Once in the frequency domain, the force-to-force FRF is inverted and applied to the measured signal along with the 2500 Hz low-pass filter. In **Figure 4.11** the attenuation of the natural frequencies is shown, with the tooth passing harmonics around 2-2.5 kHz being brought down to the normal levels of decay of the harmonics. That filtered force signal in the frequency domain is then converted back into the time domain utilizing an inverse FFT. The measured and filtered forces for the *x* and *y*-directions can be seen plotted over each other in **Figure 4.12**. It can be seen how the waviness in the signal, caused by the system's natural frequencies, is no longer present in the filtered signal while still maintaining the same form or shape of the signal. This filtered signal is closer to the actual force that was imparted on the system during cutting, and therefore the filtered signals will be used for any comparison or evaluation. The plotted signals only represent the 0.150 mm/tooth case, however all five feed per tooth values are evaluated in the same manner.

Once the measurements were completed on the commercial dynamometer, the same set of cuts were performed on the CMD in the *y* (cross-feed) and *x* (feed) directions, totaling 10 cuts on the CMD. A secondary FRF was taken on the CMD after the cross-feed measurements to obtain any shift in the natural frequency due to the removal of mass. The natural frequency of the system changed from 747 Hz to 748 Hz after the first five cuts while the stiffness and damping ratio stayed the same. The voltage signal from the KES was converted to a displacement by applying the 0.814 mm/V sensitivity value. Once converted to displacement, the compensation coefficient (α=0.859) was then applied to the measured displacement signal to obtain the actual displacement value of the workpiece. This compensated displacement can be seen plotted for the 0.150 mm/tooth cross-feed displacement in **Figure 4.13**. A DC offset of approximately 161 μm can be seen in the region where no cutting is taking place. This is due to the nature of the KES signal being measured from the center of its linear range, and the total range of measurement of the KES is approximately 320 μm. This offset value was then subtracted from the signal to get a true displacement signal that is centered around zero. A section of this data is shown in **Figure 4.14**, with two rotations of the tool plotted. The displacement signal here is similar to the predicted displacement in the initial force model, with defined tooth engagement and a section of free vibration when a tooth is not engaged. To be able to compare values to the filtered

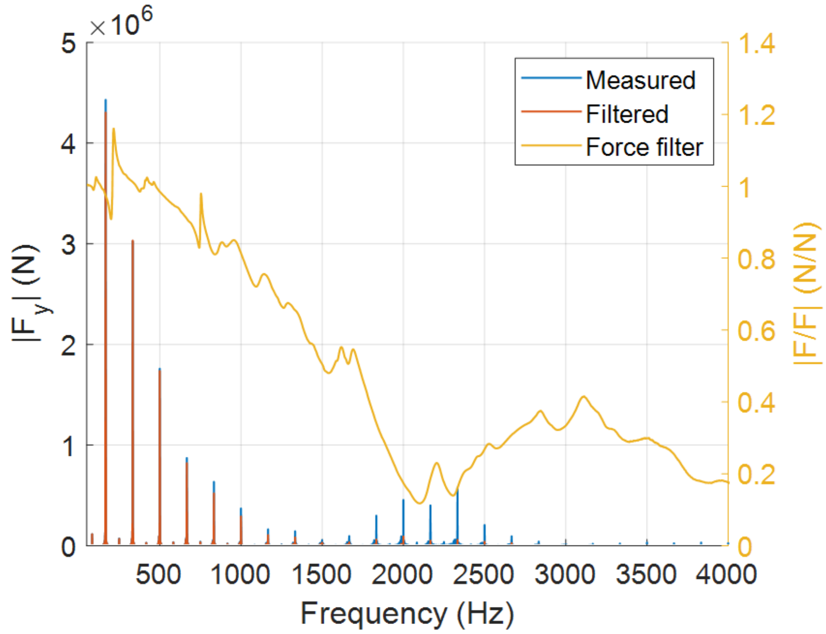

Figure 4.11: Force-to-force filter applied to *y*-direction force signal.

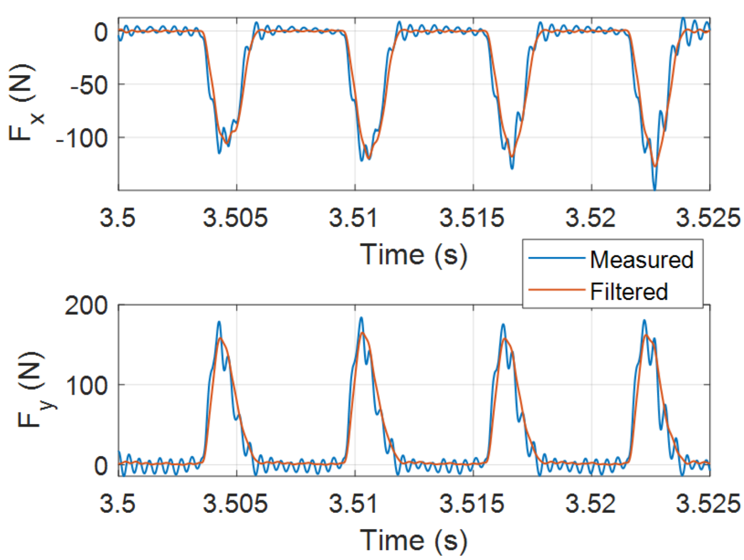

Figure 4.12: Filtered force signals from Kistler 9257B for Al 6061 at 0.150 mm/tooth and 5000rpm.

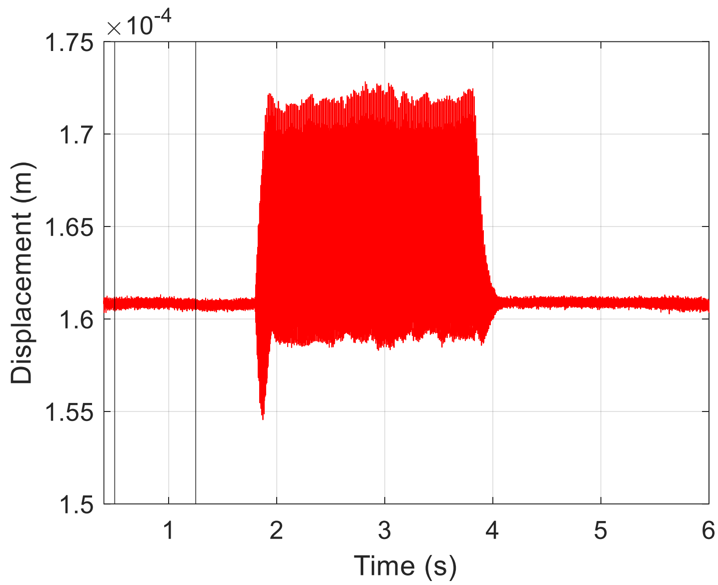

Figure 4.13: Compensated displacement signal for CMD y-feed for Al 6061 at 0.150 mm/tooth and 5000 rpm.

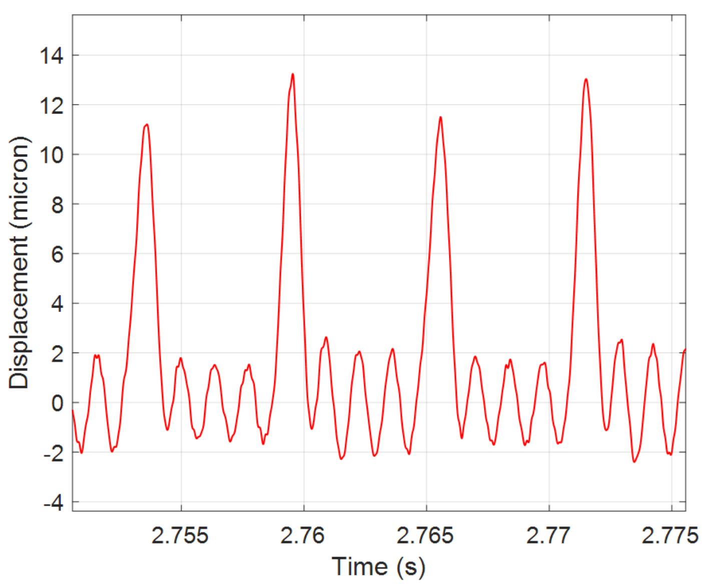

Figure 4.14: Adjusted displacement signal from CMD for Al 6061 at 0.150 mm/tooth and 5000rpm.

commercial dynamometer forces, structural deconvolution needs to take place.
This approach, as previously described, is applied similarly to the force-to-force filtering that was performed on the commercial dynamometer measurement. The actual displacement can then be converted from the time domain to the frequency domain via FFT. The SDOF FRF of the CMD is then inverted and a 5th order 850 Hz lowpass filter is applied to create the inverted force filter. The inverse force filter is applied to the displacement signal in the frequency domain to then obtain the force in the frequency domain, as shown in **Figure 4.15**. The deconvolved force can then be converted back into the time domain utilizing an inverse FFT. In **Figure 4.16** the deconvolved force in the time domain for the cross-feed direction is shown. This process is repeated nine more times for the four other cross-feed and five direct-feed measurements. The deconvolved force for the direct-feed direction at 0.150 mm/tooth is shown in **Figure 4.17**.

Force Comparison

With both sets of force measurements filtered, a proper comparison can be completed. The signals for the feed (x) and cross-feed (y) directions are plotted over each other for the force-filtered commercial dynamometer (Kistler) signals and the deconvolved CMD force at the same 0.150 mm/tooth feed rate in **Figure 4.18**. In **Figure 4.19** it is shown the comparison of all five feed values for the x-direction forces and **Figure 4.20** shows the y-direction force comparison. To analyze the data further, the data was broken up into sections of one tool rotation so that a mean and standard deviation of the mean cutting force values could be taken. Each data set contained 0.75 seconds of data, and with the tool spinning at 5000 rpm, each data set would contain about 60 rotations to analyze. **Figure 4.21** shows the parsed data sets with all 60 rotations of the CMD and Kistler measurements plotted over each other, as well as a detailed view at the peak of the force. This is used to visualize the spread of force values over a single test cut which is especially useful for materials like aluminum where improper chip evacuation can lead to variations of max force values over the entire cut. The mean value of the force over each rotation was taken, and from that set of values a mean and standard deviation of the mean forces could be calculated. **Table 4.3** shows all of the mean values and their standard deviations for All tests completed with the two fluted tool on aluminum 6061-T6. **Figure 4.22** shows these same values plotted out over the five feed per tooth values.

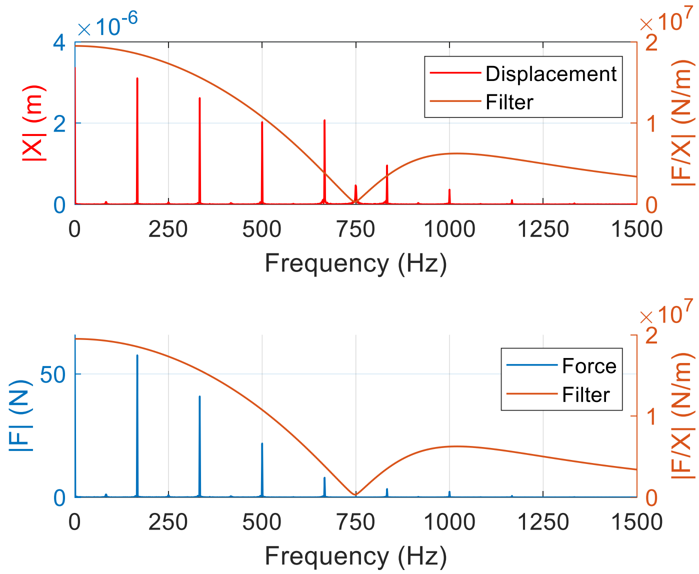

Figure 4.15: (Top) KES displacement signal in the frequency domain plotted with inverse force filter, (bottom) deconvolved force in frequency domain.

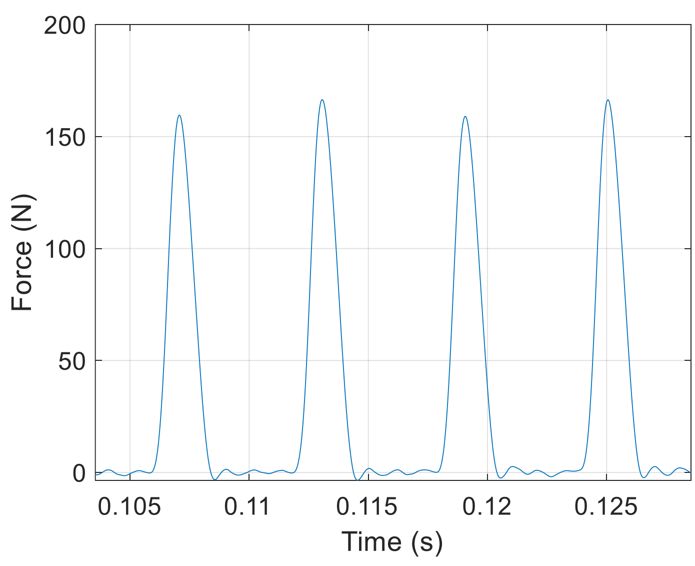

Figure 4.16: Deconvolved force for cross-feed direction from CMD for Al 6061 at 0.150 mm/tooth and 5000rpm.

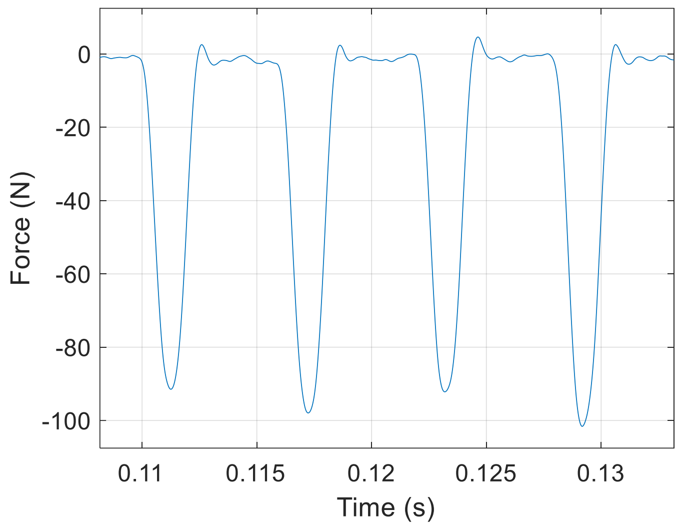

Figure 4.17: Deconvolved force for direct-feed direction from CMD for Al 6061 at 0.150 mm/tooth and 5000rpm.

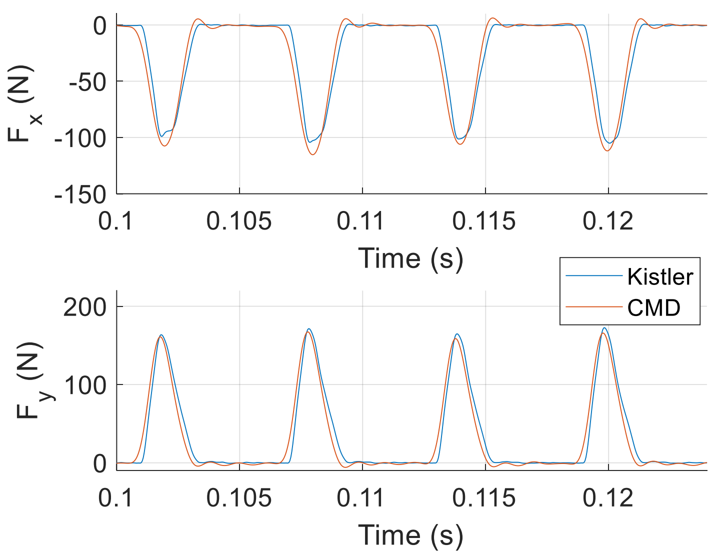

Figure 4.18: Comparison of force signals for both systems at 0.150 mm/tooth and 5000 rpm.

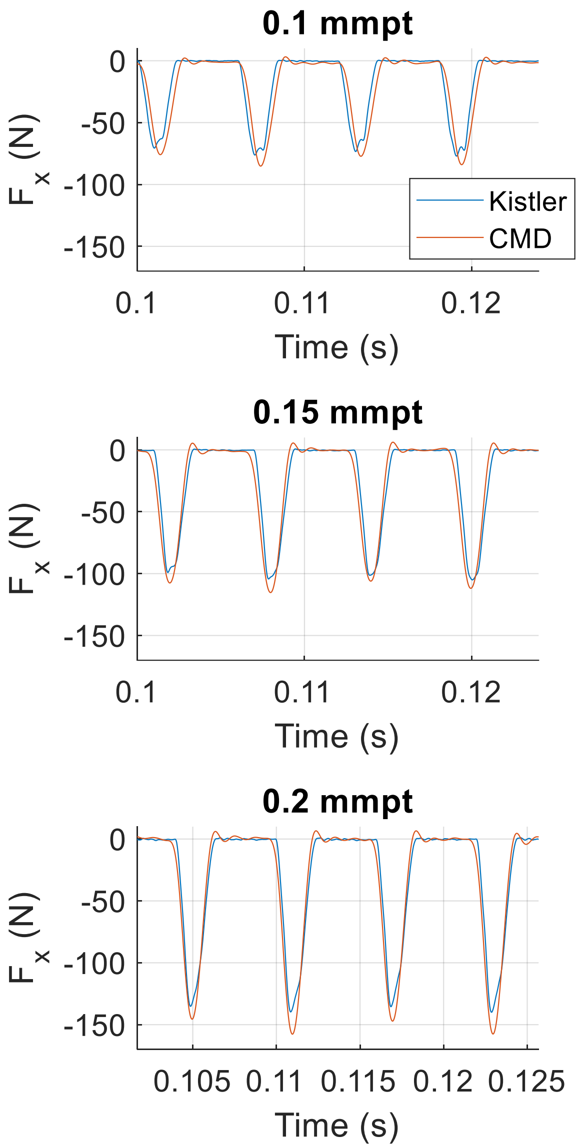

Figure 4.19: Comparison of five feed values for the *x*-direction forces for the CMD vs. commercial dynamometer for aluminum 6061.

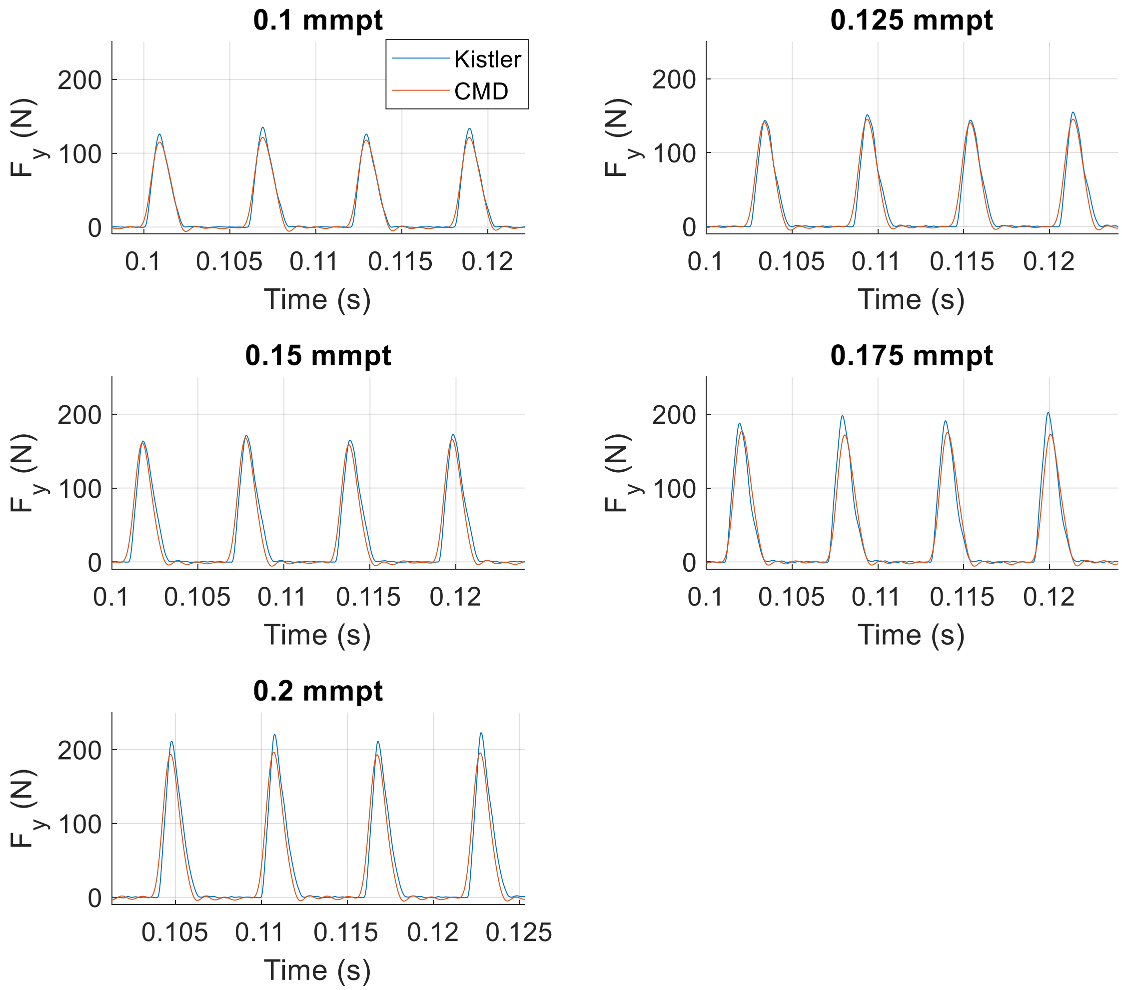

Figure 4.20: Comparison of five feed values for the *y*-direction forces for the CMD vs. commercial dynamometer for aluminum 6061.

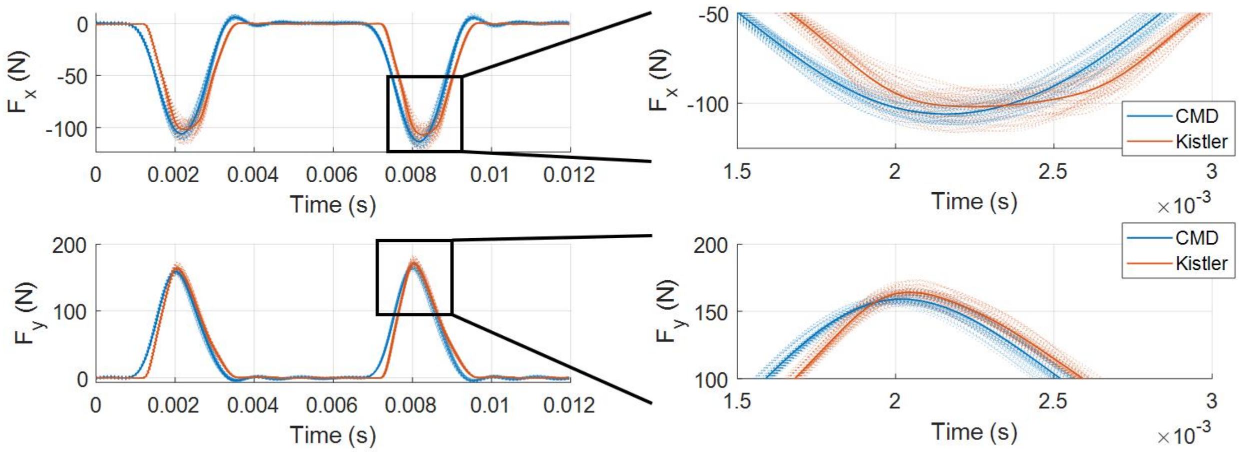

Figure 4.21: Sixty rotations of each force signal plotted over one rotation of the tool for both systems at 0.150 mm/tooth and 5000 rpm.

Table 4.3: Means and standard deviations of the mean force values for two fluted tool on Aluminum 6061-T6.

FPT (mm)	F_x (N) Kistler	F_x (N) CMD	F_y (N) Kistler	F_y (N) CMD
0.1	-17.01 ± 0.45	-17.18 ± 1.00	24.23 ± 0.34	23.90 ± 0.91
0.125	-19.94 ± 0.52	-19.67 ± 0.95	28.06 ± 0.60	29.19 ± 1.06
0.15	-23.11 ± 0.72	-23.10 ± 1.12	31.57 ± 0.55	31.62 ± 1.33
0.175	-26.14 ± 1.00	-26.74 ± 1.09	34.76 ± 1.13	35.23 ± 1.55
0.2	-29.20 ± 0.94	-29.59 ± 1.45	37.80 ± 0.63	37.57 ± 0.90

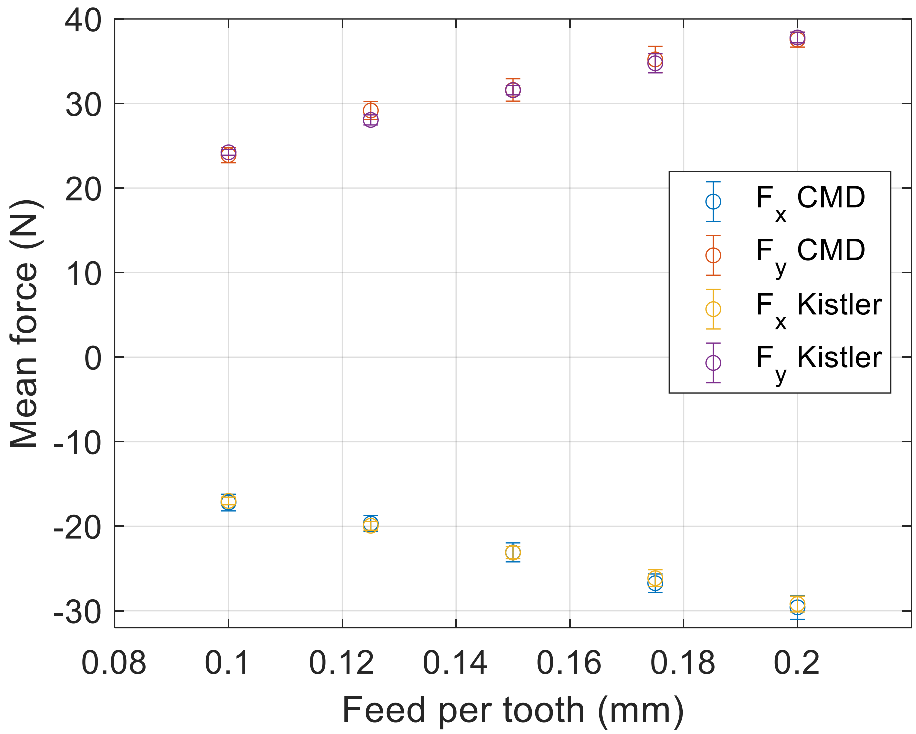

Figure 4.22: Means and standard deviations of the mean force values for two fluted tool on Aluminum 6061-T6.

Cutting Force Coefficients

After the mean force values were confirmed to be within expected range between the commercial dynamometer and the CMD, the average force linear regression algorithm was applied. The Monte Carlo sampling method was used to calculate the mean and standard deviation of the cutting force coefficient values. The inputs for the sampling method was the ten mean forces for the *x* and *y*-directions as well as the other variables needed for the average force linear regression method, and the outputs would be the CFC values. The values for the CFCs were calculated 10000 times, with each time the ten mean force values (five direct-feed and five cross-feed) being selected as a random value from a normal distribution based on the calculated means and standard deviations of each value sown in **Table 4.3**. For example, at 0.150 mm/tooth feed on the CMD, the mean force in the feed direction was selected from a normal distribution centered at -23.1 N with a standard deviation of 1.12 N, and the force in the cross-feed direction was from a normal distribution centered at 31.62 N with a standard deviation of 1.33 N. A new value was generated for each mean force value for each calculation, and the CFCs are stored to be used. After the 10000 calculations were completed, a mean value and standard deviation was calculated for each of the CFCs (k_n, k_t, k_{ne}, k_{te}, K_s, and β) and are shown in **Table 4.4**. For this case all of the values line up well, with each CFC value from the CMD falling within one standard deviation of the mean value gathered from the commercial dynamometer. With the CFC values determined from the Monte Carlo method, analysis can proceed to the final simulation of the mechanistic force model.

Table 4.4: CFC values for a two fluted tool on Aluminum 6061-T6.

	kt (N/mm^2)	kn (N/mm^2)	kt (N/mm)	kne (N/mm)	Ks (N/mm^2)	Beta (degrees)
CMD mean	905.15	249.22	16.47	17.67	941.61	74.55
CMD Stdv	74.69	68.63	4.30	3.89	71.28	4.41
Kistler mean	886.74	271.77	17.20	16.22	928.52	72.93
Kistler Stdv	45.88	41.95	2.47	2.14	43.32	2.76

Simulated Mechanistic Model Comparison

With all the final values calculated, a proper comparison between the measured forces and simulated mechanistic force model could be done. **Table 4.5** summarizes all of the variables needed to construct the simulation and where they were determined or calculated. The variables for the tool are specified by the manufacturer based on the tool the operator of the test choses, and the variables labeled “Operator determined” are chosen by the operator based on experience or the specific effects to be measured. With the cutting force coefficients finally calculated for the current tool-workpiece combination, the last variable can be set in the simulation. All CFC values used in simulations will be from the CMD deconvolved force values to test the ability to use the CMD values for a simulation construction. The updated force model values can be seen plotted against the CMD deconvolved forces for the 0.150 mm/tooth feed values in **Figure 4.23**. Since the model is fully defined to the current system, there is a very good agreement in the force values and shapes.

One discrepancy between the deconvolved forces and the simulated forces is the sharpness and resultant difference of amplitude of the peak forces in the cross-feed (y) direction. The deconvolved filtered forces from the CMD have peaks that are very rounded and not as defined as the peaks shown in the force model as shown in **Figure 4.24**. This can be explained with the frequency content of the signals. When constructing a Fourier series of sawtooth waves, which share a similar shape to the cross-feed forces, it is the higher order frequency components of the series that control how sharp the peaks of the sawtooth are. As higher order coefficients (higher frequencies) are used for the analysis, the resulting series has sharper and sharper peaks. For the CMD force signals, there is the lowpass filter that is reducing the amplitude of the noise and potential force content at higher frequencies, leading to rounder peaks. There is no lowpass filter on the simulated force in the force model, so the higher frequency content is not attenuated and as a result the peaks are able to stay sharp. The **Figure 4.25** shows the frequency content of the simulated force in the cross-feed direction compared to the frequency content of the deconvolved CMD cross-feed force. There is more content at frequencies higher than the 747 Hz natural frequency for the simulated force which leads to the sharper force peaks compared to the CMD.

Table 4.5: Variables used in mechanistic force model.

Variable	Units	Method of capture
Tool diameter	mm	Mfg. specified
Number of teeth	#	Mfg. specified
Helix angle	degree	Mfg. specified
Tooth spacing	degree	Mfg. specified
Tooth runout	micron	Dial indicator
Radial DoC	mm	Operator determined
Milling direction	up or down	Operator determined
Modal Parameters (ω_n, k, ζ)	Hz, N/m, %	Modal tap test
Feed per tooth	mm/tooth	Operator determined
Axial DoC	mm	Stability mapping
Spindle speed	rpm	Stability mapping
CFCs	N/mm^2 or N/mm	Linear regression

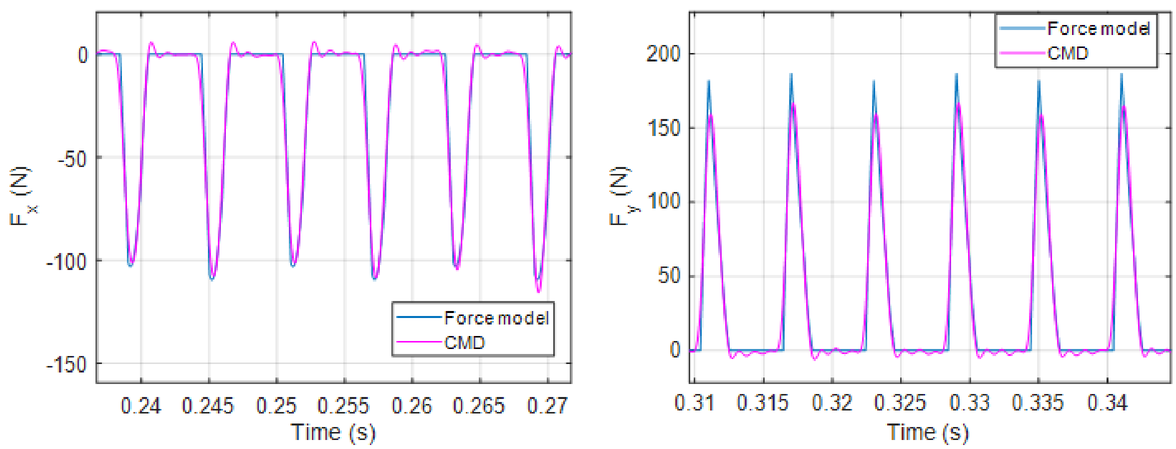

Figure 4.23: Force model and deconvolved force comparison for aluminum 6061-T6 at 5000 rpm and 0.150 mm/tooth.

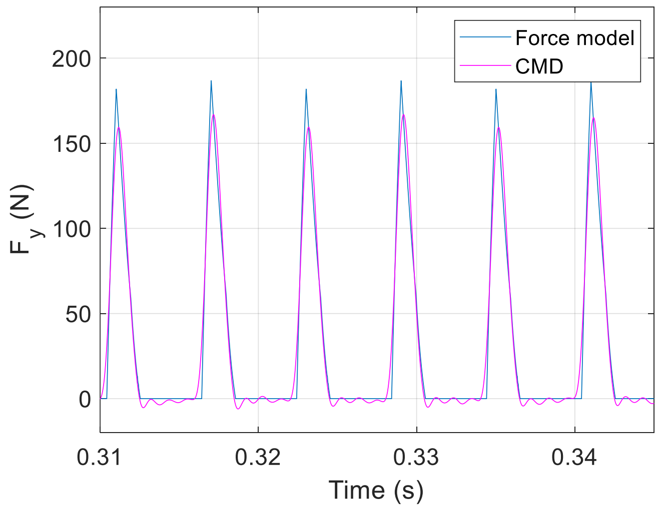

Figure 4.24: Time-domain force model and deconvolved force signals for the cross-feed direction force at 5000 rpm and 0.150 mm/tooth.

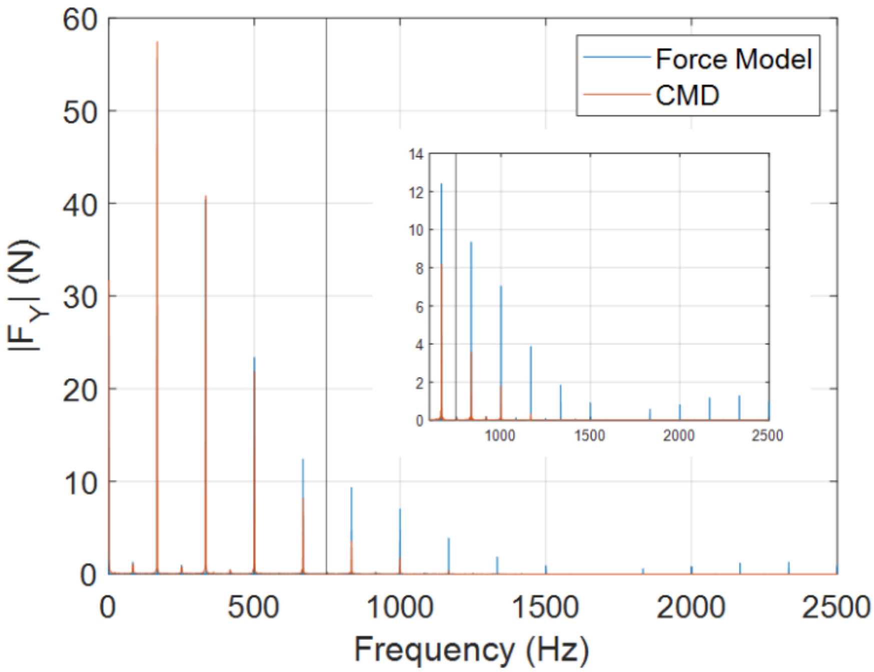

Figure 4.25: Frequency-domain force model and deconvolved force signals for the cross-feed direction force at 5000 rpm and 0.150 mm/tooth

However, if the same 850 Hz lowpass filter is applied to the simulated force model, these higher frequency peaks are attenuated to the same degree as the deconvolved force. The post-filtered frequency-domain content is plotted in **Figure 4.26** for the force model vs. the deconvolved force, which shows the reduction of frequency content above the 850 Hz filter. When looking at the filtered time-domain content, this leads to a less defined peak on the max force in the *y*-direction which matches almost perfectly with the deconvolved max force peaks. This comparison is shown in **Figure 4.27**, in which the max force and shape of the force model and deconvolved force signals match closer than before. This effect is not seen as prevalent in the direct feed forces seen in **Figure 4.23**, because the forces in that direction do not have the same sharp peaks or higher frequency content that that cross-feed direction does.

Prediction of CMD Frequency Response

The natural frequency of a SDOF system depends on the modal mass and spring stiffness of the system. While the stiffness of the flexure does not change for a specified workpiece, the mass of the system does change as material is milled away during the test cuts. Since frequency is inversely related to the mass of the system, as mass is removed in this manner, the natural frequency of the system increases. Following the initial study, another set of tests was conducted to determine if the natural frequency shift can be predicted based on the initial FRF, density of material being milled, and the volume of material being milled. If it is able to be predicted, the calculated shifts would assist with the ease of taking measurements with the system, since only one FRF would need to be conducted for any number of cuts being taken as long as the total material removed is tracked. Opposed to having to take an FRF measurement before each cut to determine the frequency shift of the system, which takes away time and resources. To be able to experimentally see a change in frequency during a normal amount of material removal, a 1018 stainless steel workpiece was chosen because of the higher density compared to aluminum workpieces. The workpiece was set up in a similar manner to the cutting tests described above. A block of roughly 3x2x1 inches was used for the experiment. The block's measured mass was 745.3 g, and the actual dimensions were 80.8 mm length, 50.8 mm depth, and 24.9 mm in height. These values were used for measuring the volume of material removed for the test cuts. The density of the sample was calculated to be 7.65 g/cm^3 using the measured mass and volume.

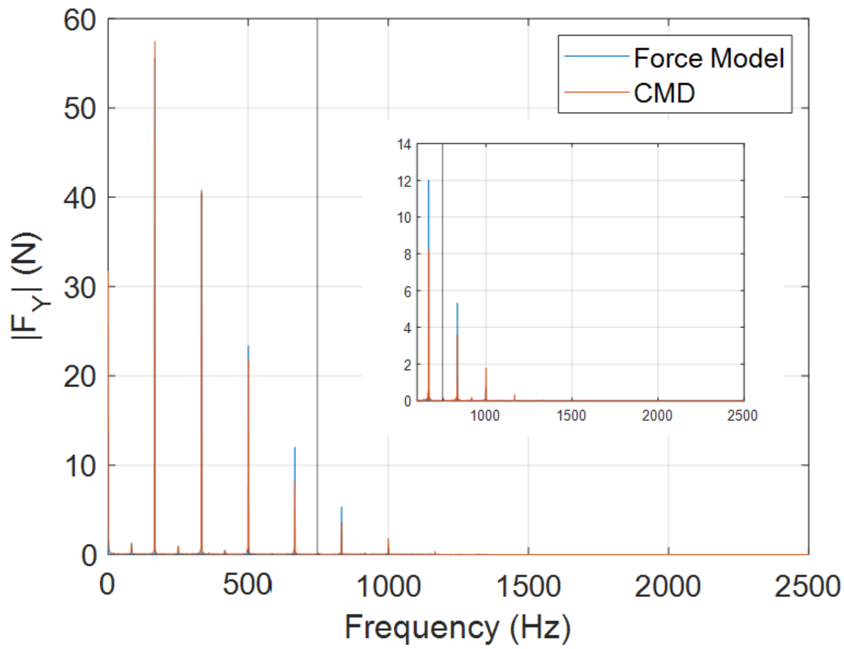

Figure 4.26: Frequency-domain filtered force model and deconvolved force signals for the cross-feed direction force at 5000 rpm and 0.150 mm/tooth.

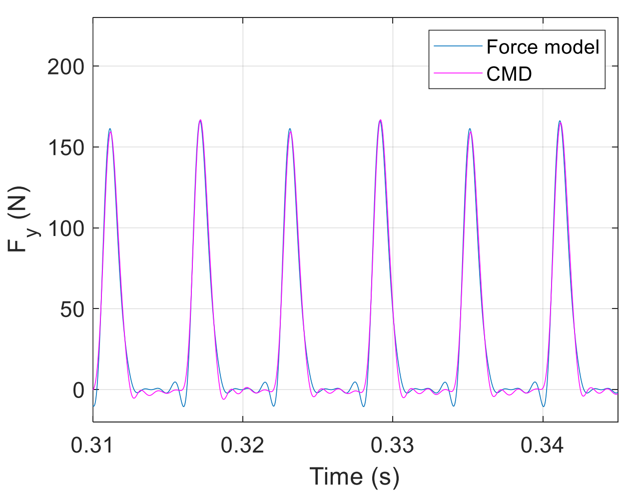

Figure 4.27: Time-domain filtered force model and deconvolved force signals for the cross-feed direction force at 5000 rpm and 0.150 mm/tooth.

Material was removed from the workpiece over ten test cut preformed over the length of the block, each having a 2 mm radial and 5 mm axial depth of cut. This resulted in each cut removing approximately 0.824 cm^3 of material. Using the actual density of the sample, it was calculated that each cut would remove approximately 6.31 grams of material from the workpiece. Tap testing was conducted before each test cut and after the last to determine the modal parameter change between each test. **Figure 4.28** shows the workpiece set up on the CMD. The accelerometer would be left on the workpiece during each test to minimize any errors that would arise from inaccurately replacing it, and a spot was marked on the opposing side of the workpiece to act as a target for the impulse hammer hits. The FRFs are shown for all 11 tap tests performed in **Figure 4.29**, and there is a visual shift in the SDOF natural frequency of the system as material is removed in between each FRF. The width and heights of the peaks in the real and imaginary portions change very little, which means the damping and stiffness values respectively are not changing between tests. This is crucial to understanding that any change in frequency should only be a result of a change in mass. The relationship between natural frequency, stiffness, and mass is shown in equation 4.3 and is used to calculate the modal mass of the system for each test.

$$\omega = \sqrt{\frac{k}{m}} \tag{4.3}$$

Where ω is the natural frequency in radians, and mass is measured in kilograms. The initial measured modal parameters were f_n = 633.2 Hz, $k = 1.99*10^7$ N/m, and ζ = 2.56 %. Using these values results in an initial modal mass of 1.263 kg. A new modal mass was calculated using the natural frequency and stiffness after every test cut to find the difference in mass between the test cuts. All of the above-mentioned values are shown in **Table 4.6** for the 11 FRFs performed. The rightmost columns show change in the modal mass between each test and the calculated predicted change in mass based on the volume of material removed. While the modal mass change between each test does not equal the 6.309 g predicted change, the average value of all the modal mass changes is 6.348 g with a standard deviation of 3.29 g. The large spread in data could be due to either human error in the tap testing or lack of precision in the measurements and processing. However, the mean value and the final value have an error of only 0.68 % from the

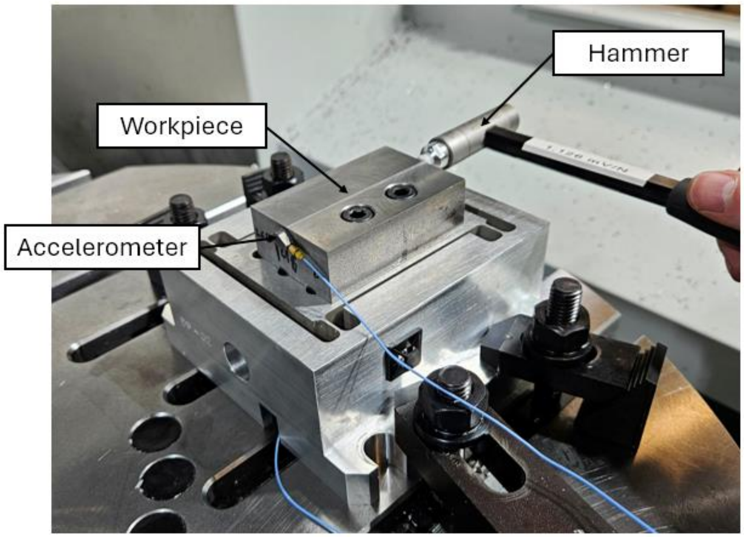

Figure 4.28: Setup of 1018 steel workpiece on CMD for the frequency shift prediction.

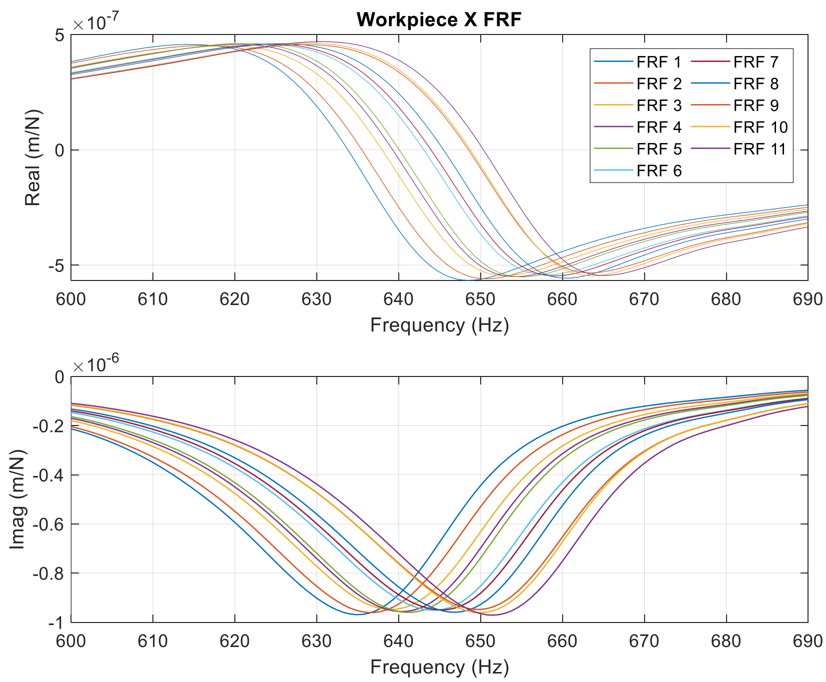

Figure 4.29: FRF of 1018 steel workpiece for 11 tests displayed near the natural frequency of the SDOF.

Table 4.6: Modal parameters of the SDOF and changes in mass between each test.

Test #	f_n (Hz)	k (N/m)	ζ (%)	Modal mass (kg)	Modal mass Change (g)	Actual mass change (g)
1	633.2	1.997E+07	2.56	*1.2629*	0.000	0.000
2	635	1.997E+07	2.59	*1.2557*	7.149	6.309
3	637.4	1.997E+07	2.61	*1.2463*	9.438	6.309
4	638.7	1.997E+07	2.59	*1.2412*	5.068	6.309
5	639.6	1.997E+07	2.56	*1.2377*	3.491	6.309
6	642.5	1.997E+07	2.61	*1.2266*	11.148	6.309
7	643.4	1.997E+07	2.61	*1.2231*	3.429	6.309
8	644.9	1.997E+07	2.59	*1.2175*	5.683	6.309
9	647.96	1.997E+07	2.61	*1.2060*	11.472	6.309
10	648.2	1.997E+07	2.59	*1.2051*	0.893	6.309
11	649.74	1.997E+07	2.56	*1.1994*	5.706	6.309
				Total	**63.477**	**63.089**

predicted values, with the final total modal mass change being 63.477 g and the predicted total change being 63.089 g.

With the method proved to be successful for the SDOF system, a simulation can be written that can utilize an initial FRF, the density of material, and the area of material being cut to predict the change in modal mass, and therefore the change in natural frequency over a series of tests. The following is a simple explanation of the simulation that be broken up into four major steps:

1. The initial modal parameters f_n, k, and ζ are set. The modal mass is calculated from these values.
2. The density of the material and cut parameters are set, which include the axial and radial depth of cut, length and number of cuts performed, and the size of any 'cleanup' passes.
3. The modal mass change between each cut is calculated utilizing the volume of a cut times the density of the material. This step is repeated for the specified number of times with a cleanup pass being calculated between cuts as specified.
4. The modal mass and stiffness values are used to calculate the new natural frequency after the specified number of cuts.

The trial was performed with the data for the H13 steel cutting tests. The modal parameters are as follows: f_n = 627.52 Hz, $k = 1.99*10^7$ N/m, and ζ = 1.54%. The density of the sample was calculated to be 7.63 g/cm^3, and the measured length and width of the sample was 7.745 cm and 5.130 cm respectively.

For this specific scenario five cuts and one cleanup pass is performed in the *y*-direction, then five more cuts and a cleanup in the *x*-direction for the first tool, and then the same cuts are performed for the second tool on the same system. This leads to 24 total cuts including the cleanup passes. The system's FRF was measured first before any cuts were performed and after every cleanup pass, totaling to five FRF measurements. **Figure 4.30** shows the top view of the workpiece and how much material is removed for each of the cuts in either direction. The axial depth of all cuts was 2 mm, the radial depth of cut was 2 mm for the *y* and *x*-directions, and the cleanup pass was 0.254 mm radial depth. The volume of material removed was calculated for every single cut and stored so that the instantaneous change in frequency could be used as needed between each cut. However, for this test the natural frequency was calculated only after each of the four cleanup

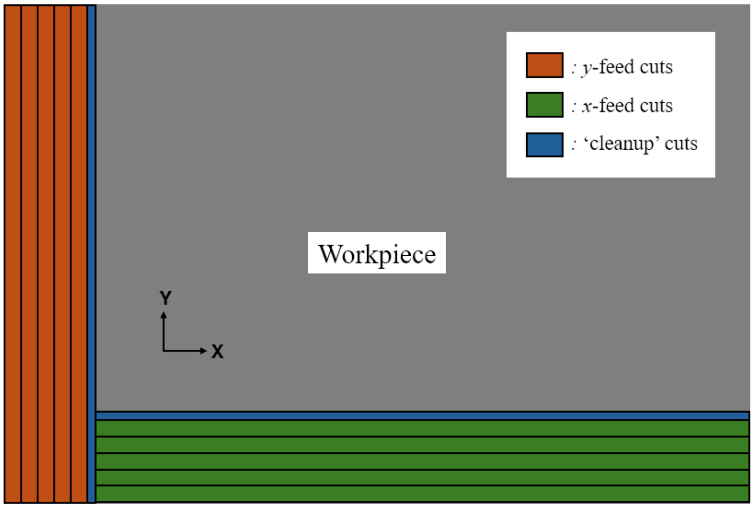

Figure 4.30: Area of cuts being performed for all cuts on the CMD system.

passes since it was seen that small volume/mass changes aren't as accurate in the predictions. **Table 4.7** shows the natural frequency values found using the FRF of the workpiece and the calculated prediction of change in natural frequency based on the mass removal calculations. The percent error for the first value is zero since the algorithm needs the initial natural frequency input for the first value, but the rest of the values are all within 0.1 % of the measured natural frequencies of the system.

Table 4.7: Measured natural frequencies and calculated natural frequencies using the modal mass change calculations.

Test #	**1**	**2**	**3**	**4**	**5**
FRF f_n (Hz)	627.52	629.81	632.48	634.38	637.82
Calculated f_n (Hz)	627.52	629.75	632.71	634.99	638.02
% Error	0.00%	0.01%	-0.04%	-0.10%	-0.03%

CHAPTER FIVE

EXPERIMENTAL RESULTS AND DISCUSSION

This section will go over the results found regarding the 24 different cutting conditions, from two different tools for twelve materials. The 12 materials are meant to cover a wide range of the most common materials used in a practical machining environment, and two different tools were chosen for each to be able to compare how different geometries or manufacturers of tools would affect the relative values. Reference **Table 4.1** and **Table 4.2** for the list of materials and tools specified for certain materials. Any material abbreviations will be the following: aluminum (Al), low carbon steel (LCS), stainless steel (SS), and titanium (Ti). Simplified identifiers will be used for the tools as well. For the aluminum tools the two fluted cutter will be referred to as “tool #2” and the three fluted tool will be referred to as “tool #1”, and for the steels and titanium the Kennametal tool will be “tool #4” and the Accupro tool will be referred to as “tool #3”. **Table 5.1** shows all of the SDOF modal parameters and corresponding α value for all of the trials.

Mean Forces

The main objective of this research is to be able to accurately gather the cutting force coefficient values to construct a mechanistic force model utilizing only the CMD without the need for the high-cost commercial dynamometer. The mean force values that are needed for the CFCs are compared between the CMD and the Kistler commercial dynamometer. The values obtained from the commercial dynamometer are the expected/actual force values during milling. Any percent errors obtained utilize the commercial dynamometer as the expected values and the CMD values are the observed values. **Table 5.2** through **Table 5.5** shows the mean force value comparison for one of each general material group: aluminum, low carbon steel, stainless steel, and titanium. The rest of the tables are shown in the appendix for all materials and tools. Most of the mean force values have a percent error around ±3 percent in both the feed and cross-feed directions. Only a few values lie outside of this range, with the highest percent error being 8 % for one cut in the aluminum 2024 cross-feed direction. This indicates that the system and proposed method for collecting the cutting force values on the CMD can yield results that are within a reasonable margin of error. Since the error is also above and below the measured values from the commercial dynamometer, this error can be due to the stochastic nature of milling.

Table 5.1: SDOF modal parameters for every workpiece-tool combination on the CMD and corresponding compensation coefficients α.

Material	Tool #	f_n (Hz)	k (N/m)	ζ(%)	α (-)
2024 aluminum	1	747	2.00E+07	0.97	0.890
2024 aluminum	2	750	1.95E+07	0.96	0.890
6061 aluminum	1	744	2.00E+07	0.90	0.849
6061 aluminum	2	750	1.95E+07	0.96	0.852
7075 aluminum	1	745	2.00E+07	0.96	0.860
7075 aluminum	2	744	1.94E+07	0.87	0.861
1018 steel	3	630	1.94E+07	1.56	0.934
1018 steel	4	641	1.98E+07	1.47	0.934
4140 steel	3	630	1.93E+07	1.56	0.876
4140 steel	4	626	1.94E+07	1.62	0.862
A36 steel	3	632	1.94E+07	1.55	0.923
A36 steel	4	626	1.94E+07	1.53	0.924
H13 steel	3	631	1.99E+07	1.55	0.892
H13 steel	4	627	1.99E+07	1.54	0.892
303 stainless steel	3	631	1.98E+07	1.56	0.876
303 stainless steel	4	628	1.94E+07	1.64	0.878
304 stainless steel	3	627	1.95E+07	1.55	0.866
304 stainless steel	4	622	2.00E+07	1.55	0.866
316 stainless steel	3	628	1.97E+07	1.57	0.947
316 stainless steel	4	922	1.94E+07	1.65	0.930
440 stainless steel	3	631	1.98E+07	1.56	0.876
440 stainless steel	4	628	1.94E+07	1.64	0.878
6Al-4V titanium	3	708	1.99E+07	1.59	0.956
6Al-4V titanium	4	705	1.99E+07	1.58	0.970

Table 5.2: Al 2024, Kennametal two-flute tool mean forces for CMD and commercial dynamometer.

FX mean (N)				**FY mean (N)**			
FPT (mm)	**Kistler**	**CMD**	**% Error**	**FPT (mm)**	**Kistler**	**CMD**	**% Error**
0.1	18.35	18.47	0.6%	**0.1**	27.39	29.58	8.0%
0.125	21.86	22.80	4.3%	**0.125**	29.91	30.23	1.0%
0.15	25.37	25.69	1.3%	**0.15**	34.32	35.94	4.7%
0.175	28.88	28.50	-1.3%	**0.175**	38.89	39.98	2.8%
0.2	32.47	31.91	-1.7%	**0.2**	42.85	43.68	1.9%

Table 5.3: LCS 1018, Kennametal four-flute tool mean forces for CMD and commercial dynamometer.

FX mean (N)				FY mean (N)			
FPT (mm)	Kistler	CMD	% Error	FPT (mm)	Kistler	CMD	% Error
0.1	-56.40	-55.59	-1.4%	**0.1**	87.81	88.17	0.4%
0.125	-67.84	-67.08	-1.1%	**0.125**	102.13	102.11	0.0%
0.15	-79.76	-78.56	-1.5%	**0.15**	115.50	114.17	-1.2%
0.175	-91.26	-90.59	-0.7%	**0.175**	129.00	129.65	0.5%
0.2	-103.06	-102.29	-0.7%	**0.2**	142.31	140.72	-1.1%

Table 5.4: SS 303, Accupro four-flute tool mean forces for CMD and commercial dynamometer.

FX mean (N)				FY mean (N)			
FPT (mm)	Kistler	CMD	% Error	FPT (mm)	Kistler	CMD	% Error
0.1	-62.09	-61.34	-1.2%	**0.1**	99.81	101.18	1.4%
0.125	-75.37	-74.94	-0.6%	**0.125**	113.44	112.61	-0.7%
0.15	-89.51	-88.11	-1.6%	**0.15**	128.46	130.54	1.6%
0.175	-104.05	-103.15	-0.9%	**0.175**	143.28	146.06	1.9%
0.2	-118.23	-119.01	0.7%	**0.2**	156.92	160.18	2.1%

Table 5.5: Ti6Al4V, Accupro four-flute tool mean forces for CMD and commercial dynamometer.

FX mean (N)				FY mean (N)			
FPT (mm)	Kistler	CMD	% Error	FPT (mm)	Kistler	CMD	% Error
0.1	-42.47	-42.37	-0.2%	**0.1**	95.44	94.11	-1.4%
0.125	-53.31	-52.35	-1.8%	**0.125**	110.10	108.87	-1.1%
0.15	-63.94	-61.62	-3.6%	**0.15**	122.48	117.90	-3.7%
0.175	-74.56	-72.58	-2.7%	**0.175**	133.29	123.98	-7.0%
0.2	-85.31	-82.84	-2.9%	**0.2**	143.19	134.81	-5.9%

Cutting Force Coefficients

As explained in chapter 2, the CFC values are solved by utilizing the mean force values of the series of cuts. Since a good agreement is seen for the mean forces on the CMD vs. the commercial dynamometer, there should follow a good agreement in the CFC values for the two. The Monte-Carlo simulation technique was applied again to all twenty-four workpiece-tool combinations to find the mean value and standard deviation of each CFC value. The tangential and normal cutting coefficients as well as their edge (rubbing) coefficients are show in **Table 5.6** as the mean value of the coefficient plus/minus one standard deviation of the coefficient. **Table 5.7** shows the same mean and standard deviation for the resultant cutting force coefficient (K_s) and angle (β).

It can clearly be seen that the values of the CFCs are both tool and workpiece dependent. Two different tools for one material have similar mean values but can differ by about 100 N/mm^2 in one direction or the other. Since some values are higher for tool#1 on one material and higher for tool#2 on another material, it is hard to say for certain that one tool will produce CFC values higher than another tool, at least for the tools selected in these trials. The same spread in mean values can also be seen for each material group. The aluminums, low carbon steels, and stainless steels have similar values to the other materials in their group but have a slightly larger spread of around 200-300 N/mm^2 at most. The difference in these values show that there is a dependance on both the specific tool and workpiece for each CFC value. A final note to make is a pattern in the standard deviations of the values. For the aluminum samples the range of standard deviation is 30-60 N/mm^2, whereas the steel samples have standard deviations of only 20-30 N/mm^2 even with higher mean values. This is most likely due to poor chip evacuation during milling of the aluminum. Since aluminum is more ductile than steel, when the chips are being sheared away they tend to want to stick to the tool more and lead to variations in the cutting forces each rotation of the tool. This is usually mitigated by using a coolant to fully lubricate the tool and workpiece, but since the KES is not waterproof, coolant could not be used for the test cuts.

The values shown in the tables are only for the CMD calculated CFC values, but to show how those values compare against the values obtained from the commercial dynamometer a bar plot was constructed. **Figure 5.1-5.3** shows the K_s and β values as the mean value with an error bar of

Table 5.6: Tangential, normal, and edge cutting coefficients for all workpiece and tool combinations performed on the CMD.

Material	Tool #	kt (N/mm^2)	kn (N/mm^2)	kt (N/mm)	kne (N/mm)
2024 aluminum	1	1030.4 ± 35.3	268.97 ± 44.78	21.30 ± 1.96	30.11 ± 3.01
2024 aluminum	2	963.8 ± 50.1	325.42 ± 54.89	21.10 ± 2.76	19.02 ± 3.50
6061 aluminum	1	848.9 ± 41.8	337.93 ± 36.95	17.70 ± 2.52	14.75 ± 2.24
6061 aluminum	2	905.2 ± 74.7	249.22 ± 68.63	16.47 ± 4.30	17.67 ± 3.89
7075 aluminum	1	818.5 ± 34.5	110.03 ± 43.83	30.77 ± 1.85	44.71 ± 2.85
7075 aluminum	2	1000.7 ± 51.0	289.65 ± 53.72	23.63 ± 3.00	32.81 ± 3.01
1018 steel	3	1742.8 ± 20.8	528.41 ± 18.02	23.13 ± 1.24	28.22 ± 1.00
1018 steel	4	1784.3 ± 22.1	669.25 ± 28.32	19.84 ± 1.10	24.11 ± 1.75
4140 steel	3	2066.2 ± 28.4	571.96 ± 27.74	30.65 ± 1.57	32.30 ± 1.60
4140 steel	4	1996.6 ± 27.1	615.95 ± 23.62	31.59 ± 1.60	38.75 ± 1.40
A36 steel	3	1844.5 ± 37.3	648.28 ± 24.94	30.03 ± 2.16	32.11 ± 1.16
A36 steel	4	1770.7 ± 24.8	659.49 ± 26.86	30.99 ± 1.40	37.51 ± 1.57
H13 steel	3	1877.9 ± 30.0	458.84 ± 25.37	22.92 ± 1.74	24.44 ± 1.44
H13 steel	4	1856.9 ± 22.4	566.46 ± 28.51	23.71 ± 1.24	27.30 ± 1.65
303 stainless steel	3	2038.5 ± 27.0	571.27 ± 33.11	18.53 ± 1.60	34.53 ± 1.92
303 stainless steel	4	1942.9 ± 19.4	743.69 ± 25.01	21.31 ± 1.15	32.40 ± 1.55
304 stainless steel	3	2036.8 ± 30.1	642.75 ± 26.87	25.78 ± 1.73	43.09 ± 1.40
304 stainless steel	4	2071.8 ± 23.7	688.40 ± 26.76	25.06 ± 1.26	49.40 ± 1.57
316 stainless steel	3	2165.3 ± 33.7	762.75 ± 30.28	24.47 ± 1.90	43.79 ± 1.67
316 stainless steel	4	2377.6 ± 28.4	960.57 ± 29.67	18.96 ± 1.72	48.79 ± 1.67
440 stainless steel	3	2065.3 ± 24.3	468.59 ± 24.67	30.03 ± 1.36	40.02 ± 1.46
440 stainless steel	4	2009.1 ± 26.0	581.15 ± 19.28	32.26 ± 1.72	39.36 ± 1.08
6Al-4V titanium	3	1362.5 ± 43.0	275.37 ± 53.74	25.19 ± 2.25	54.08 ± 2.95
6Al-4V titanium	4	1319.6 ± 22.8	190.57 ± 28.72	25.07 ± 1.21	51.10 ± 1.73

Table 5.7: Resultant cutting coefficient and angle for all workpiece and tool combinations performed on the CMD and commercial dynamometer.

Material	**Tool #**	**Ks CMD (N/mm^2)**	**Ks Kistler (N/mm^2)**	**Beta CMD (degrees)**	**Beta Kistler (degrees)**
2024 aluminum	1	1065.7 ± 40.6	1062.6 ± 11.9	75.41 ± 2.15	75.25 ± 0.63
2024 aluminum	2	1018.6 ± 53.4	1082.2 ± 9.2	71.37 ± 2.91	72.33 ± 0.46
6061 aluminum	1	914.6 ± 38.1	936.2 ± 26.5	68.27 ± 2.55	68.14 ± 1.52
6061 aluminum	2	941.6 ± 71.3	928.5 ± 43.3	74.55 ± 4.41	72.93 ± 2.76
7075 aluminum	1	826.9 ± 37.0	913.7 ± 9.9	81.14 ± 12.56	76.68 ± 0.63
7075 aluminum	2	1043.1 ± 52.6	968.8 ± 10.6	73.87 ± 2.87	75.00 ± 0.62
1018 steel	3	1821.2 ± 19.0	1835.4 ± 9.1	73.13 ± 0.63	72.01 ± 0.28
1018 steel	4	1905.9 ± 26.8	1930.8 ± 5.6	69.45 ± 0.72	68.78 ± 0.16
4140 steel	3	2144.1 ± 28.2	2220.0 ± 5.2	74.53 ± 0.75	75.13 ± 0.13
4140 steel	4	2089.6 ± 24.9	2223.9 ± 6.1	72.85 ± 0.71	72.49 ± 0.15
A36 steel	3	1955.4 ± 29.6	1951.4 ± 8.7	70.62 ± 0.99	70.44 ± 0.23
A36 steel	4	1889.6 ± 26.6	1939.5 ± 12.0	69.57 ± 0.76	68.82 ± 0.29
H13 steel	3	1933.4 ± 28.1	1937.3 ± 5.7	76.27 ± 0.82	76.54 ± 0.17
H13 steel	4	1941.6 ± 26.0	1936.6 ± 4.7	73.04 ± 0.74	73.00 ± 0.14
303 stainless steel	3	2117.3 ± 30.6	2047.4 ± 5.7	74.35 ± 0.81	75.24 ± 0.16
303 stainless steel	4	2080.5 ± 23.5	1994.1 ± 6.4	69.06 ± 0.58	72.36 ± 0.18
304 stainless steel	3	2136.1 ± 28.1	2134.1 ± 7.7	72.48 ± 0.78	72.36 ± 0.19
304 stainless steel	4	2183.3 ± 26.0	2269.3 ± 15.2	71.62 ± 0.64	71.11 ± 0.34
316 stainless steel	3	2295.9 ± 31.6	2399.1 ± 13.9	70.59 ± 0.81	71.13 ± 0.31
316 stainless steel	4	2564.5 ± 29.4	2636.7 ± 19.9	68.00 ± 0.64	67.72 ± 0.37
440 stainless steel	3	2117.9 ± 24.5	2152.0 ± 6.2	77.22 ± 0.66	76.93 ± 0.17
440 stainless steel	4	2091.6 ± 22.6	2171.6 ± 6.9	73.86 ± 0.64	72.38 ± 0.17
6Al-4V titanium	3	1391.0 ± 47.7	1624.6 ± 20.7	78.61 ± 2.05	72.79 ± 0.70
6Al-4V titanium	4	1333.6 ± 24.6	1491.6 ± 17.1	81.79 ± 1.17	76.82 ± 0.66

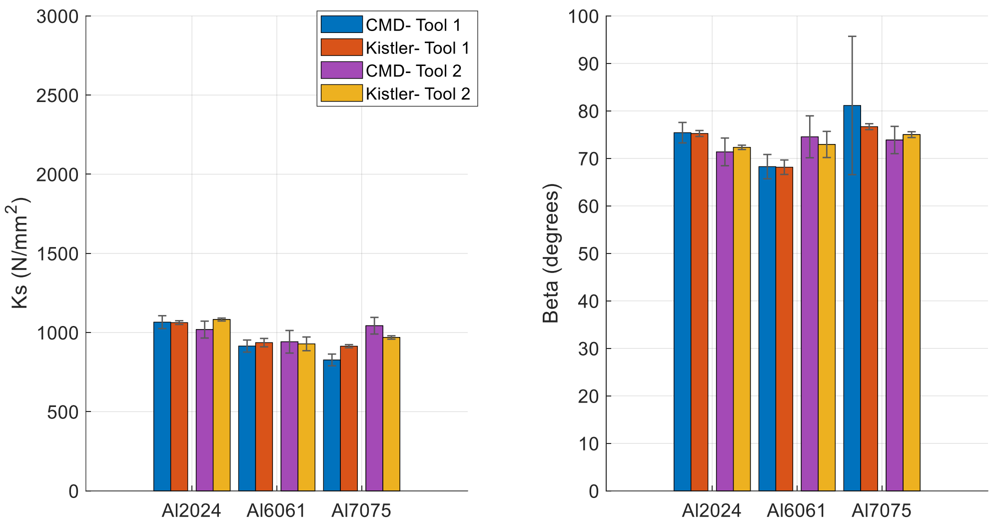

Figure 5.1: Resultant cutting coefficients and Beta angles for all aluminum workpiece and tool combinations performed on both the CMD and commercial dynamometer.

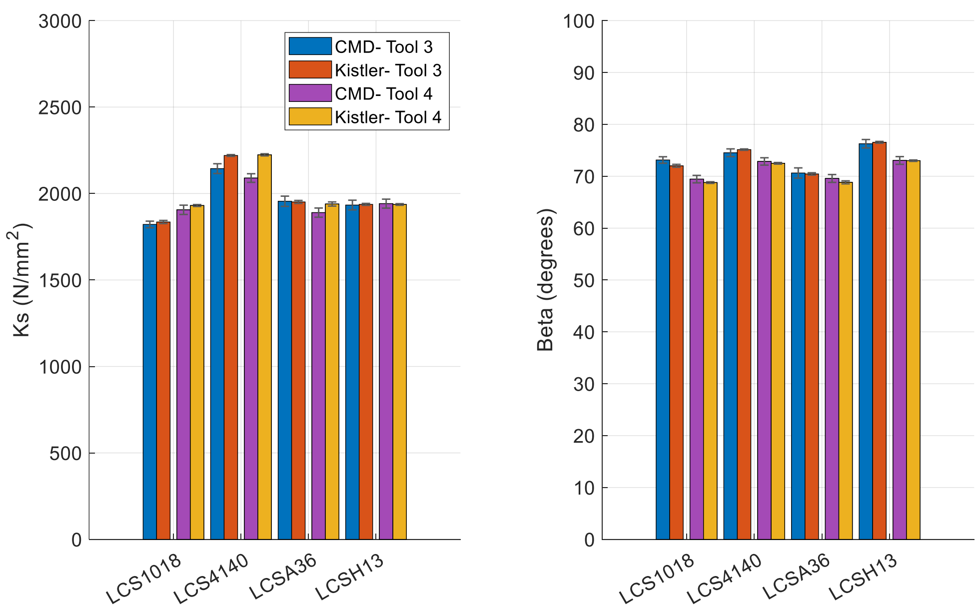

Figure 5.2: Resultant cutting coefficients and Beta angles for all low carbon steel workpiece and tool combinations performed on both the CMD and commercial dynamometer.

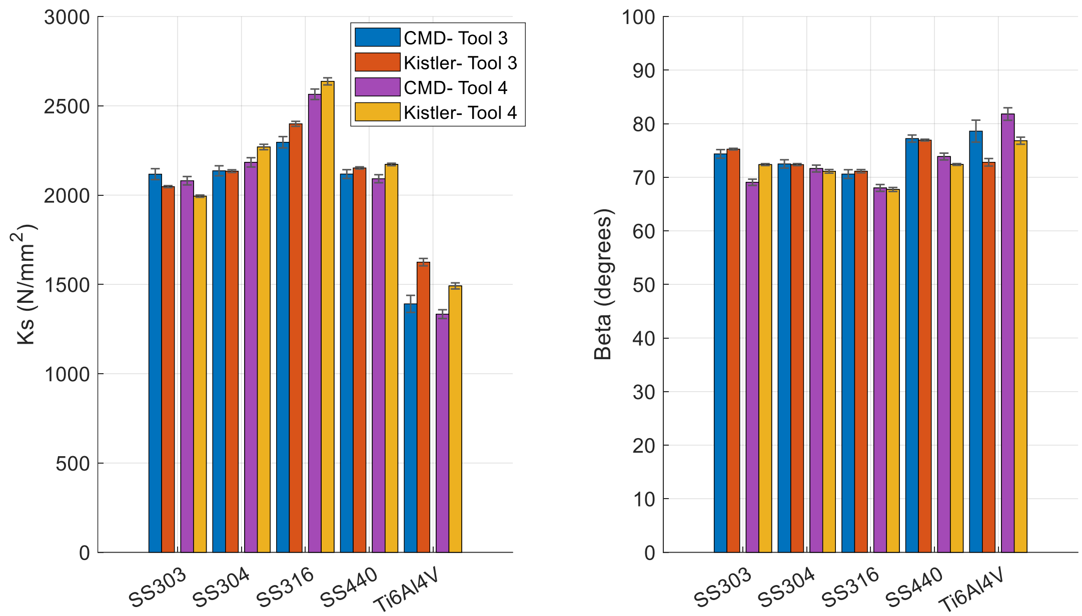

Figure 5.3: Resultant cutting coefficients and Beta angles for all stainless steel and titanium workpiece and tool combinations performed on both the CMD and commercial dynamometer.

one standard deviation for each material and tool combination for both the CMD and commercial dynamometer (Kistler). For most of the materials and tools the mean value of K_s is within one standard deviation between the two dynamometers. Some materials are within two standard deviations for both tools such as 4140 low carbon steel and the 303 and 440 series stainless steels. The worst correlation is the titanium at 3 standard deviations between the CMD and commercial dynamometer for both tools. The overall agreement between the two dynamometers proves that the low cost CMD can be used to reliably gather the CFC values needed to construct a force model for milling for different tools and workpiece combinations. There are some possibilities for the errors between the mean values. The first being a result of the workpieces having some difference in preparation or setup. If not properly secured, there could be some unwanted energy dissipation at the connection between the workpiece and dynamometer. Also, the consistency of the error could be a result of an error in setup or performing tap testing for the modal parameters. If the modal stiffness found from tap testing is too high or low compared to the actual values the mean value and therefore the CFC value can be shifted up or down from the expected value. Overall, the magnitudes line up well with expected values, where aluminums will have lower values and stainless steels are on the higher end of CFC values depending on the alloy. For the cutting force angles shown there is no correlation of the value of the angle between any particular tool or material group, but the mean values are spread out between 68 and 82 degrees.

Since the K_s and β values are calculated from the original k_t and k_n, both plots for those two CFCs are also shown in **Figure 5.4-5.6.** These plots show similar patterns to those described for the K_s value plot, where there is clear distinction between aluminum and steel values and some error for certain materials between the two dynamometers. The normal CFC, however, does show more spread in the normal values compared to the tangential CFC values.

Force Model Comparison

This first main goal of this thesis was to validate the constrained motion dynamometer in gathering forces, for a wide variety of materials and in tools, compared to an industry standard cutting force dynamometer. With the mean force values, and now the cutting force coefficients validated against the commercial dynamometer within a reasonable level of error, the final step

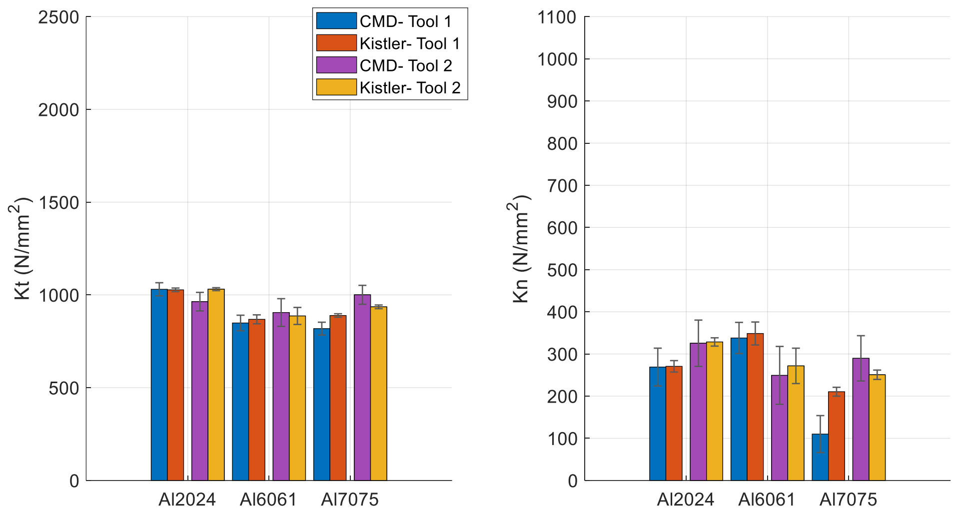

Figure 5.4: Tangential and normal cutting coefficients for all aluminum workpiece and tool combinations performed on both the CMD and commercial dynamometer.

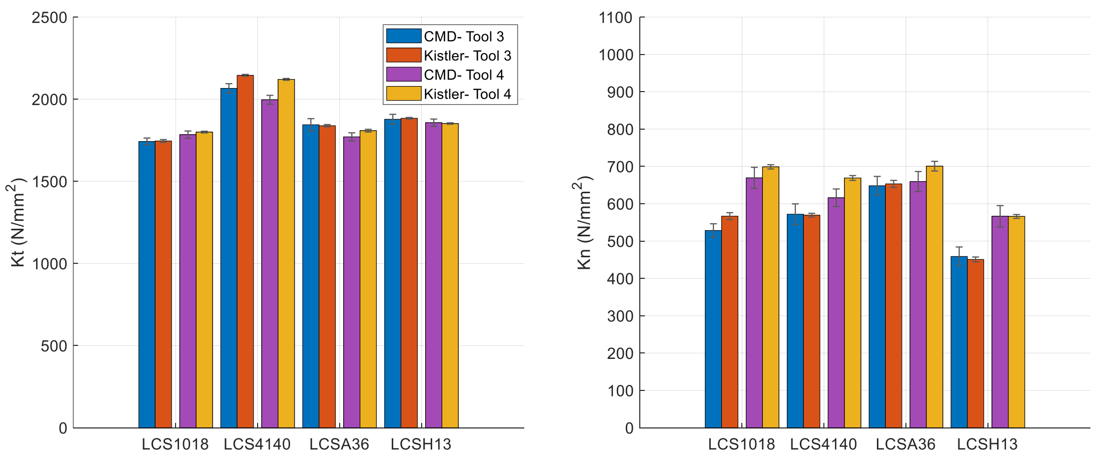

Figure 5.5: Tangential and normal cutting coefficients for all low carbon steel workpiece and tool combinations performed on both the CMD and commercial dynamometer.

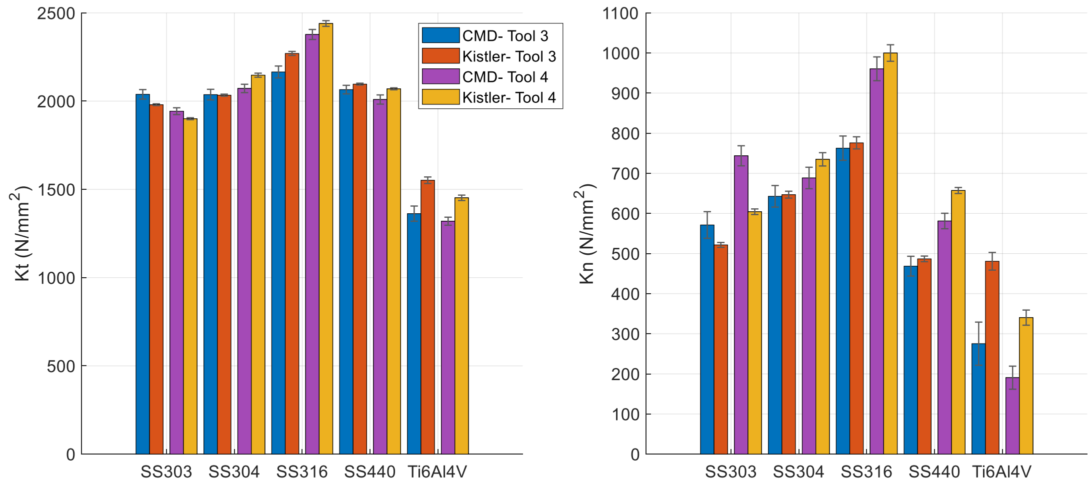

Figure 5.6: Tangential and normal cutting coefficients for all stainless steel and titanium workpiece and tool combinations performed on both the CMD and commercial dynamometer.

of the process can be validated. That is the mechanistic milling force model used to simulate cutting conditions for particular tool-workpiece combinations. As explained prior, the variables used for the milling model can mostly be found or set through traditional means of physical measurements. This includes the tool geometry and cutting conditions. The two inputs that require more advanced measurement systems to accurately portray the system are the frequency response functions and the cutting force coefficients. The validation of using the CMD to find the CFC values has already been completed. Therefore, when constructing the mechanistic force model there is no longer a need for the commercial dynamometer when looking to get a low-cost alternative for CFC values and model validation. The only variable left is the FRFs that are both used for the structural deconvolution of the measured displacement of the CMD and also used to input as the structural dynamics of the system into the model. For the purposes of this thesis, all FRF measurements used were gathered utilizing commercial grade equipment and software to ensure accuracy in the measurements used and to minimize sources of error for validating the CMD itself. However, as stated previously there do exist other methods to be able to obtain the FRFs for the tool and workpiece including FEA simulations for workpieces and tools and receptance coupling modeling for tools.

As shown in chapter 4 though, once an initial FRF is determined for the CMD the updated modal parameters can be calculated as mass is removed from the workpiece. This involved the assumption of a single degree of freedom (SDoF) where all mass being removed only affects that SDoF. With the stiffness and damping staying the same between cuts, all that was needed is an update to the modal mass value which is used with the stiffness to find the change in natural frequency. Therefore, it has been shown that as long as the mass being removed is known for a certain cut that the updated modal mass and therefore natural frequency can be calculated.

When looking at the force model construction all of the CFC values are from the CMD measurements and all FRFs are taken from tap testing results. All other parameters are taken for the tools from the tooling selection table, the runout of the tools was measured for each tool used, and the selected speeds based on the stability maps results for the corresponding test cuts. As stated before, all tests conducted were two by two-millimeter axial and radial depth of cut and were performed utilizing down milling. To avoid an excess of unnecessary results, only the

0.150 mm/tooth feed examples will be shown for the feed (*x*) and cross-feed (*y*) direction plots for all 24 cases. **Figure 5.7-10** shows some of the resulting plots for comparing the deconvolved force signals from the CMD to the constructed mechanistic force model. Only one set of feed and cross-feed plots are shown for each material group to see the difference in magnitudes for the differing materials. The rest of the plots will be shown in appendix B.

There are a few points to make about the following figures. Firstly, something that applies to all figures is the ability to match magnitudes of the signals in the *x* and *y*-directions, but with the previously mentioned fact that the maximum values for each tooth are going to be higher in the model than the deconvolved forces due to the filtering of high frequency content. No filtering was performed on the force model to avoid skewing any data from what should be generated normally. The second point to make is about the runout values, since the runout for each tool was measured on the spindle, the relative distance from the center axis could be inserted into the model. This runout is what controls the relative magnitudes of each tooths maximum force to the next tooths. Therefore, in **Figure 5.7** where the tool is a three-fluted tool, a repeated pattern of three different magnitudes can be seen in the simulation and on the deconvolved forces. In **Figure 5.8**, the evenly spaced four-fluted tool is also seen in a repeating pattern of four different magnitudes as even 90 degree intervals. The third major finding was that for the abnormal tooth spacing on the Kennametal four-fluted tool, as long as the correct tooth spacing and runout order is input into the model, an accurate model can be constructed. It is hard to tell in **Figure 5.9** since the forces are all lined up, but there is a slightly different tooth spacing at the 90-85-90-95 degree offsets. All of these finding are good indications that an accurate force model can be constructed utilizing the proposed methods for a wide variety of tools and materials as long as conditions are stable and within the limits of the dynamometer.

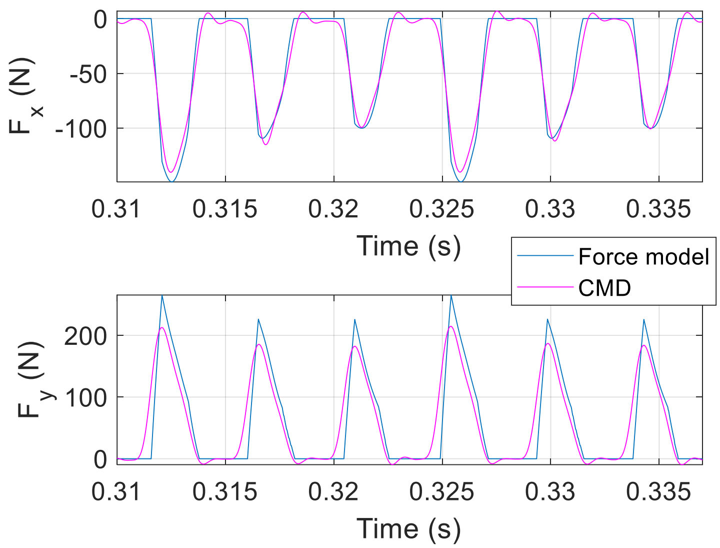

Figure 5.7: 2024 aluminum, tool #1, comparing the deconvolved force from CMD to the mechanistic force model construction at 0.150 mm/tooth for the *x* and *y*-directions.

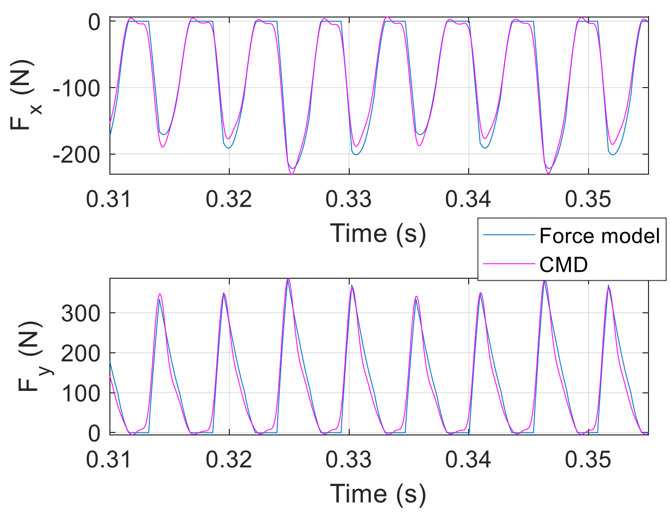

Figure 5.8: 1018 steel, tool #3, comparing the deconvolved force from CMD to the mechanistic force model construction at 0.150 mm/tooth for the *x* and *y*-directions.

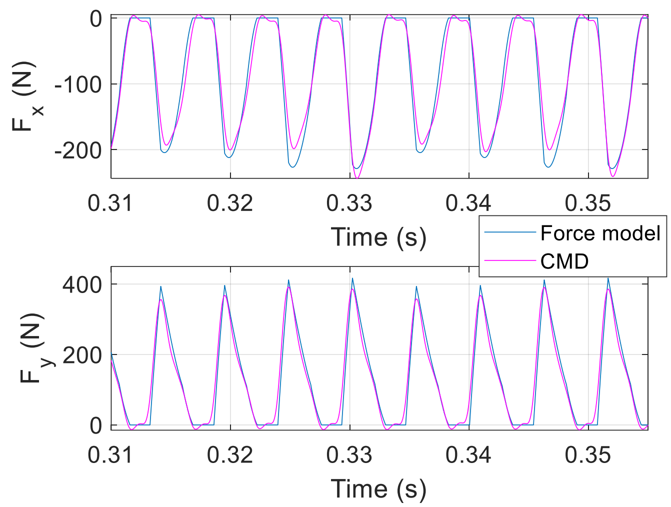

Figure 5.9: 303 stainless steel, tool #3, comparing the deconvolved force from CMD to the mechanistic force model construction at 0.150 mm/tooth for the *x* and *y*-directions.

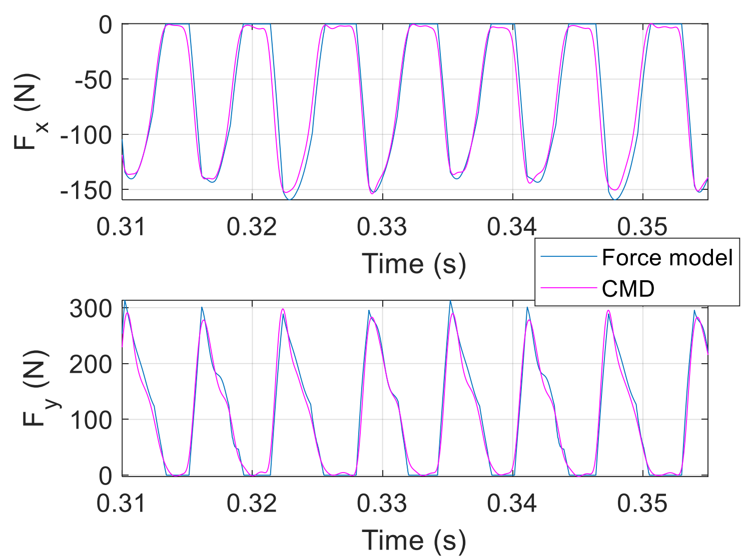

Figure 5.10: Ti6Al4V, tool #4, comparing the deconvolved force from CMD to the mechanistic force model construction at 0.150 mm/tooth for the *x* and *y*-directions.

CHAPTER SIX

CONCLUSIONS

Overall, the system has been made more robust. If following the set of instructions given in this thesis, CFC values and an accompanying mechanistic force model can be constructed for any number of endmills and materials. Firstly, the proposal of an on-system sensitivity coefficient calculation utilizing the hanging mass test was used to minimize the cost of calibration while still giving an accurate volt to displacement conversion. Secondly, it was determined that a compensation coefficient (α) was needed to account for a previously unaccounted for bending mode in the structure. The compensation amount for testing was determined utilizing only two FRFs, one direct FRF from the accelerometer that is already needed for deconvolving the force and one cross FRF from the KES that is already on the system. Other minor modifications were the reworking of the KES board, and its accompanying 3D printed housing that assisted in repeatable placement of the sensor in the KES. Also, all of the wiring was converted from DuPont connectors to an M12 three-pin barrel connection with soldered leads. The M12 connection with soldered leads decreased the ability for any connections to come loose from the KES, and increased robustness of the connections to the CMD itself and to the data acquisition box.

All of this initial work assisted with the ease of use when collecting data from the system. Utilizing the compensated displacement measurements from the CMD, the previous deconvolution method could be used to compared the deconvolved forces to the commercial grade system. It was shown that these measurement all lied within a reasonable amount of error that could be corelated to the stochastic nature of milling. Finally, the CFCs needed to input into a simulated force model could be calculated, which allowed the ability to simulate cutting forces. Ultimately the simulated mechanistic force model is what can be used to simulate any variety of cutting conditions for the specific tool-workpiece combination.

Further Application

Currently the CMD can be utilized by anyone with the proper tap testing and data collection equipment. While this equipment is usually not as costly as the Kistler 9257B dynamometer, it could still be cost prohibitive for a smaller lab or shop wanting to utilize force measurements.

Some barriers to consider would be the power supply and data acquisition device/software. Currently a lab grade variable power supply is used to supply the five volt power to the sensor, but a lower cost five-volt constant power supply could be utilized if one with minimal electrical noise could be tested. Moving to a lower cost data acquisition device such as an Arduino could be beneficial and allows for more flexibility in the data collection depending on the use case. Also, for the software, currently MATLAB is utilized for all data collection and processing but moving to an open-source option such as Python or Octave would remove the need for an expensive license. Finally, the addition of other methods of acquiring the FRFs could be used as long as proper validation is done to avoid the tap testing equipment cost.

Some of the other drawbacks of the current system include the lack of coolant/waterproofing the system. This results in the inability to use coolant during cutting tests which is used to lubricate the tool, wash away chips, and to take heat out of the system. This is a problem when testing on aluminum where chip adhesion and gulling affect the forces being measured and adds unwanted noise into the cutting forces. The galling effect was seen as the increase of standard deviation of the mean forces as opposed to the cuts in steel. Therefore, finding a new sensor, or packaging the current sensor to be able to withstand the use of flood coolant would be ideal if the dynamometer were to be used in a shop environment. Not only could the forces be measured closer to conditions that are present during machining of actual parts, but the CMD could be left on the machine table without worry of coolant and chips affecting the ability to measure forces.

The final drawback of the current system is the ability to only measure one degree of motion at a time. Unlike the commercial dynamometer that is able to measure three directions for one cut, the CMD is only able to measure in the flexible direction of the stage. Therefore, for any testing such as the CFC values that need both directions of forces, multiple cuts are needed. If wanting to simplify the collection of force values with a low-cost dynamometer, a multiple degree of freedom system is needed. Such as those proposed by Ramsauer et al. [15], which follows the same monolithic structure construction, or more complex systems such as those proposed by Palalic et al. [22]. Further testing would have to be done with those particular systems to be able to validate their use in gathering forces while milling in the same manner done for the current CMD design in this thesis.

LIST OF REFERENCES

[1] T. L. Schmitz and K. S. Smith, *Machining Dynamics: Frequency Response to Improved Productivity*. Cham: Springer International Publishing, 2019. doi: 10.1007/978-3-319-93707-6.

[2] J. Tlusty, *Manufacturing Processes and Equipment*. Upper Saddle River, NJ: Prentice Hall, 2000.

[3] M. A. Rubeo and T. L. Schmitz, "Milling Force Modeling: A Comparison of Two Approaches," *Procedia Manufacturing*, vol. 5, pp. 90–105, 2016, doi: 10.1016/j.promfg.2016.08.010.

[4] Z. Mason, "Sensor Comparison For Low-Cost Dynamic Force Measurement in Milling," University of Tennessee Knoxville.

[5] E. Budak, Y. Altintas¸, and E. J. A. Armarego, "Prediction of Milling Force Coefficients From Orthogonal Cutting Data," *Journal of Manufacturing Science and Engineering*, vol. 118, no. 2, pp. 216–224, May 1996, doi: 10.1115/1.2831014.

[6] Y. Altintas, *Manufacturing automation: Metal cutting mechanics, machine tool Vibrations, and CNC Design*, Second. Cambridge, UK: Cambridge University Press, 2012.

[7] Y. Altintaş and E. Budak, "Analytical Prediction of Stability Lobes in Milling," *CIRP Annals*, vol. 44, no. 1, pp. 357–362, 1995, doi: 10.1016/S0007-8506(07)62342-7.

[8] S. Smith and J. Tlusty, "An overview of modeling and simulation of the milling process," *Journal of Engineering for Industry*, no. 113, pp. 169–175, 1991.

[9] T. Poon, "DESIGN OF MACHINE TOOL CROSS BEAM USING METAL BIG AREA ADDITIVE MANUFACTURING," University of Tennessee Knoxville, 2023.

[10] A. Múgica and M. Bueno, "PREDICTION OF VIBRATIONAL PARAMETERS OF A MACHINE FIXTURE BY FINITE ELEMENT METHOD," University of Skovde, Sweeden, 2024.

[11] T. Schmitz, E. Betters, E. Budak, E. Yüksel, S. Park, and Y. Altintas, "Review and status of tool tip frequency response function prediction using receptance coupling," *Precision Engineering*, vol. 79, pp. 60–77, Jan. 2023, doi: 10.1016/j.precisioneng.2022.09.008.

[12] M. Gomez, “Displacement-based dynamometer for milling force measurement,” University of Tennessee Knoxville, 2021.

[13] “Kistler Instruction Manual.” Kistler Group, 2024.

[14] G. M. Gu, Y. K. Shin, J. Son, and J. Kim, “Design and characterization of a photo-sensor based force measurement unit (FMU),” *Sensors and Actuators A: Physical*, vol. 182, pp. 49–56, Aug. 2012, doi: 10.1016/j.sna.2012.05.018.

[15] C. Ramsauer, D. Leitner, C. Habersohn, T. Schmitz, K. Yamazaki, and F. Bleicher, “Flexure-based dynamometer for vector-valued milling force measurement,” *Journal of Machine Engineering*, Feb. 2023, doi: 10.36897/jme/161234.

[16] R. Zameroski, M. Gomez, and T. Schmitz, “Geometry-based, Gaussian profile model for optical knife-edge displacement sensor,” *Precision Engineering*, vol. 73, pp. 470–476, Jan. 2022, doi: 10.1016/j.precisioneng.2021.10.011.

[17] ROHM, “Transmission type Photointerrupters Eco-Friendly type.” ROHM semiconductor, 2017.

[18] J. Nazario, D. Pollard, and T. Schmitz, “Milling force measurement using a constrained motion dynamometer with compensation,” *Manufacturing Letters*, 2025.

[19] M. F. Gomez and T. L. Schmitz, “Displacement-based dynamometer for milling force measurement,” *Procedia Manufacturing*, vol. 34, pp. 867–875, 2019, doi: 10.1016/j.promfg.2019.06.161.

[20] İ. Korkut, “A dynamometer design and its construction for milling operation,” *Materials & Design*, vol. 24, no. 8, pp. 631–637, Dec. 2003, doi: 10.1016/S0261-3069(03)00122-5.

[21] R. Swan, “Surface Location Error in Robotic Milling: Modeling and Experiments,” University of Tennessee Knoxville, 2023.

[22] M. Palalic, H.-C. Möhring, W. Maier, A. G. De Mendoza, and F. Riemeier, “Multiaxial force platform with disturbance compensation for machine tools,” *Journal of Machine Engineering*, vol. 20, no. 3, pp. 5–16, Sep. 2020, doi: 10.36897/jme/127105.

APPENDIX

Appendix A: Mean force tables

Table A.1: 2024 aluminum, tool #1, mean forces measured from the commercial dynamometer vs the CMD deconvolved force.

FX mean (N)				FY mean (N)			
FPT (mm)	**Kistler**	**CMD**	**% Error**	**FPT (mm)**	**Kistler**	**CMD**	**% Error**
0.1	28.59	27.51	-3.8%	**0.1**	49.54	49.69	0.3%
0.125	34.07	33.84	-0.7%	**0.125**	55.19	55.77	1.1%
0.15	39.58	38.70	-2.2%	**0.15**	60.93	60.57	-0.6%
0.175	45.17	43.88	-2.9%	**0.175**	66.95	66.82	-0.2%
0.2	50.51	49.95	-1.1%	**0.2**	71.74	72.41	0.9%

Table A.2: 7075 aluminum, tool #2, mean forces measured from the commercial dynamometer vs the CMD deconvolved force.

FX mean (N)				FY mean (N)			
FPT (mm)	**Kistler**	**CMD**	**% Error**	**FPT (mm)**	**Kistler**	**CMD**	**% Error**
0.1	-19.03	-18.69	-1.7%	**0.1**	35.83	34.99	-2.3%
0.125	-22.32	-21.27	-4.7%	**0.125**	38.94	38.64	-0.8%
0.15	-25.92	-25.19	-2.8%	**0.15**	42.57	41.95	-1.5%
0.175	-29.13	-29.69	1.9%	**0.175**	45.87	46.76	2.0%
0.2	-32.20	-31.96	-0.7%	**0.2**	49.45	49.78	0.7%

Table A.3: 7075 aluminum, tool #1, mean forces measured from the commercial dynamometer vs the CMD deconvolved force.

FX mean (N)				FY mean (N)			
FPT (mm)	**Kistler**	**CMD**	**% Error**	**FPT (mm)**	**Kistler**	**CMD**	**% Error**
0.1	-27.20	-27.04	-0.6%	**0.1**	54.71	55.04	0.6%
0.125	-32.13	-32.39	0.8%	**0.125**	59.15	59.90	1.3%
0.15	-36.84	-35.92	-2.5%	**0.15**	64.01	61.92	-3.3%
0.175	-42.16	-40.83	-3.1%	**0.175**	69.38	68.76	-0.9%
0.2	-46.38	-46.50	0.3%	**0.2**	73.10	69.56	-4.8%

Table A.4: 1018 steel, tool #3, mean forces measured from the commercial dynamometer vs the CMD deconvolved force.

FX mean (N)				FY mean (N)			
FPT (mm)	**Kistler**	**CMD**	**% Error**	**FPT (mm)**	**Kistler**	**CMD**	**% Error**
0.1	-59.43	-58.73	-1.2%	**0.1**	87.81	88.17	0.4%
0.125	-70.93	-70.11	-1.2%	**0.125**	102.13	102.11	0.0%
0.15	-82.79	-81.62	-1.4%	**0.15**	115.50	114.17	-1.2%
0.175	-94.96	-95.28	0.3%	**0.175**	129.00	129.65	0.5%
0.2	-106.86	-106.41	-0.4%	**0.2**	142.31	140.72	-1.1%

Table A.5: A36 steel, tool #4, mean forces measured from the commercial dynamometer vs the CMD deconvolved force.

FX mean (N)				FY mean (N)			
FPT (mm)	**Kistler**	**CMD**	**% Error**	**FPT (mm)**	**Kistler**	**CMD**	**% Error**
0.1	-61.70	-60.77	-1.5%	**0.1**	104.51	103.51	-1.0%
0.125	-73.78	-71.00	-3.8%	**0.125**	123.14	120.59	-2.1%
0.15	-85.63	-83.66	-2.3%	**0.15**	138.53	135.58	-2.1%
0.175	-97.16	-95.01	-2.2%	**0.175**	152.24	150.04	-1.4%
0.2	-108.72	-106.94	-1.6%	**0.2**	165.16	161.48	-2.2%

Table A.6: A36 steel, tool #3, mean forces measured from the commercial dynamometer vs the CMD deconvolved force.

FX mean (N)				FY mean (N)			
FPT (mm)	**Kistler**	**CMD**	**% Error**	**FPT (mm)**	**Kistler**	**CMD**	**% Error**
0.1	-64.58	-64.69	0.2%	**0.1**	101.96	100.43	-1.5%
0.125	-76.87	-75.77	-1.4%	**0.125**	116.70	116.41	-0.2%
0.15	-88.87	-88.54	-0.4%	**0.15**	131.92	130.07	-1.4%
0.175	-101.29	-101.96	0.7%	**0.175**	146.52	146.16	-0.2%
0.2	-113.50	-112.95	-0.5%	**0.2**	160.99	159.40	-1.0%

Table A.7: H13 steel, tool #4, mean forces measured from the commercial dynamometer vs the CMD deconvolved force.

FX mean (N)				FY mean (N)			
FPT (mm)	**Kistler**	**CMD**	**% Error**	**FPT (mm)**	**Kistler**	**CMD**	**% Error**
0.1	-63.05	-62.85	-0.3%	**0.1**	93.30	91.84	-1.6%
0.125	-75.87	-74.92	-1.2%	**0.125**	107.43	105.45	-1.8%
0.15	-88.59	-86.83	-2.0%	**0.15**	122.00	119.00	-2.5%
0.175	-101.50	-101.38	-0.1%	**0.175**	135.83	133.60	-1.6%
0.2	-114.14	-113.91	-0.2%	**0.2**	149.68	148.50	-0.8%

Table A.8: H13 steel, tool #3, mean forces measured from the commercial dynamometer vs the CMD deconvolved force.

FX mean (N)				FY mean (N)			
FPT (mm)	**Kistler**	**CMD**	**% Error**	**FPT (mm)**	**Kistler**	**CMD**	**% Error**
0.1	-67.01	-66.26	-1.1%	**0.1**	86.00	84.66	-1.6%
0.125	-79.91	-78.80	-1.4%	**0.125**	100.96	99.00	-1.9%
0.15	-92.96	-92.29	-0.7%	**0.15**	114.07	112.46	-1.4%
0.175	-106.39	-105.91	-0.4%	**0.175**	127.48	125.60	-1.5%
0.2	-121.95	-120.29	-1.4%	**0.2**	139.26	138.18	-0.8%

Table A.9: 4140 steel, tool #4, mean forces measured from the commercial dynamometer vs the CMD deconvolved force.

FX mean (N)				FY mean (N)			
FPT (mm)	**Kistler**	**CMD**	**% Error**	**FPT (mm)**	**Kistler**	**CMD**	**% Error**
0.1	-69.95	-69.18	-1.1%	**0.1**	109.59	109.67	0.1%
0.125	-84.08	-81.56	-3.0%	**0.125**	126.43	125.29	-0.9%
0.15	-98.73	-96.95	-1.8%	**0.15**	142.87	139.38	-2.4%
0.175	-113.21	-109.49	-3.3%	**0.175**	159.13	156.96	-1.4%
0.2	-128.12	-124.11	-3.1%	**0.2**	175.04	170.22	-2.8%

Table A.10: H13 steel, tool #3, mean forces measured from the commercial dynamometer vs the CMD deconvolved force.

FX mean (N)				FY mean (N)			
FPT (mm)	**Kistler**	**CMD**	**% Error**	**FPT (mm)**	**Kistler**	**CMD**	**% Error**
0.1	-74.59	-73.97	-0.8%	**0.1**	104.29	103.66	-0.6%
0.125	-89.92	-88.19	-1.9%	**0.125**	119.57	119.18	-0.3%
0.15	-105.26	-102.36	-2.8%	**0.15**	134.51	132.39	-1.6%
0.175	-120.67	-117.52	-2.6%	**0.175**	150.85	148.99	-1.2%
0.2	-135.48	-132.02	-2.6%	**0.2**	166.87	165.08	-1.1%

Table A.11: 303 stainless steel, tool #4, mean forces measured from the commercial dynamometer vs the CMD deconvolved force.

FX mean (N)				FY mean (N)			
FPT (mm)	**Kistler**	**CMD**	**% Error**	**FPT (mm)**	**Kistler**	**CMD**	**% Error**
0.1	-57.81	-57.58	-0.4%	**0.1**	101.95	100.67	-1.3%
0.125	-70.23	-69.46	-1.1%	**0.125**	118.25	120.29	1.7%
0.15	-83.11	-84.46	1.6%	**0.15**	132.85	137.09	3.2%
0.175	-96.42	-93.26	-3.3%	**0.175**	147.10	151.64	3.1%
0.2	-109.75	-108.99	-0.7%	**0.2**	160.98	165.42	2.8%

Table A.12: 304 stainless steel, tool #4, mean forces measured from the commercial dynamometer vs the CMD deconvolved force.

FX mean (N)				FY mean (N)			
FPT (mm)	**Kistler**	**CMD**	**% Error**	**FPT (mm)**	**Kistler**	**CMD**	**% Error**
0.1	-58.46	-59.02	1.0%	**0.1**	118.86	119.80	0.8%
0.125	-72.95	-74.46	2.1%	**0.125**	137.02	136.55	-0.3%
0.15	-87.75	-87.37	-0.4%	**0.15**	155.48	156.31	0.5%
0.175	-101.75	-101.99	0.2%	**0.175**	171.73	170.76	-0.6%
0.2	-116.22	-115.20	-0.9%	**0.2**	186.70	183.96	-1.5%

Table A.13: 304 stainless steel, tool #3, mean forces measured from the commercial dynamometer vs the CMD deconvolved force.

FX mean (N)				FY mean (N)			
FPT (mm)	**Kistler**	**CMD**	**% Error**	**FPT (mm)**	**Kistler**	**CMD**	**% Error**
0.1	-62.47	-62.40	-0.1%	**0.1**	112.95	111.50	-1.3%
0.125	-76.54	-76.72	0.2%	**0.125**	129.59	129.66	0.0%
0.15	-90.56	-90.24	-0.4%	**0.15**	145.60	146.64	0.7%
0.175	-104.57	-104.53	0.0%	**0.175**	160.28	160.52	0.2%
0.2	-118.02	-118.13	0.1%	**0.2**	176.24	174.56	-1.0%

Table A.14: 440 stainless steel, tool #4, mean forces measured from the commercial dynamometer vs the CMD deconvolved force.

FX mean (N)				FY mean (N)			
FPT (mm)	**Kistler**	**CMD**	**% Error**	**FPT (mm)**	**Kistler**	**CMD**	**% Error**
0.1	-69.37	-70.69	1.9%	**0.1**	112.65	109.51	-2.8%
0.125	-83.45	-84.73	1.5%	**0.125**	129.72	124.66	-3.9%
0.15	-97.62	-97.31	-0.3%	**0.15**	145.47	139.84	-3.9%
0.175	-111.80	-110.98	-0.7%	**0.175**	161.12	155.24	-3.6%
0.2	-126.03	-127.96	1.5%	**0.2**	176.91	169.36	-4.3%

Table A.15: 440 stainless steel, tool #3, mean forces measured from the commercial dynamometer vs the CMD deconvolved force.

FX mean (N)				FY mean (N)			
FPT (mm)	**Kistler**	**CMD**	**% Error**	**FPT (mm)**	**Kistler**	**CMD**	**% Error**
0.1	-71.61	-72.50	1.2%	**0.1**	106.17	105.83	-0.3%
0.125	-86.59	-86.23	-0.4%	**0.125**	122.99	121.81	-1.0%
0.15	-102.89	-102.49	-0.4%	**0.15**	137.72	136.59	-0.8%
0.175	-117.81	-118.09	0.2%	**0.175**	151.60	149.29	-1.5%
0.2	-132.26	-131.92	-0.3%	**0.2**	165.33	163.70	-1.0%

Table A.16: 316 stainless steel, tool #4, mean forces measured from the commercial dynamometer vs the CMD deconvolved force.

FX mean (N)				FY mean (N)			
FPT (mm)	**Kistler**	**CMD**	**% Error**	**FPT (mm)**	**Kistler**	**CMD**	**% Error**
0.1	-59.21	-58.27	-1.6%	**0.1**	128.11	131.99	3.0%
0.125	-74.55	-75.74	1.6%	**0.125**	150.04	153.88	2.6%
0.15	-90.54	-89.11	-1.6%	**0.15**	174.14	175.30	0.7%
0.175	-105.67	-103.85	-1.7%	**0.175**	195.26	194.29	-0.5%
0.2	-121.49	-120.40	-0.9%	**0.2**	209.24	212.04	1.3%

Table A.17: 316 stainless steel, tool #3, mean forces measured from the commercial dynamometer vs the CMD deconvolved force.

FX mean (N)				FY mean (N)			
FPT (mm)	**Kistler**	**CMD**	**% Error**	**FPT (mm)**	**Kistler**	**CMD**	**% Error**
0.1	-66.31	-63.27	-4.6%	**0.1**	120.35	119.21	-0.9%
0.125	-80.98	-76.71	-5.3%	**0.125**	138.29	137.58	-0.5%
0.15	-96.31	-92.39	-4.1%	**0.15**	157.68	155.74	-1.2%
0.175	-113.18	-105.63	-6.7%	**0.175**	171.00	170.81	-0.1%
0.2	-126.60	-120.95	-4.5%	**0.2**	194.37	189.55	-2.5%

Table A.18: Ti6Al4V, tool #4, mean forces measured from the commercial dynamometer vs the CMD deconvolved force.

FX mean (N)				FY mean (N)			
FPT (mm)	**Kistler**	**CMD**	**% Error**	**FPT (mm)**	**Kistler**	**CMD**	**% Error**
0.1	-46.96	-43.47	-7.4%	**0.1**	89.19	95.12	6.6%
0.125	-56.60	-53.30	-5.8%	**0.125**	97.70	94.73	-3.0%
0.15	-67.27	-64.34	-4.4%	**0.15**	108.98	103.90	-4.7%
0.175	-78.16	-74.48	-4.7%	**0.175**	119.02	115.89	-2.6%
0.2	-88.95	-83.68	-5.9%	**0.2**	129.53	125.53	-3.1%

Appendix B: Mean force tables

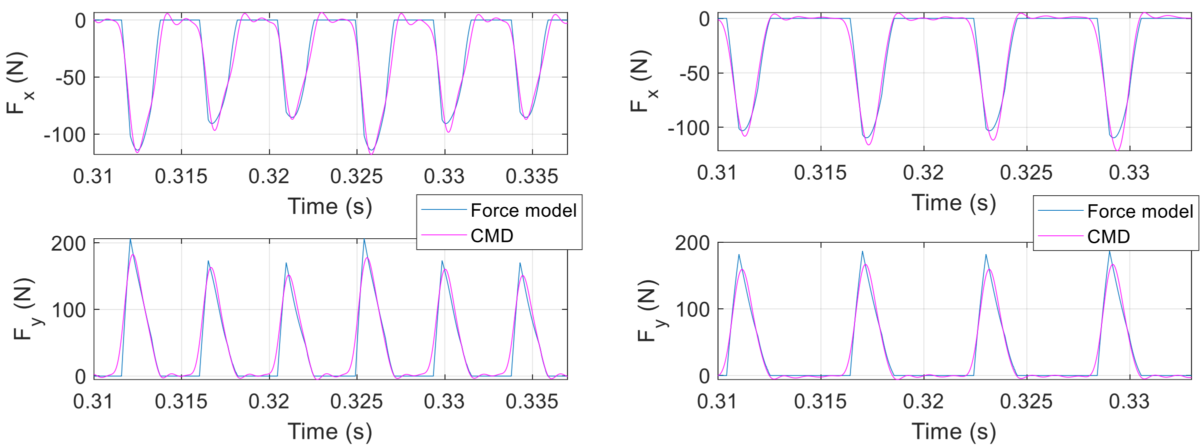

Figure B.1: 6061 aluminum, (left) tool #1 and (right) tool #2, comparing the deconvolved force from CMD to the mechanistic force model construction at 0.150 mm/tooth for the (top) *x* and (bottom) *y*-directions.

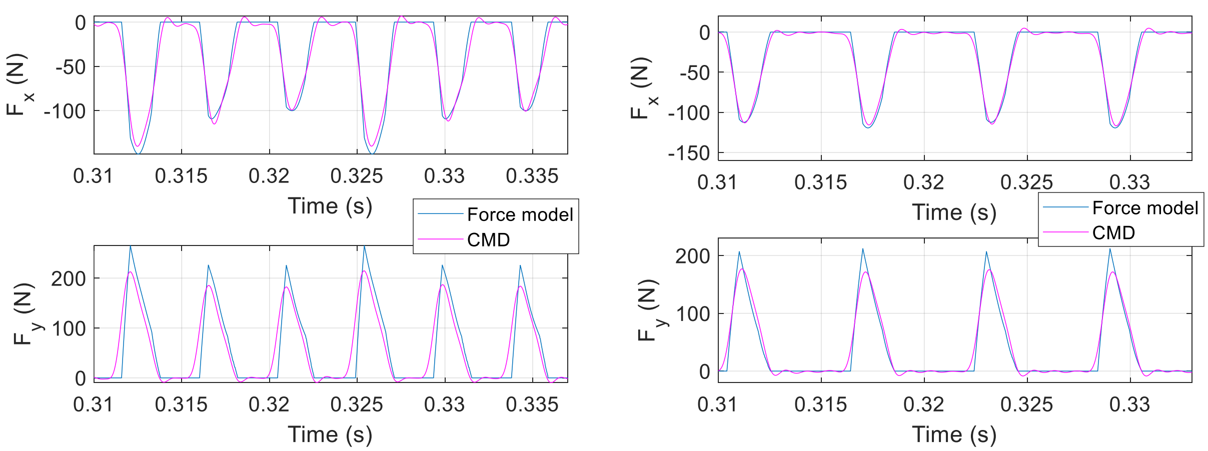

Figure B.2: 2024 aluminum, (left) tool #1 and (right) tool #2, comparing the deconvolved force from CMD to the mechanistic force model construction at 0.150 mm/tooth for the (top) *x* and (bottom) *y*-directions.

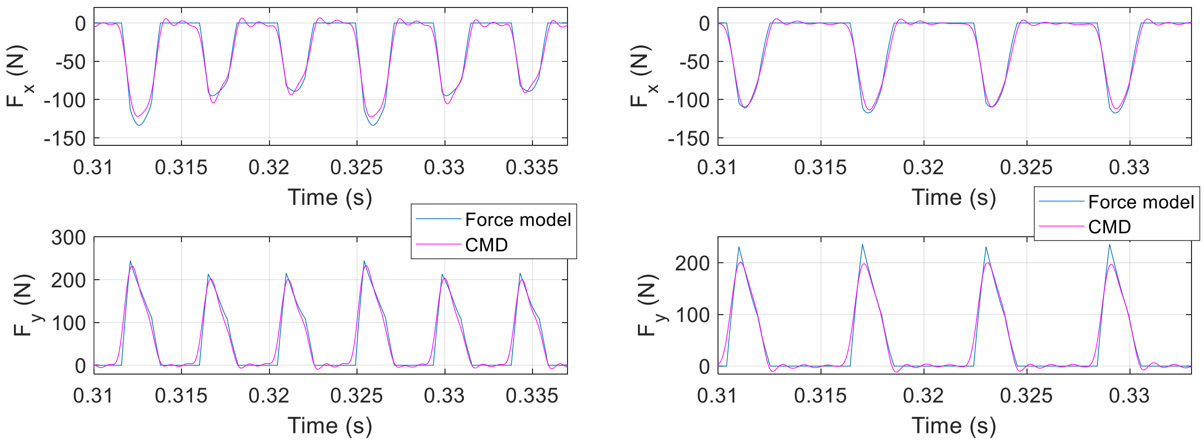

Figure B.3: 7075 aluminum, (left) tool #1 and (right) tool #2, comparing the deconvolved force from CMD to the mechanistic force model construction at 0.150 mm/tooth for the (top) *x* and (bottom) *y*-directions.

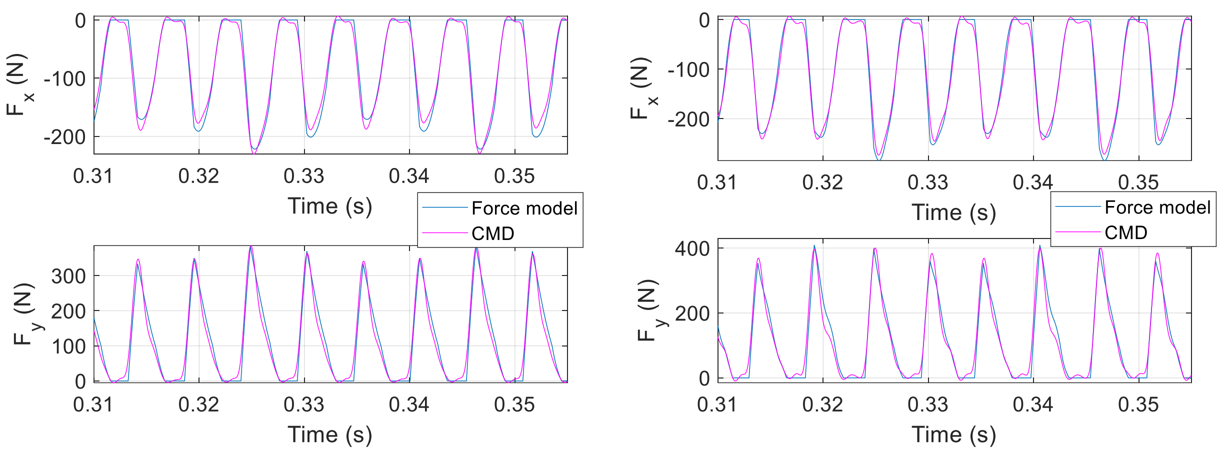

Figure B.4: 1018 steel, (left) tool #3 and (right) tool #4, comparing the deconvolved force from CMD to the mechanistic force model construction at 0.150 mm/tooth for the (top) *x* and (bottom) *y*-directions.

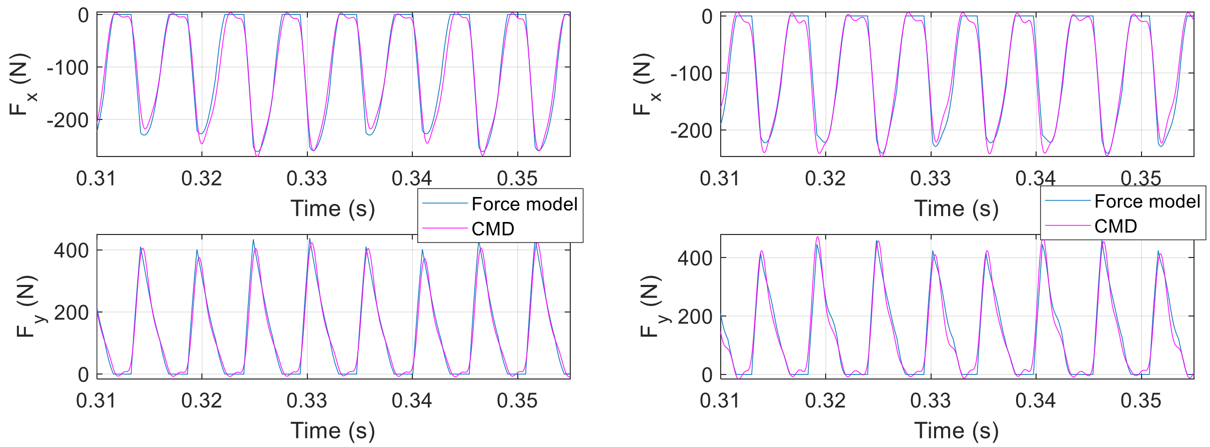

Figure B.5: 4140 steel, (left) tool #3 and (right) tool #4, comparing the deconvolved force from CMD to the mechanistic force model construction at 0.150 mm/tooth for the (top) *x* and (bottom) *y*-directions.

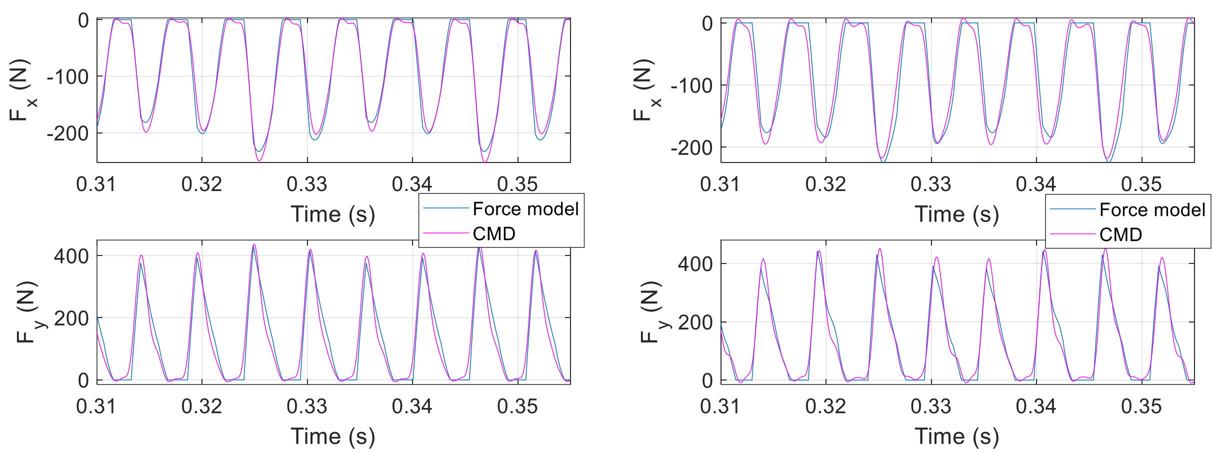

Figure B.6: A36 steel, (left) tool #3 and (right) tool #4, comparing the deconvolved force from CMD to the mechanistic force model construction at 0.150 mm/tooth for the (top) *x* and (bottom) *y*-directions.

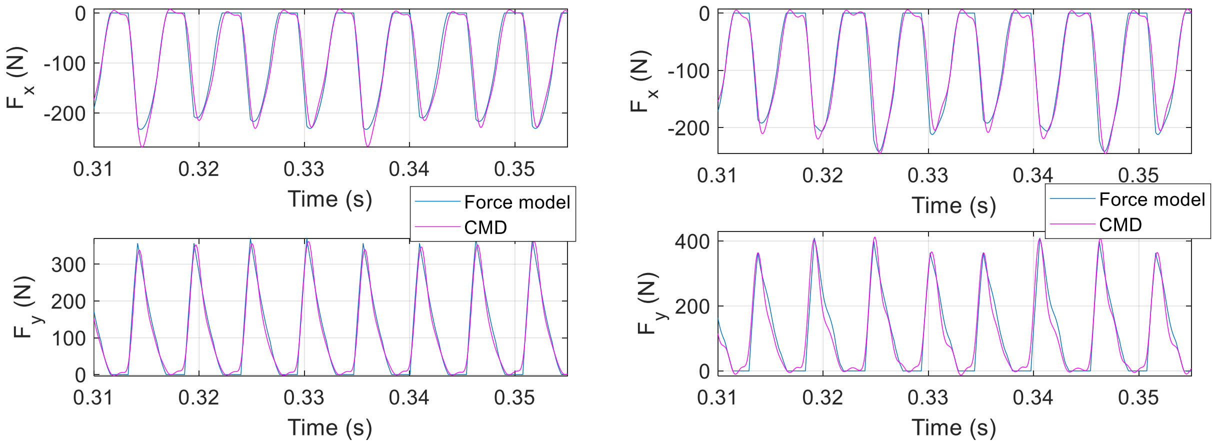

Figure B.7: H13 steel, (left) tool #3 and (right) tool #4, comparing the deconvolved force from CMD to the mechanistic force model construction at 0.150 mm/tooth for the (top) *x* and (bottom) *y*-directions.

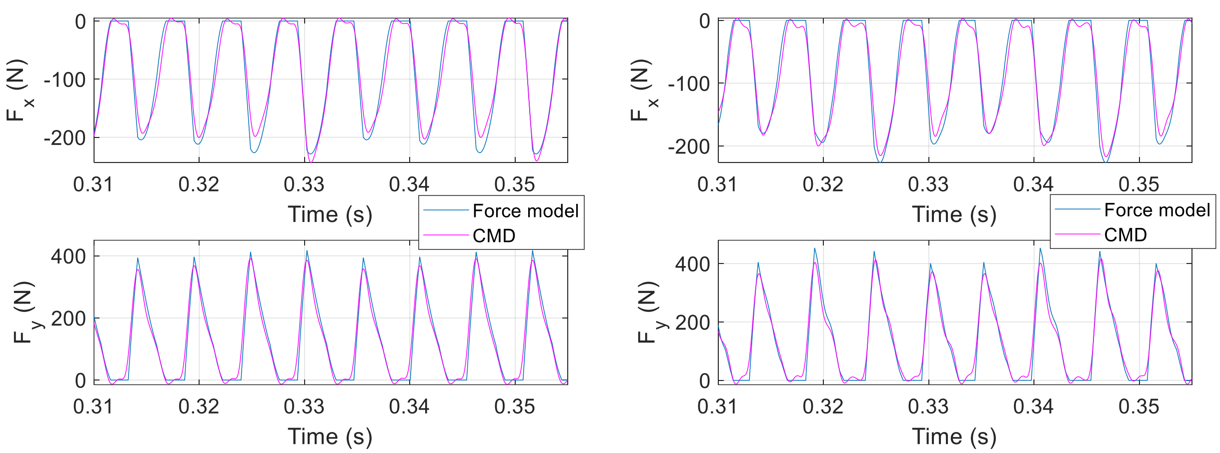

Figure B.8: 303 stainless steel, (left) tool #3 and (right) tool #4, comparing the deconvolved force from CMD to the mechanistic force model construction at 0.150 mm/tooth for the (top) *x* and (bottom) *y*-directions.

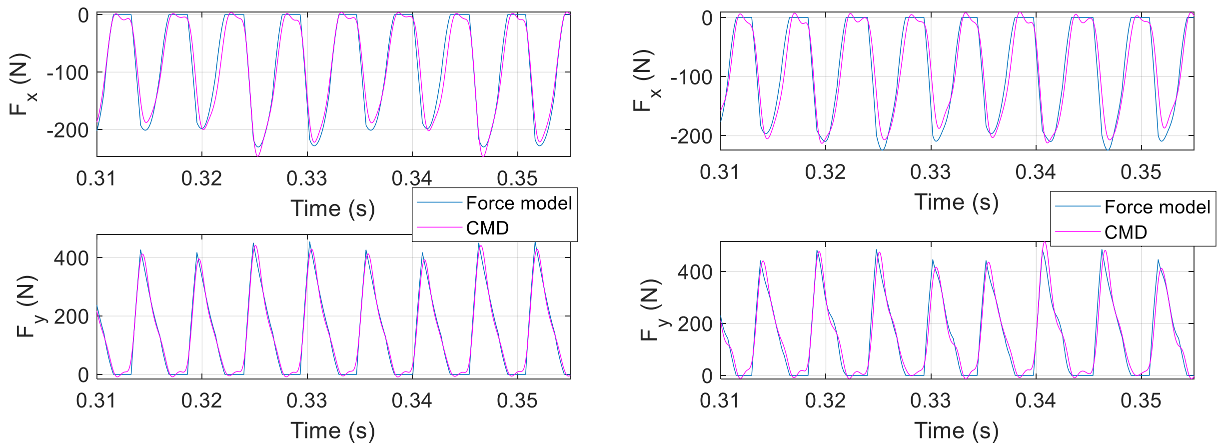

Figure B.9: 304 stainless steel, (left) tool #3 and (right) tool #4, comparing the deconvolved force from CMD to the mechanistic force model construction at 0.150 mm/tooth for the (top) *x* and (bottom) *y*-directions.

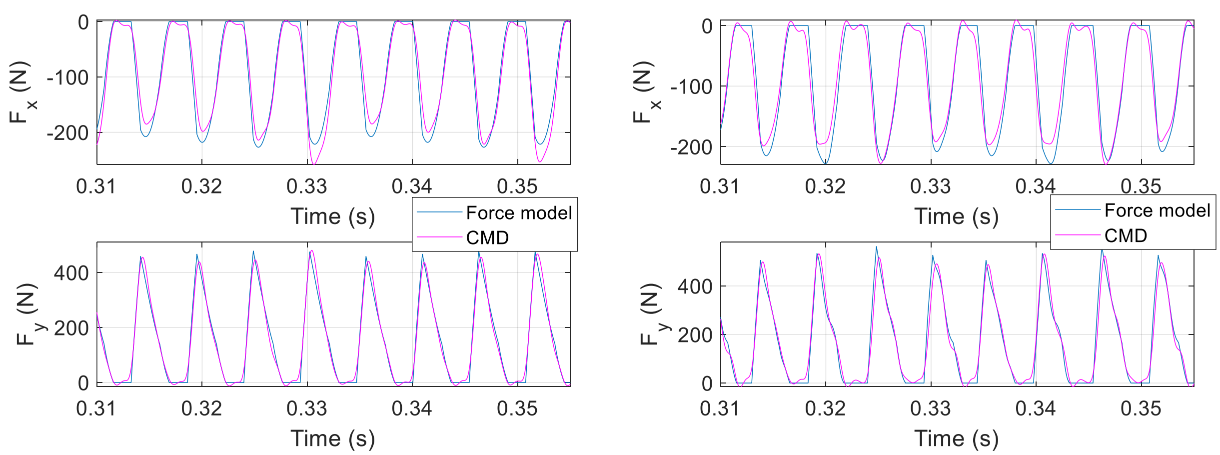

Figure B.10: 316 stainless steel, (left) tool #3 and (right) tool #4, comparing the deconvolved force from CMD to the mechanistic force model construction at 0.150 mm/tooth for the (top) *x* and (bottom) *y*-directions.

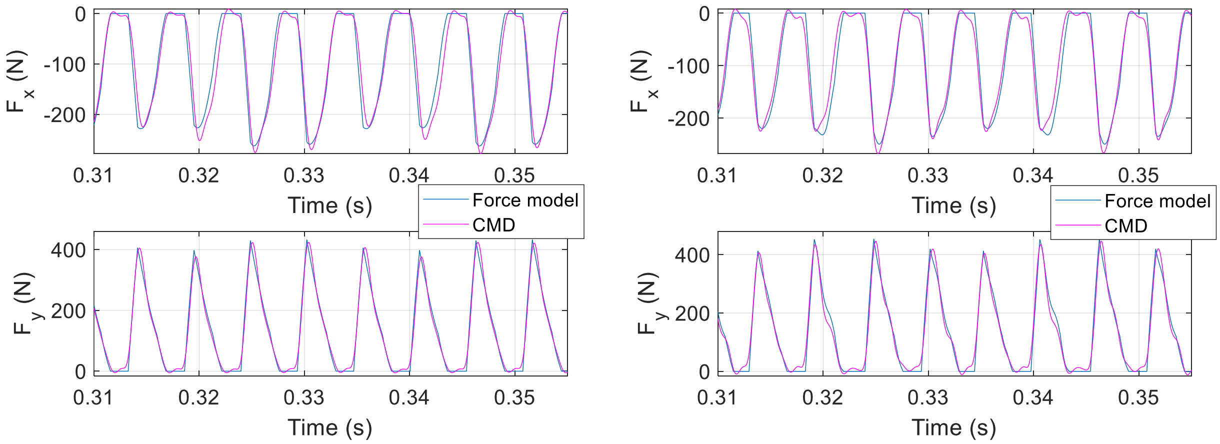

Figure B.11: 440 stainless steel, (left) tool #3 and (right) tool #4, comparing the deconvolved force from CMD to the mechanistic force model construction at 0.150 mm/tooth for the (top) *x* and (bottom) *y*-directions.

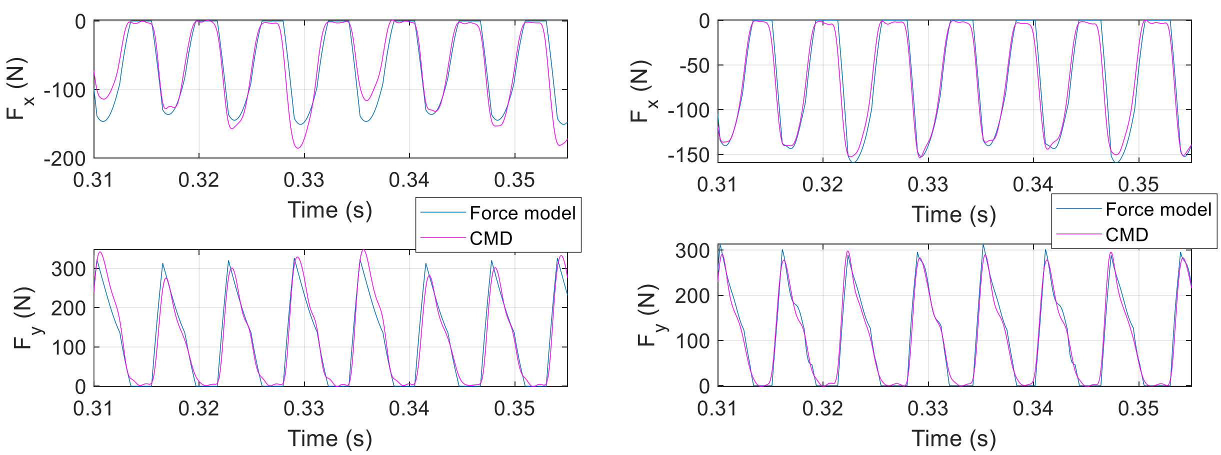

Figure B.12: Ti6Al4V, (left) tool #3 and (right) tool #4, comparing the deconvolved force from CMD to the mechanistic force model construction at 0.150 mm/tooth for the (top) *x* and (bottom) *y*-directions.

VITA

Dylan Pollard was born in North Canton, Ohio in 2000. He learned about the basics of engineering throughout his years at Hoover High School (2015-19) and cemented his passion for mechanical engineering after joining the school's FIRST Robotics Competition team. He attended Case Western Reserve University (CWRU) (2019-23) in Cleveland, Ohio to earn his B.S.E. in Mechanical Engineering. During his time at CWRU he learned the fundamentals of mechanical systems, design, and manufacturing. After acquiring an internship at the University of Tennessee Knoxville in the Machine Tool Research Center he furthered his appreciation for manufacturing. He was able to continue his education at UTK (2023-25) starting under the direction of Dr. Tony Schmitz. His research focused on cutting force modeling during milling, low-cost measurements, modal tap testing, and some tool wear analysis. Outside of his research, he also assisted with machining projects for the Army Research Laboratory and acted as an assistant instructor for the America's Cutting Edge (ACE) program. He plans to enter the industry workforce as a manufacturing engineer starting in Knoxville, Tennessee.